A Directionally Dispersion-free Algorithm for the Calculation of Wake Potentials

Vom Fachbereich Elektrotechnik und Informationstechnik
der Technischen Universität Darmstadt

zur Erlangung
der Würde eines Doctor rerum naturalium (Dr. rer. nat.)
genehmigte

DISSERTATION

von

Dipl.-Phys. Robert Hampel
geboren am 29.06.1977 in Frankfurt am Main

Darmstadt 2009

Referent:	Prof. Dr.-Ing. Thomas Weiland
Korreferent:	Prof. Dr.-Ing. Ludger Klinkenbusch
Tag der Einreichung:	22. August 2008
Tag der mündlichen Prüfung:	31. Oktober 2008

D 17
Darmstädter Dissertation

Erklärung laut §9 PromO

Ich versichere hiermit, dass ich die vorliegende Dissertation allein und nur unter Verwendung der angegebenen Literatur verfasst habe. Die Arbeit hat bisher noch nicht zu Prüfungszewecken gedient.

Darmstadt, 21. August 2008

To
Helmut, Claudia,
Volker, and Mareike

Contents

Chapter 1

Introduction

Since the invention of particle accelerators in the first half of the twentieth century, scientists and engineers tried to expand the barriers of practicable investigations in order to discover more and more details of atomic and subatomic structures. The increasing resolution needed for a deeper insight into the structures of the microcosm demands for shorter de Broglie wavelengths of the accelerated particles. This requires higher momenta and kinetic energy, demanding for more powerful accelerators.

Numerical simulation techniques are indispensable tools supporting the design of such machines. They provide detailed information at low costs and allow for parameter studies within reasonable time. Moreover, not all quantities of interest are accessible via measurements. The final design is verified in tests of expensive prototypes and individual components.

In accelerators, particles are accelerated by a radio frequency field which is fed into a resonant structure. A typical accelerating structure which is used in many contemporary linear accelerators is the TESLA nine-cell cavity [1] (Fig. 1.1).

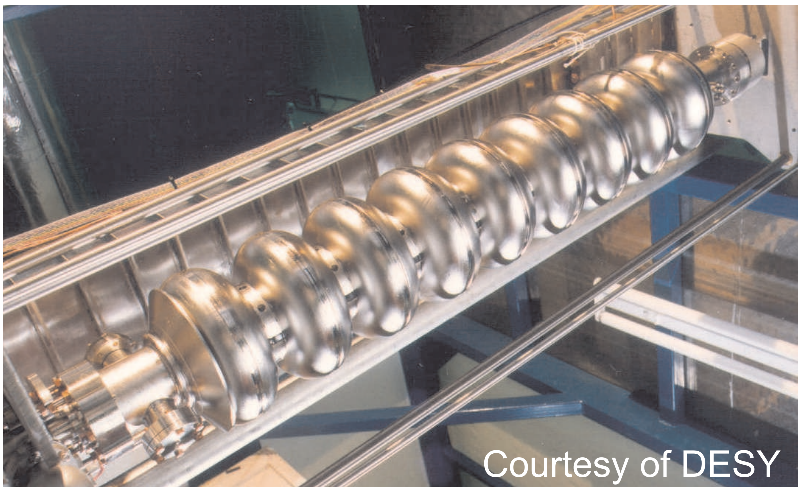
Courtesy of DESY

Figure 1.1: A TESLA nine-cell cavity.

In order to minimize wall losses the cavities are kept in operation at temperatures below 9.2 K where the cavity walls which are made of niobium become superconducting. This way high field gradients for the accelerating field are achieved. In the TESLA technology the RF field is tuned to the resonance frequency of 1.3 GHz of the cavity. The phase of the longitudinal electric field component is chosen in such a way that the particles experience an accelerating force every time they enter a cell of the cavity (Fig. 1.2).

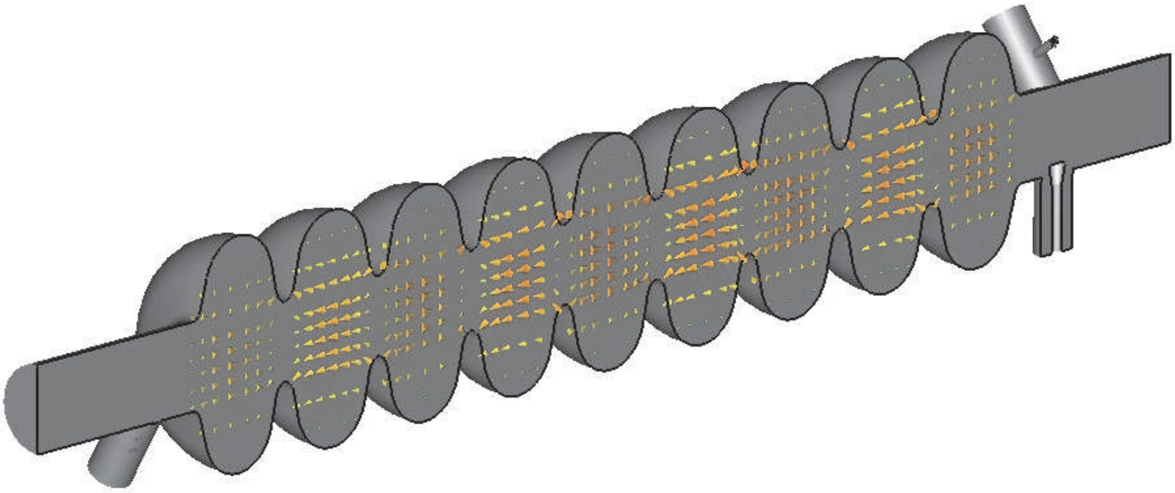

Figure 1.2: The plot shows the electric field distribution in a TESLA nine-cell cavity. The orientation of the electric field vector on axis changes its direction with time, such that a charged particle traveling through the cavity experiences an accelerating force in each cell.

It was discovered that simply by increasing the particles' energy limiting effects become significant. As a result, design values like, e.g. the beam current, cannot be achieved. One of these limiting effects are the so-called *wake fields* which spoil the emittance of the bunch or can lead to collective instabilities.

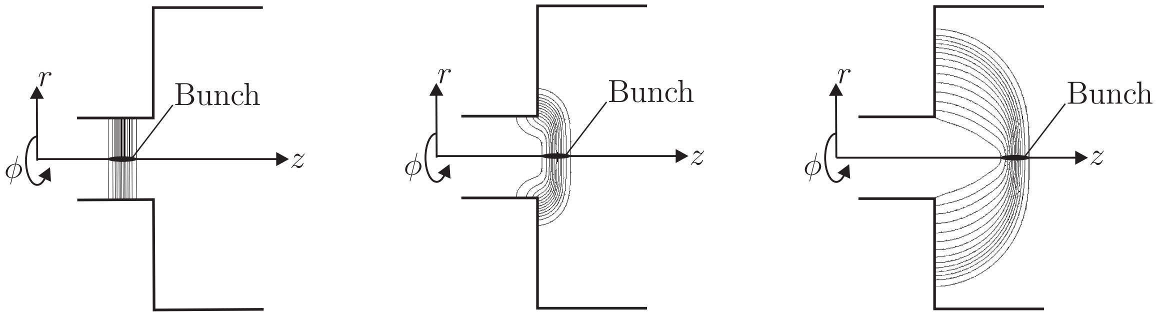

(a) The radial fields of a particle bunch.

(b) Passing the discontinuity, wake fields are excited.

(c) The wake fields propagate behind the particle bunch.

Figure 1.3: The lines of force of the fields for a particle bunch passing a discontinuity. The particle bunch travels at almost the speed of light.

Moving charged particles excite electromagnetic fields – the wake fields (Fig. 1.3) – which superimpose the accelerating RF field. Any particle bunch which travels in a smooth tube carries its radial electric and circular magnetic field. No additional fields are excited (Fig. 1.3(a)). Passing a discontinuity leads to the excitation of electromagnetic fields (Fig. 1.3(b)). These wake fields propagate behind the particle bunch (Fig. 1.3(c)) and have an impact on trailing charged particles.

The wake potential, which is computed from the wake fields, describes this impact of the bunch of particles onto itself and all trailing bunches. If not taken into account, the wake fields can lead to a deterioration of the beam quality or even beam loss due to instabilities. In particular, expensive major projects such as the X-FEL (for 1 bn Euros) or the ILC (for 5 bn Euros) would be set to fail.

Thus, reliable and accurate numerical algorithms are needed to predict the characteristic properties of components to be built or to optimize already existent components. There are several computer codes available which allow for the calculation of wake fields and wake potentials. Such programs are for example BCI [2], TBCI [3], ABCI [4], MAFIA [5], CST Particle Studio [5], ECHO [6], and PBCI [7]. Despite the good results obtained by MAFIA and CST Particle Studio, both programs suffer from numerical dispersion errors. These errors arise due to non-physical frequency dependent phase velocities in the numerical simulations. This deteriorates the accuracy of the results. In simulations of long accelerating structures, dispersion errors accumulate and therefore accurate results cannot be obtained.

Recently, the development of two simulation programs overcoming the dispersion errors in the direction of bunch motion has been reported [6, 8]. However, the computational cost of these programs are increased in comparison to the established MAFIA code which is based on the *Finite Integration Technique* (FIT) [9, 10]. In this thesis, an algorithm is developed which combines dispersion-free directions and the low memory demands of MAFIA.

The spatial discretization of Maxwell's equations is carried out via the established FIT. The time integration of the Maxwell-Grid-Equations is implemented using the leapfrog scheme. The combination of the FIT and the leapfrog scheme yields dispersion-free directions in the discrete space. Thus, the basic idea consists of rotating the computational grid which allows for the alignment of these inherently dispersion-free directions with the direction of bunch motion.

Besides errors due to numerical dispersion, the mapping of the structure to the discrete space leads to an inaccurate rendering of the original shape. This is another source of errors. Several of these mappings exist. The simplest one is the staircase technique which introduces large errors. In contrast to that, there are conformal mappings of the structure which render the shape more accurately. The benefits of conformal mappings are combined with the directionally dispersion-free scheme leading to an algorithm which is very well-suited to the simulation of wake fields for long accelerator structures.

Overview

This work is outlined as follows:

Firstly, Maxwell's equations describing continuous electromagnetic fields are introduced. On this basis, the wake fields and the wake function are described. Characterizing properties for the wake fields are presented – such as the wake potential.

Afterwards, the spatial discretization of Maxwell's equations according to the Finite Integration Technique is introduced. The FIT is combined with the leapfrog scheme in order to solve transient problems.

The dispersion properties of the spatial as well as the temporal discretization are investigated. The results allow for the identification of dispersion-free directions in the discrete space. In the following, the computational grid is rotated such that these directions are aligned with the direction of bunch motion.

The issues related to the development of a code with the properties mentioned above are described. These include the implementation of the scattered field approach, the computation of the exciting fields on the rotated grid, and different boundary approximation methods.

Two versions of the algorithm have been implemented. One of them being limited to the simulation of structures exhibiting a cylindrical symmetry. The other implementation can be applied to arbitrary three-dimensional structures. The dispersion properties of both implementations are tested. Furthermore, they are verified against other numerical simulation tools as well as analytical solutions.

Finally, two particle accelerator components which are currently subject to optimization are studied.

Concluding, the results are summarized and remaining questions are outlined.

Chapter 2

Continuous Electrodynamics

Maxwell's equations describe all macroscopic phenomena of electromagnetism. This chapter starts with a discussion of the continuous Maxwell's equations. A brief introduction to the basic set of equations is followed by a section about wake fields. The theory of wake fields is introduced as well as important characterizing equations.

2.1 Continuous Electromagnetic Fields

In the 19th century, several scientists were engaged in the research of electromagnetic phenomena. They formulated various mathematical equations describing these phenomena, for example Faraday's law of electromagnetic induction [11]

$$U_{\mathrm{ind}} = \int\limits_{\partial A} \vec{E} \cdot \mathrm{d}\vec{s} = -\frac{\mathrm{d}}{\mathrm{d}t} \int\limits_{A} \vec{B} \cdot \mathrm{d}\vec{A}, \tag{2.1}$$

and Ampère's circuital law [12]

$$\int\limits_{\partial A} \vec{H} \cdot \mathrm{d}\vec{s} = I. \tag{2.2}$$

The former states that the voltage induced in a loop ∂A is equal to the negative time derivative of the magnetic flux through that loop. The latter connects the magnetic field integrated along a closed path ∂A to the total electric current through the face A.

2.1.1 Maxwell's Equations

James Clerk Maxwell [13, 14] added the displacement current to Ampère's circuital law and published a set of equations based on existing works. These equations are called

Maxwell's equations. In integral form they read as follows

$$\int_{\partial A} \vec{E}\,(\vec{r},t)\cdot \mathrm{d}\vec{s} = -\frac{\mathrm{d}}{\mathrm{d}t}\int_{A} \vec{B}\,(\vec{r},t)\cdot \mathrm{d}\vec{A} \qquad \forall A \subset \mathbb{R}^3, t \in \mathbb{R}, \tag{2.3a}$$

$$\int_{\partial A} \vec{H}\,(\vec{r},t)\cdot \mathrm{d}\vec{s} = \frac{\mathrm{d}}{\mathrm{d}t}\int_{A} \vec{D}\,(\vec{r},t)\cdot \mathrm{d}\vec{A} + \int_{A} \vec{J}\,(\vec{r},t)\cdot \mathrm{d}\vec{A} \qquad \forall A \subset \mathbb{R}^3, t \in \mathbb{R}, \tag{2.3b}$$

$$\int_{\partial V} \vec{D}\,(\vec{r},t)\cdot \mathrm{d}\vec{A} = \int_{V} \rho\,(\vec{r},t)\,\mathrm{d}V \qquad \forall V \subseteq \mathbb{R}^3, t \in \mathbb{R}, \tag{2.3c}$$

$$\int_{\partial V} \vec{B}\,(\vec{r},t)\cdot \mathrm{d}\vec{A} = 0 \qquad \forall V \subseteq \mathbb{R}^3, t \in \mathbb{R}. \tag{2.3d}$$

Equation (2.3a) is known as Faraday's law and equation (2.3b) is given by Ampère's original law extended by the electric displacement current. The third equation is called Gauss's law. The fourth one, Gauss' law for magnetism, states the non-existence of magnetic monopoles.

The boundaries of the areas and the surfaces of the volumes on the left hand side in equations (2.3a-2.3d) are defined in the inertial system of the electric and magnetic fields. On the other hand, the areas and volumes on the right hand side are defined in a system at rest. In all problems which are addressed in this thesis, the media are at rest and the integrals in Maxwell's equations are evaluated with respect to the same inertial system. Therefore, no different inertial systems with relative movement occur. No additional terms or relativistic transformations have to be considered. Additionally, the areas and surfaces are fixed in time. Thus, equations (2.3a-2.3d) simplify to

$$\int_{\partial A} \vec{E}\,(\vec{r},t)\cdot \mathrm{d}\vec{s} \;=\; -\int_{A} \frac{\partial}{\partial t}\vec{B}\,(\vec{r},t)\cdot \mathrm{d}\vec{A} \qquad \forall A \subset \mathbb{R}^3, t \in \mathbb{R}, \tag{2.4a}$$

$$\int_{\partial A} \vec{H}\,(\vec{r},t)\cdot \mathrm{d}\vec{s} \;=\; \int_{A} \frac{\partial}{\partial t}\vec{D}\,(\vec{r},t)\cdot \mathrm{d}\vec{A} + \int_{A} \vec{J}\,(\vec{r},t)\cdot \mathrm{d}\vec{A} \qquad \forall A \subset \mathbb{R}^3, t \in \mathbb{R}, \tag{2.4b}$$

$$\int_{\partial V} \vec{D}\,(\vec{r},t)\cdot \mathrm{d}\vec{A} \;=\; \int_{V} \rho\,(\vec{r},t)\,\mathrm{d}V \qquad \forall V \subseteq \mathbb{R}^3, t \in \mathbb{R}, \tag{2.4c}$$

$$\int_{\partial V} \vec{B}\,(\vec{r},t)\cdot \mathrm{d}\vec{A} \;=\; 0 \qquad \forall V \subseteq \mathbb{R}^3, t \in \mathbb{R}. \tag{2.4d}$$

The correctness of physical laws cannot be proven in the mathematical sense. Nevertheless, Maxwell's equations hold true in all experimental verifications. Among the numerous experiments conducted is the test of the inverse square law for the electrostatic force. As a result of these experiments, the mass of the photon – the gauge boson of electromagnetism – is zero within an upper limit of

$$m_\gamma < 4 \cdot 10^{-51}\ \mathrm{kg},$$

indicating Gauss' law (eqn. (2.3c)) to be correct.

In the 20th century, quantum theory evolved and subsequently, physicists discovered electromagnetic effects which could not be explained solely by (the classical) Maxwell's equations. Particle generation by fields, the magnetic moment of the electron and many other effects on the microscopic scale could only be explained sufficiently with a new theory – quantum electrodynamics (QED). The later is the best experimentally proven theory in physics. The magnetic moment of the electron can be measured precisely to the eleventh decimal within the theoretical prediction of the QED. Nevertheless, since the QED deals with large fields on a microscopic scale as well as nuclear and particle physics, it will not be addressed in the further scope of this thesis.

Maxwell's equations in integral form (eqns. (2.3a)-(2.3d)) can be rewritten using the Gauß-Ostrogradsky theorem and Stokes' theorem which results in

$$\begin{aligned} \operatorname{curl} \vec{E}\,(\vec{r},t) &= -\frac{\partial}{\partial t}\vec{B}\,(\vec{r},t) && (2.5a)\\ \operatorname{curl} \vec{H}\,(\vec{r},t) &= \frac{\partial}{\partial t}\vec{D}\,(\vec{r},t) + \vec{J}\,(\vec{r},t) && (2.5b)\\ \operatorname{div} \vec{D}\,(\vec{r},t) &= \rho\,(\vec{r},t) && (2.5c)\\ \operatorname{div} \vec{B}\,(\vec{r},t) &= 0. && (2.5d) \end{aligned}$$

The current density $\vec{J}(\vec{r},t)$ in Maxwell's equations is composed of three parts:

$$\vec{J}(\vec{r},t) = \vec{J}_\kappa(\vec{r},t) + \vec{J}_C(\vec{r},t) + \vec{J}_I(\vec{r},t), \tag{2.6}$$

namely the conductive current density $\vec{J}_\kappa(\vec{r},t)$, the convective current density $\vec{J}_C(\vec{r},t)$, and the impressed current density $\vec{J}_I(\vec{r},t)$. In this thesis, fields excited by electron bunches are considered. Only the convective part $\vec{J}_C(\vec{r},t)$ of the current density has to be taken into account, i.e.,

$$\vec{J}(\vec{r},t) = \vec{J}_C(\vec{r},t) = \rho(\vec{r},t)\cdot\vec{v}(\vec{r},t), \tag{2.7}$$

with $\rho(\vec{r},t)$ being the charge distribution describing an electron bunch. The current densities $\vec{J}_\kappa(\vec{r},t)$ and $\vec{J}_I(\vec{r},t)$ are therefore neglected.

2.1.2 Constitutive Equations

The equations (2.5a-2.5d) form a coupled set of first order linear partial differential equations. Therefore, each equation cannot be solved individually. The vectors $\vec{E}$, $\vec{D}$, $\vec{H}$ and $\vec{B}$ are connected pairwise by relations describing the electric and magnetic properties of a given medium. The constitutive equations for an isotropic medium are given by

$$\begin{aligned} \vec{D}\,(\vec{r},t) &= \epsilon_0\vec{E}\,(\vec{r},t) + \vec{P}\,(\vec{r},t) && (2.8a)\\ \vec{B}\,(\vec{r},t) &= \mu_0\left(\vec{H}\,(\vec{r},t) + \vec{M}\,(\vec{r},t)\right). && (2.8b) \end{aligned}$$

and connect $\vec{E}$ with $\vec{D}$ as well as $\vec{H}$ with $\vec{B}$.

The electric polarization $\vec{P}$ and the magnetization $\vec{M}$ describe the microscopic response of the material, averaged on the macroscopic scale.

This thesis deals with the simulation of electromagnetic fields in accelerator structures consisting of metallic components, i.e. assuming a perfectly conducting material containing a vacuum. In vacuum, $\vec{P}$ and $\vec{M}$ are zero. Equations (2.8a and 2.8b) can thus be simplified to the constitutive equations for an isotropic homogeneous and frequency independent medium:

$$\begin{aligned} \vec{D}\left(\vec{r},t\right) &= \epsilon_0 \vec{E}\left(\vec{r},t\right) \qquad (2.9a) \\ \vec{B}\left(\vec{r},t\right) &= \mu_0 \vec{H}\left(\vec{r},t\right). \qquad (2.9b) \end{aligned}$$

Maxwell's equations describe all electromagnetic phenomena. Unfortunately, these set of differential equations can only be solved accurately in a very small number of situations. In the next section, electromagnetic fields induced by moving charged particles are introduced. In general, no analytical solution can be found for these fields and numerical simulations have to be performed instead.

2.2 Wake Fields

Charged particles excite scattered electromagnetic fields as they move through a surrounding structure (Fig. 1.3). The total electromagnetic field can be considered as a superposition of this scattered fields $\vec{E}_s$ and $\vec{H}_s$ and the exciting fields $\vec{E}_0$ and $\vec{H}_0$ generated by the charged particles in free space:

$$\begin{aligned} \vec{E} &= \vec{E}_0 + \vec{E}_s \\ \vec{H} &= \vec{H}_0 + \vec{H}_s. \qquad (2.10) \end{aligned}$$

The fields inside a metallic structure can be described in terms of the moving source charge and currents on the metallic walls. If these wall currents follow the source charge synchronously no scattered fields are excited. This is the case, e.g. for a charged particle moving at the speed of light within a homogeneous perfectly electric conducting (PEC) tube.

Passing a discontinuity in this tube, the wall current cannot follow the source charge. In order to fulfill the boundary conditions for the total fields, additional longitudinal electromagnetic fields are excited at the discontinuity. These scattered fields are called *wake fields*. They have an important impact on the beam dynamics in accelerators. In this section, a mathematical description and the physical quantities describing the effects of wake fields on charged particle beams are introduced.

2.2.1 Wake Function and Wake Potential

In order to derive the physical quantities describing the impact of the wake fields on trailing charges, it is assumed that two charged particles travel at the speed of light through a component of an accelerator. The first particle (Fig. 2.1) carrying the charge Q_1 – called the driving charge – has an offset $r_1 = |\vec{r}_1|$ to the axis. It is followed by a second particle carrying the charge Q_2 – called the witness charge – with an offset $r_2 = |\vec{r}_2|$ to the axis. The difference of the longitudinal positions $s = z_1 - z_2$ defines the abscissa of a co-moving coordinate system with the driving charge at its origin.

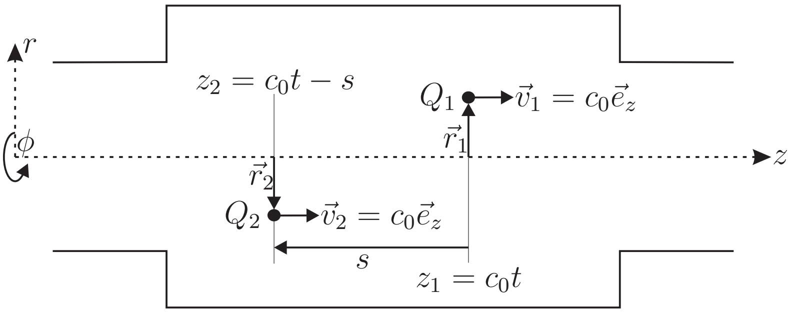

Figure 2.1: Two charged particles passing a discontinuity. Q_1, the driving charge, is followed by Q_2, the witness charge. The positions of both particles are described by $\vec{r}_1$ and z_1 and by $\vec{r}_2$ and z_2 respectively. s is defined as the relative position, $z_1 - z_2$, in the co-moving coordinate system.

The relativistic mass of a particle traveling at the velocity v is given by

$$m(v) = \gamma(v) \cdot m_0 \quad \text{with} \quad \gamma = \frac{1}{\sqrt{1-\beta^2}} \quad \text{and} \quad \beta = \frac{v}{c_0}, \tag{2.11}$$

with the speed of light c_0, the relative velocity β, and the Lorentz factor γ. In the ultra-relativistic energy regime, i.e. practically at the speed of light $\beta = 1$, the masses of the particles are infinitely large.

Therefore, the transversal position of each particle, which is described by the so-called beta-function [15, 16], is not varying along the beam path. The beta-function is considered constant along the interaction length. Thus, the motion of the particles is parallel to the axis, i.e. r_1 and r_2 are constant.

Additionally, the relativistic contraction of the electromagnetic field distribution has to be taken into account. At a velocity v smaller than the speed of light, the fields of the two charged particles Q_1 and Q_2 in Fig. 2.1 lead to interactions which are called space charge effects. The relativistic contraction of the spherically symmetric fields of a charge at rest into a cone perpendicular to the direction of motion depends on this velocity v of the charged particles (App. D). This is illustrated in Fig. 2.2.

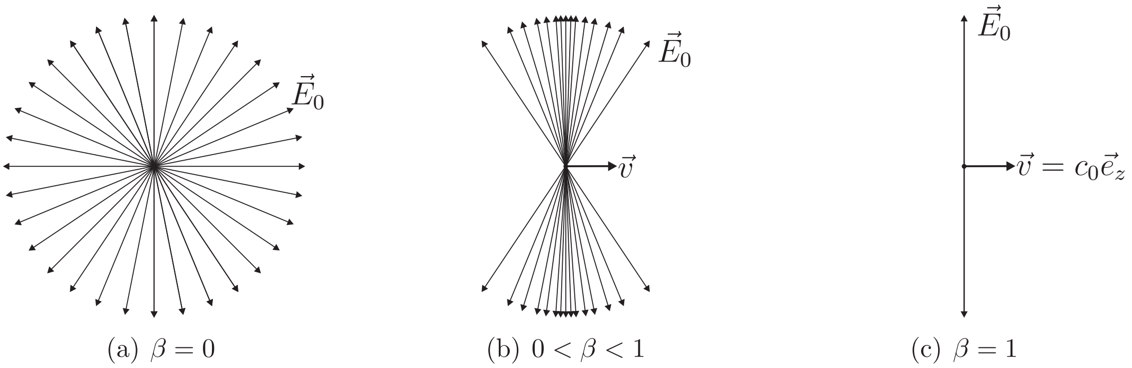

(a) $\beta = 0$

(b) $0 < \beta < 1$

(c) $\beta = 1$

Figure 2.2: The electric field $\vec{E}_0$ of a point-like electric charge (a) at rest, (b) in relativistic motion, and (c) in the ultrarelativistic limit.

In the limit of $\beta = 1$ the spatial extension of the electric and magnetic fields of a point charge contract to a plane perpendicular to the direction of motion at its position $z = c_0 t$:

$$\lim_{\beta\to 1} \vec{E}_0 = \frac{Q}{2\pi\epsilon_0 r}\delta(z - c_0 t)\vec{e}_r \qquad \lim_{\beta\to 1} \vec{B}_0 = \frac{Q}{2\pi\epsilon_0 c_0 r}\delta(z - c_0 t)\vec{e}_\phi. \tag{2.12}$$

The interaction between the two particles due to the space charge effects reduce to zero because the Lorentz-force caused by the electromagnetic fields of Q_1 is zero at the position of the charged particle Q_2 for any $s \neq 0$:

$$\vec{F}_{\text{Lorentz}}(\vec{E}_0, \vec{B}_0, \beta = 1) = 0. \tag{2.13}$$

In order to demonstrate the space charge interaction at high energies, the Lorentz-force caused by Q_1 at a velocity $\vec{v}$ (Fig. 2.3(b)) witnessed by Q_2 is compared to the Lorentz-force at rest (Fig. 2.3(a)) by means of the ratio η which is defined as

$$\eta = \frac{\left|\vec{F}_{\text{Lorentz}}(\vec{E}_0, \vec{B}_0, \beta)\right|}{\left|\vec{F}_{\text{Lorentz}}(\vec{E}_0, \vec{B}_0, \beta = 0)\right|}. \tag{2.14}$$

In the table 2.1, the ratios η for different kinetic energies are given

E_{kin}[MeV]	1	2	5	10
β	0.89	0.969	0.995	0.999
η	$2.9 \cdot 10^{-6}$	$7.25 \cdot 10^{-7}$	$1.16 \cdot 10^{-7}$	$2.9 \cdot 10^{-8}$

Table 2.1: The ratio η for different kinetic energies. With increasing velocity the space charge effects decrease.

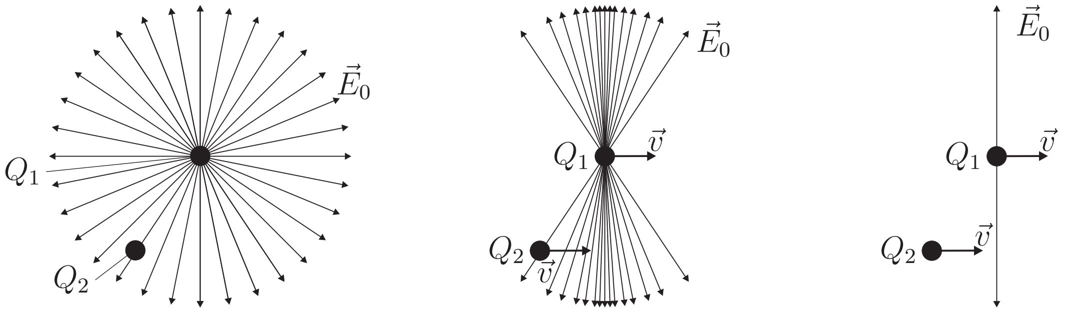

(a) $\beta = 0$, the Lorentz-force is non-zero.

(b) $0 < \beta < 1$, the Lorentz-force is non-zero.

(c) $\beta = 1$, the Lorentz-force is zero.

Figure 2.3: The electric field $\vec{E}_0$ of the charge Q_1 witnessed by the charge Q_2 depending on the velocity $\vec{v}$.

For a given limit of η, the required kinetic energy can be calculated (Tab. 2.2). The kinetic energy of 538.8 MeV is easily achieved for electrons in modern particle accelerators. Therefore, neglecting the space charge interaction at high velocities is a reasonable assumption.

η	10^{-7}	10^{-8}	10^{-9}	10^{-10}	10^{-11}
E_{kin}[MeV]	5.4	17.0	53.9	170.3	538.8

Table 2.2: The kinetic energies for several ratios η.

In the following, it is assumed that all charged particles travel at the speed of light. If the driving charge passes a discontinuity, wake fields are excited. These fields propagate into the half space behind the driving charge and cause a non-vanishing Lorentz-force

$$\vec{F}_{\mathrm{Lorentz}}\left(\vec{r}_1, \vec{r}_2, z_2, t\right) = Q_2 \cdot \left(\vec{E}_s\left(\vec{r}_1, \vec{r}_2, z_2, t\right) + c_0\, \vec{e}_z \times \vec{B}_s\left(\vec{r}_1, \vec{r}_2, z_2, t\right)\right) \tag{2.15}$$

at the position of the witness charge Q_2. The Lorentz-force is integrated along the longitudinal direction. This yields a change in the momentum of the witness charge. Normalizing this change to the product of the driving charge Q_1 and the witness charge Q_2, leads to the *wake function*

$$\vec{w}\left(\vec{r}_1, \vec{r}_2, s\right) = \frac{1}{Q_1\, Q_2} \int\limits_{-\infty}^{\infty} \vec{F}_{\mathrm{Lorentz}}\left(\vec{r}_1, \vec{r}_2, z_2 = c_0 t - s, t\right)\, \mathrm{d}(c_0 t). \tag{2.16}$$

Its unit is usually given as $^{V}/_{pC}$. In the definition of the wake function only point-like charges were considered. Therefore, the wake function is the Green's function of the electromagnetic field solution in the given accelerator structure. If a particle bunch with total charge Q_1 and a given bunch distribution $\lambda(s)$ excites the wake fields, the impact on the witness charge Q_2 is described by the *wake potential* $\vec{W}(s)$. It is defined as the convolution of the wake function with the bunch distribution

$$\vec{W}(s) = \int\limits_{-\infty}^{\infty} \lambda(s - s')\, \vec{w}(s')\, \mathrm{d}s'. \tag{2.17}$$

The vector $\vec{W} = \left(W_{\perp,x}, W_{\perp,y}, W_{\parallel}\right)^T$ consists of three components. Each of these components is a measure for the induced voltage of the bunch witnessed by the trailing charge, normalized to the total bunch charge Q_1. Its unit is $^{V}/_{pC}$ as well. The wake potential can also be obtained directly by integrating the Lorentz-force acting on the witness charge, scaled with the charge Q_1 of the particle bunch

$$\vec{W}\left(\vec{r}_1, \vec{r}_2, s\right) = \frac{1}{Q_1} \int\limits_{-\infty}^{\infty} \left(\vec{E}_s\left(\vec{r}_1, \vec{r}_2, z_2, t\right) + c_0\, \vec{e}_z \times \vec{B}_s\left(\vec{r}_1, \vec{r}_2, z_2, t\right)\right) \mathrm{d}(c_0 t). \tag{2.18}$$

The wake potential $\vec{W}(s)$ can be separated into two parts, $W_{\parallel}$ – the longitudinal wake potential – and $\vec{W}_{\perp}$ – the transverse wake potential. The former describes the impact on the longitudinal dynamics of a witness charge, and the latter on the transverse dynamics, respectively.

The vector resulting from the term $\vec{e}_z \times \vec{B}_s$ in equation (2.18) is oriented perpendicularly to the longitudinal coordinate. Therefore, it has no effect on the longitudinal dynamics of particles traveling on an axis-parallel trajectory

$$W_{\parallel}\left(\vec{r}_1, \vec{r}_2, s\right) = \frac{1}{Q_1} \int\limits_{-\infty}^{\infty} E_z\left(\vec{r}_1, \vec{r}_2, z_2 = c_0 t - s, t\right) \,\mathrm{d}(c_0 t). \tag{2.19}$$

Both components of the wake potential are mutually dependent. Assuming that the particle bunch travels at the speed of light on an axis-parallel trajectory, i.e. the beta-function is constant, the space charge effects which vary as $^1/_{\gamma^2}$ vanish. In this case, the longitudinal and the transverse wake potential are connected via the Panofsky-Wenzel theorem [17]

$$\frac{\partial}{\partial s}\vec{W}_{\perp}\left(x, y, s\right) = -\nabla_{\perp} W_{\parallel}\left(x, y, s\right). \tag{2.20}$$

Thus, it is sufficient to calculate the longitudinal wake potential by equation (2.19). Then, Equation (2.20) allows for the computation of the transverse wake potential.

Two scalar quantities characterize the impact of the wake potential $\vec{W}(s)$ on the longitudinal and transverse dynamics. The *kick factor* $\kappa_{\perp}$ quantifies the deflection of the witness charge Q_2 in the transverse direction. The mean induced voltage seen by the witness charge normalized to its charge Q_2 is called the *total loss factor* k_{loss} [18]

$$k_{\mathrm{loss}} = \int\limits_{-\infty}^{\infty} \lambda(s) W_{\parallel}(s) \,\mathrm{d}s. \tag{2.21}$$

The loss factor multiplied by Q_1 describes the total voltage induced by the particle bunch. Multiplying the loss factor with the charges Q_1 and Q_2 yields the total energy gain of the witness charge Q_2:

$$\Delta E_{Q_2} = Q_2 \cdot Q_1 \cdot k_{\mathrm{loss}}. \tag{2.22}$$

2.2.2 Direct and Indirect Integration

The integral expression given by equation (2.19) defines the longitudinal wake potential, which is evaluated within the limits $-\infty$ and ∞. However, a numerical simulation has to be stopped at a finite distance z_0. This is illustrated in Fig. 2.4. The integral is split into

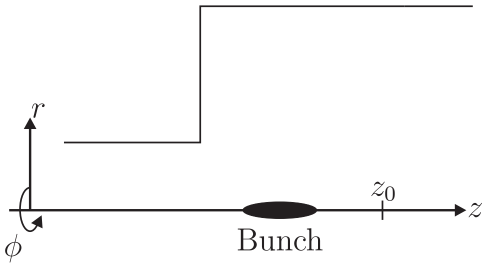

Figure 2.4: The integration of the longitudinal electric fields on the axis stops at the position z_0 when the simulation ends.

two parts

$$W_{\parallel}(s) = \int_{-\infty}^{\infty} \ldots \, \mathrm{d}(c_0 t) = \int_{-\infty}^{z_0} \ldots \, \mathrm{d}(c_0 t) + \underbrace{\int_{z_0}^{\infty} \ldots \, \mathrm{d}(c_0 t)}_{I} \tag{2.23}$$

The first summand in equation (2.23) is integrated directly during the simulation. The longitudinal component of the scattered electric field is zero in front of the discontinuity and the lower limit of the integration is changed to a position located there. However, omitting the second summand I leads to erroneous wake potentials. Therefore, its contribution is evaluated in a so-called 'indirect integration' [19].

There are two different approaches to carry out this task. The integration of the longitudinal electric field along the beam axis to infinity can be transformed into an integration along a perpendicular path C as indicated in Fig. 2.5 [20, 21].

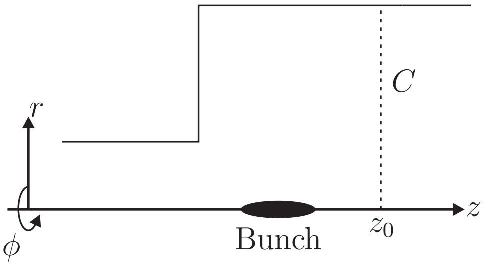

Figure 2.5: The excited electromagnetic fields are integrated along a perpendicular path at the position z_0.

$$I = \int_{z_0}^{\infty} \ldots \, \mathrm{d}(c_0 t) = \int_{C} \left(\vec{E} + c_0 \, \vec{e}_z \times \vec{B} \right) \cdot \mathrm{d}\vec{r} \tag{2.24}$$

For this case the transverse components of $\vec{E}$ and $\vec{e}_z \times \vec{B}$ must not be omitted.

The second approach utilizes a modal expansion of the electromagnetic fields [22, 23]. The fields are monitored at the position z_0 in time. After the direct integration stops, a mode decomposition is performed. The contribution of each mode to the integral I can be calculated analytically.

Chapter 3

Discrete Electrodynamics

Up to this point, continuous electromagnetic fields were described. In order to simulate these fields in accelerator structures a spatial and a temporal discretization of Maxwell's equations is required. In this chapter, first, the spatial discretization is introduced. Following, the temporal discretization is presented. Additionally, the time update scheme for the integration of the fully discretized Maxwell's equations is described and its properties are analyzed.

3.1 The Finite Integration Technique

In 1977, Thomas Weiland developed the *Finite Integration Technique* (FIT) – a convenient technique to discretize Maxwell's equations for the purpose of the numerical computation of electromagnetic fields. The equations (2.3a-2.3d) are discretized in a consistent way and allow for the solution of a large variety of electromagnetic field problems in electrical engineering and physics.

3.1.1 Spatial Discretization

In the FIT, a finite volume of space Ω is discretized utilizing a three dimensional grid G. The grid is defined by grid lines which are parallel to the axes of the coordinate system. Intersections of these grid lines are called nodes P. Along the grid lines and in-between two nodes are the edges L. Four of these edges enclose a cell face A. Six cell faces enclose a cell volume V. These geometric objects are typically referenced by a lexicographic index n throughout this thesis.

A second grid, the dual grid, $\widetilde{G}$ is chosen in such a way, that its edges $\widetilde{L}$ stab the corresponding face of the primary grid G orthogonally. Likewise, the cell faces $\widetilde{A}$ of the dual grid are stabbed orthogonally by the edges of the primary grid. This arrangement of the two grids allows for a convenient description of Maxwell's equations on the staggered dual-orthogonal grid [24].

The detailed construction of the dual-orthogonal grids is determined by the particular coordinate system which is used. In the scope of this thesis, two coordinate systems are considered – the Cartesian coordinate system and the cylindrical coordinate system. In the following, both grids are briefly introduced.

Cartesian Coordinates

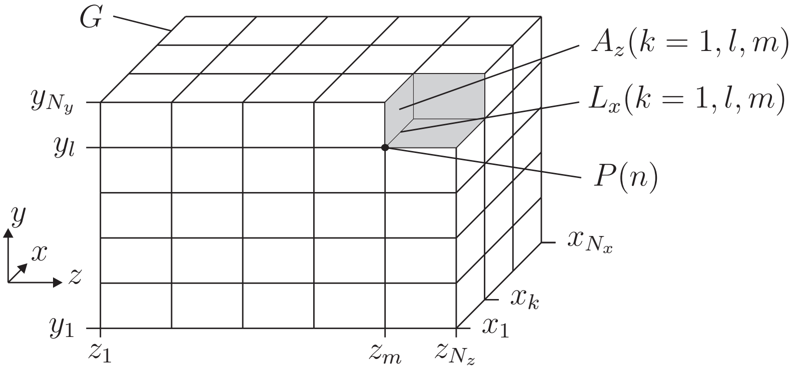

Figure 3.1: The discretization of space by an equidistant mesh resulting in the grid G. A node P is defined by the triple (k,l,m). Here $P(n)$ refers to $(1,l,m)$. Associated to each node are three faces A and three edges L – here $A_z(n)$ and $L_x(n)$ are shown.

The grid consists of N_x, N_y and N_z grid lines in the x-, y- and z-direction of the Cartesian coordinate system. In order to refer to the $N_x \cdot N_y \cdot N_z$ nodes of G, the lexicographic index n is defined as

$$n = 1 + (k-1) \cdot M_x + (l-1) \cdot M_y + (m-1) \cdot M_z, \tag{3.1}$$

with the parameters $M_x = 1$, $M_y = N_x$ and $M_z = N_x \cdot N_y$. Each of the geometric objects introduced above is indexed according to the triple of numbers (k,l,m) or n, respectively. The primary grid G and its components in Cartesian coordinates are illustrated in Fig. 3.1.

Cylindrical Coordinates

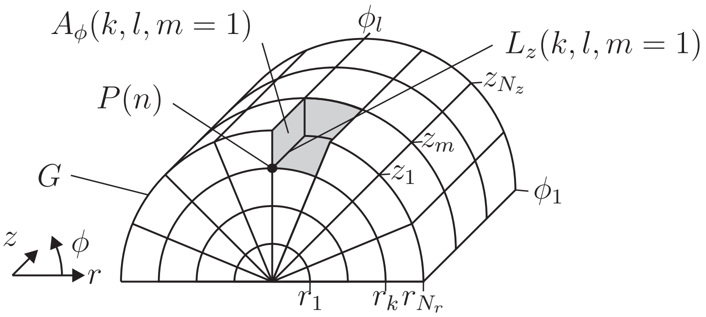

Figure 3.2: The discretization of space utilizing a cylindrical coordinate system resulting in the grid G. A node P is defined by the triple (k,l,m). Here $P(n)$ refers to $(k,l,1)$. Associated to each node are three faces A and three edges L – here $A_\phi(n)$ and $L_z(n)$ are shown.

The grid for cylindrical coordinates is constructed in an analogous way. The index triple (k, l, m) now refers to the r-, ϕ- and z- directions. In Fig. 3.2, the node $P(n)$ is shown. The corresponding edge L_z and the face A_ϕ are additionally depicted.

Both types of grids are used in this thesis for discretizing Ω. However, the Cartesian coordinate system based grid G is considered in the following sections in order to introduce the FIT.

3.1.2 Allocation of Field Values

In the following, the discretization of the continuous field quantities $\vec{E}$, $\vec{D}$, $\vec{H}$, and $\vec{B}$ on a dual-orthogonal Cartesian grid is described. For every edge L on the grid G, an electric grid voltage can be defined by

$$\widehat{e} := \int_L \vec{E}(x, y, z) \cdot \mathrm{d}\vec{s}, \qquad \forall L \in G. \tag{3.2}$$

The integral is not evaluated but the electric grid voltage is used as a state variable of the FIT. No approximation is introduced, and $\widehat{e}$ is an exact representation of the continuous field on the grid edges.

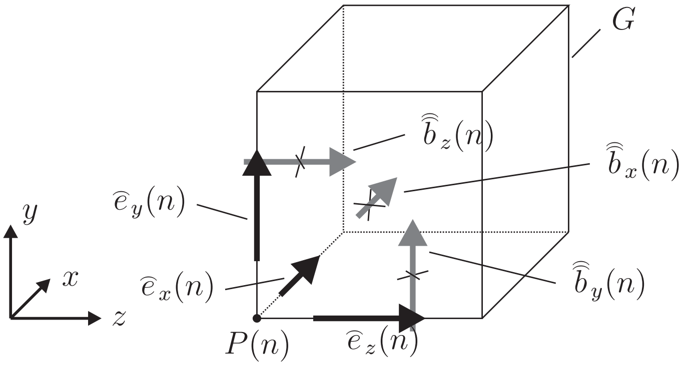

Figure 3.3: A grid cell referred to by the node $P(n)$. The three electric grid voltages $\widehat{e}_x(n)$, $\widehat{e}_y(n)$ and $\widehat{e}_z(n)$ are located on the respective edges. The three magnetic grid fluxes $\widehat{\widehat{b}}_x(n)$, $\widehat{\widehat{b}}_y(n)$ and $\widehat{\widehat{b}}_z(n)$ are positioned on the three faces associated with $P(n)$.

Similarly, the magnetic field induction is integrated over a cell face A of the grid G. Consequently, the definition for the magnetic grid flux $\widehat{\widehat{b}}$ is given as

$$\widehat{\widehat{b}} := \int_A \vec{B}(x, y, z) \cdot \mathrm{d}\vec{A}, \qquad \forall A \in G. \tag{3.3}$$

The two state variables $\widehat{e}$ and $\widehat{\widehat{b}}$ allow for a discrete representation of Faraday's law.

The circulation around a given face, i.e. the edges $L_x(n)$, $L_x(n + M_y)$, $L_y(n)$ and $L_y(n + M_x)$ of the face $A_z(n)$, can be expressed as a sum (correctly signed) of grid voltages (Fig. 3.4)

$$-\frac{\mathrm{d}}{\mathrm{d}t}\widehat{\widehat{b}}_z(n) = \widehat{e}_x(n) + \widehat{e}_y(n + M_x) - \widehat{e}_x(n + M_y) - \widehat{e}_y(n). \tag{3.4}$$

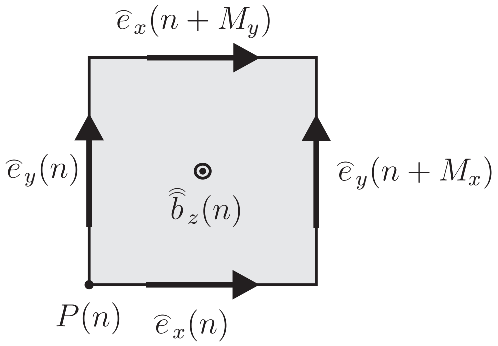

Figure 3.4: The curl operation is demonstrated exemplarily on a grid face assigned to the node $P(n)$ in Fig. 3.1. Adding the proper signed electric grid voltages results in the magnetic grid flux $\widehat{\widehat{b}}_z$ located at the center of the face.

Ampère's law (eqn. (2.4b)) is treated in a similar way. For this purpose, the continuous electric displacement $\vec{D}$ and magnetic field $\vec{H}$ have to be allocated on the dual grid $\widetilde{G}$ in the discretized space Ω.

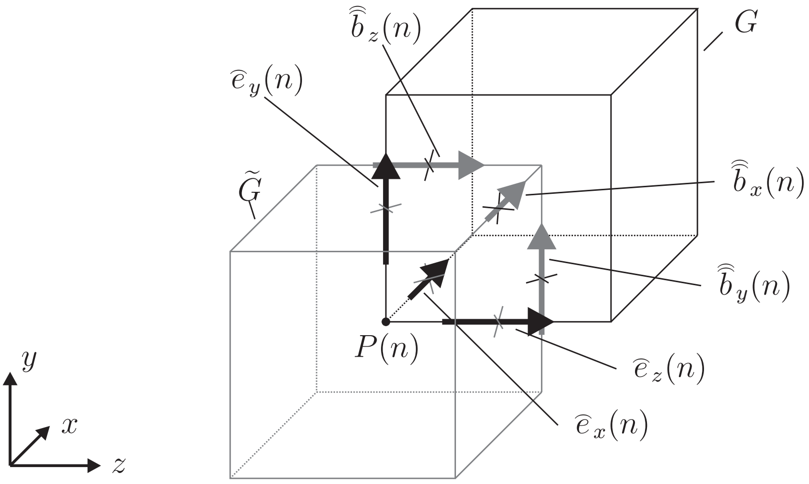

Figure 3.5: The cell of the primary grid G is the same as depicted in Fig. 3.3. In addition, a second cell is shown which is part of the dual grid $\widetilde{G}$. The electric grid voltages stab the faces of the dual grid cell. On the edges of the dual grid cell the magnetic induction is located.

Analogously to the definition of $\widehat{e}$ and $\widehat{\widehat{b}}$, a magnetic voltage is defined as an integral along a dual edge $\widetilde{L}$ and the electric displacement flux is defined as the integral over a dual face $\widetilde{A}$

$$\widehat{h} := \int_{\widetilde{L}} \vec{H}(x,y,z) \cdot \mathrm{d}\vec{s} \tag{3.5}$$

$$\widehat{\widehat{d}} := \int_{\widetilde{A}} \vec{D}(x,y,z) \cdot \mathrm{d}\vec{A} \tag{3.6}$$

Additionally, a discrete representation of the driving current $\vec{J}$ is needed in order to introduce an excitation into the computational domain. It is defined as the integral over a face $\widetilde{A}$ of the dual grid

$$\widehat{\widehat{j}} := \int_{\widetilde{A}} \vec{J}(x, y, z) \cdot \mathrm{d}\vec{A}. \tag{3.7}$$

As a result, Ampère's law in the FIT notation reads as,

$$\frac{\mathrm{d}}{\mathrm{d}t}\,\widehat{\widehat{d}}_z(n) = \widehat{h}_y(n) - \widehat{h}_x(n) - \widehat{h}_y(n - M_x) + \widehat{h}_x(n - M_y) - \widehat{\widehat{j}}_z(n). \tag{3.8}$$

Due to the convenient state variables defined above, the remaining two equations of Maxwell's equations are written as sums of the respective electric grid fluxes (Fig. 3.6) and magnetic grid fluxes (Fig. 3.7)

$$+\,\widehat{\widehat{d}}_x(n) + \widehat{\widehat{d}}_y(n) + \widehat{\widehat{d}}_z(n) - \widehat{\widehat{d}}_x(n - M_x) - \widehat{\widehat{d}}_y(n - M_y) - \widehat{\widehat{d}}_z(n - M_z) \;=\; q(n), \tag{3.9a}$$

$$-\,\widehat{\widehat{b}}_x(n) - \widehat{\widehat{b}}_y(n) - \widehat{\widehat{b}}_z(n) + \widehat{\widehat{b}}_x(n + M_x) + \widehat{\widehat{b}}_y(n + M_y) + \widehat{\widehat{b}}_z(n + M_z) \;=\; 0, \tag{3.9b}$$

with $q(n)$ being the charge of a dual grid cell allocated at the primary grid node $P(n)$ (Fig. 3.6).

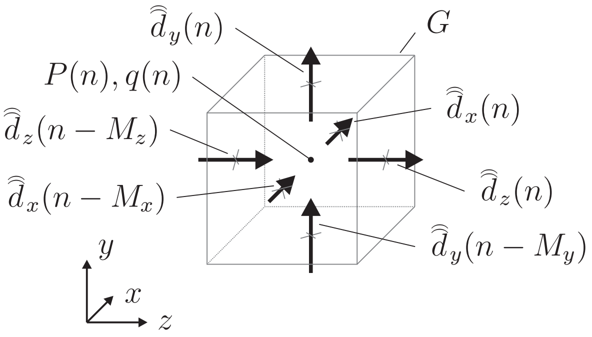

Figure 3.6: Discretization of Gauss' law (eqn. (2.3c)) on the primary grid G. The sum of all electric grid fluxes on the faces of one cell equals the charge located at the primary node $P(n)$.

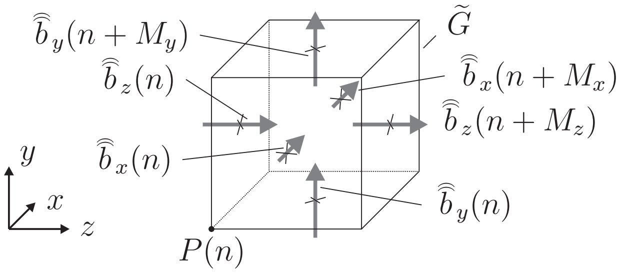

Figure 3.7: Discretization of Gauss' law for magnetism (eqn. (2.3d)) on the dual grid $\widetilde{G}$.

3.1.3 Matrix notation

The electric grid voltages are arranged in a vector of the form

$$\widehat{\mathbf{e}} = \left(\widehat{e}_x(1), \ldots \widehat{e}_x(N_p), \widehat{e}_y(1), \ldots \widehat{e}_y(N_p), \widehat{e}_z(1), \ldots \widehat{e}_z(N_p)\right)^T . \tag{3.10}$$

The vectors $\widehat{\mathbf{h}}$, $\widehat{\widehat{\mathbf{d}}}$, and $\widehat{\widehat{\mathbf{b}}}$ are defined respectively.

The $3 \cdot N_p$ equations of one of Maxwell's equations can be written in a matrix-vector notation. The signs in the sums of equations (3.4 and 3.8) are incorporated as ±1 and 0 entries in matrices $\mathbf{C}$ and $\widetilde{\mathbf{C}}$ respectively. Both equations can now be written as

$$-\frac{\mathrm{d}}{\mathrm{d}t}\widehat{\widehat{\mathbf{b}}} = \mathbf{C}\,\widehat{\mathbf{e}} \tag{3.11a}$$

$$\frac{\mathrm{d}}{\mathrm{d}t}\widehat{\widehat{\mathbf{d}}} = \widetilde{\mathbf{C}}\,\widehat{\mathbf{h}} - \widehat{\widehat{\mathbf{j}}} \tag{3.11b}$$

The matrices $\mathbf{C}$ and $\widetilde{\mathbf{C}}$ describe the circulation around the grid's faces. Thus, they are called the *curl matrix* of the primary grid and the dual grid, respectively. They are the discrete analogons to the continuous curl operator $\nabla\times$. Equation (3.9a) and equation (3.9b) show a similar structure of addition and subtraction signs as well. The N_p equations can again be rewritten as a matrix vector product using two further matrices $\mathbf{S}$ and $\widetilde{\mathbf{S}}$, representing the discrete analogons to the continuous divergence operator $\nabla\cdot$. The entries of these matrices are composed of ±1 and 0. Rewriting equation (3.9a) and equation (3.9b) using the state vectors $\widehat{\widehat{\mathbf{d}}}$ and $\widehat{\widehat{\mathbf{b}}}$ results in

$$\widetilde{\mathbf{S}}\widehat{\widehat{\mathbf{d}}} = \begin{pmatrix} \int\limits_{V(1)} \rho\,\mathrm{d}V \\ \vdots \\ \int\limits_{V(N_p)} \rho\,\mathrm{d}V \end{pmatrix} = \mathbf{q} \tag{3.11c}$$

$$\mathbf{S}\widehat{\widehat{\mathbf{b}}} = 0. \tag{3.11d}$$

where $\mathbf{q}$ is the vector of discrete grid charges. The set of equations (eqns. (3.11a)-(3.11d)) is called the *Maxwell-Grid-Equations*. The topological matrices $\mathbf{C}$, $\widetilde{\mathbf{C}}$, $\mathbf{S}$, and $\widetilde{\mathbf{S}}$ mimic the mathematical properties of the corresponding continuous operators, which leads to the discrete analogies of physical conservation laws, e.g. energy conservation [25]. The relation

$$\mathbf{C} = \widetilde{\mathbf{C}}^T, \tag{3.12}$$

connects the primary and dual grid, and guarantees stability. Furthermore, the following identities can be derived from the topological matrices,

$$\mathbf{C}\widetilde{\mathbf{S}}^T = 0, \tag{3.13a}$$

$$\widetilde{\mathbf{C}}\mathbf{S}^T = 0, \tag{3.13b}$$

$$\mathbf{S}\mathbf{C} = 0, \tag{3.13c}$$

$$\widetilde{\mathbf{S}}\widetilde{\mathbf{C}} = 0. \tag{3.13d}$$

These identities given in equations (3.13a-3.13d) consistently show the preservation of the properties of the continuous operators $\nabla\times$ and $\nabla\cdot$ by the corresponding matrices in the FIT. These properties are: The curl of a gradient field vanishes and the divergence of a rotational field is also always zero.

$$\nabla \times (\nabla\psi) = 0 \qquad \forall\, \psi \in \mathbb{R} \tag{3.14}$$

$$\nabla \cdot (\nabla \times \vec{v}) = 0 \qquad \forall\, \vec{v} \in \mathbb{R}^3 \tag{3.15}$$

Up to this point, the discrete formulations of the FIT are exact. No approximations, and thus no errors, are introduced.

3.1.4 Discrete Constitutive Equations

However, in addition to the Maxwell-Grid-Equations (eqns. (3.11a)-(3.11d)), the constitutive equations (2.9a and 2.9b) have to be discretized.

In order to preserve the physical properties of the electromagnetic fields at material interfaces, homogeneously filled grid cells V of the primary grid G are assumed. Thus, the continuity of the tangential electric field and the normal magnetic induction is guaranteed.

In order to obtain values for the electric permittivity and the magnetic permeability in equations (2.9a-2.9b), the components of the grid displacement vector $\widehat{\widehat{\mathbf{d}}}$ have to be divided by the corresponding components of the electric grid voltage vector $\widehat{\mathbf{e}}$. Otherwise, the component of the magnetic grid voltage vector $\widehat{\mathbf{h}}$ has to be divided by the component of the magnetic grid induction $\widehat{\widehat{\mathbf{b}}}$. Since the state variables $\widehat{e}(n)$, $\widehat{\widehat{d}}(n)$, $\widehat{h}(n)$ and $\widehat{\widehat{b}}(n)$ are defined by integrals, the division can only be carried out with localized values – sampled field values. Thus, averaged values $\overline{\epsilon}(n)$ and $\overline{\mu^{-1}}(n)$ for the discrete permittivity and inverse permeability have to be used by introducing the approximations:

$$\frac{\widehat{\widehat{d}}(n)}{\widehat{e}(n)} = \frac{\int_{\widetilde{A}(n)} \vec{D} \cdot \mathrm{d}\vec{A}}{\int_{L(n)} \vec{E} \cdot \mathrm{d}\vec{s}} \approx \frac{\overline{\epsilon}(n)\,|\widetilde{A}(n)|}{|L(n)|} =: M_{\epsilon}(n) \tag{3.16a}$$

$$\frac{\widehat{h}(n)}{\widehat{\widehat{b}}(n)} = \frac{\int_{\widetilde{L}(n)} \vec{H} \cdot \mathrm{d}\vec{s}}{\int_{A(n)} \vec{B} \cdot \mathrm{d}\vec{A}} \approx \frac{\overline{\mu^{-1}}(n)\,|\widetilde{L}(n)|}{|A(n)|} =: M_{\mu^{-1}}(n) \tag{3.16b}$$

The right hand side is equal to a discrete analogy of the scalar material parameters ϵ and μ^{-1}.

In the staircase approximation, i.e. one type of material filling per volume V, both matrices $M_{\epsilon}(n)$ and $M_{\mu^{-1}}(n)$ are diagonal if a canonical indexing scheme is chosen. Furthermore, these two matrices are the only mathematical objects which carry information about the metric of the grids G and $\widetilde{G}$.

As shown in equation (3.16a), the electric permittivity connects the electric grid voltage allocated on an edge $L \in G$ to the grid displacement located on a face $\widetilde{A} \in \widetilde{G}$. Considering the integral in equation (3.16a) and Fig. 3.8, the electric permittivity, averaged over an

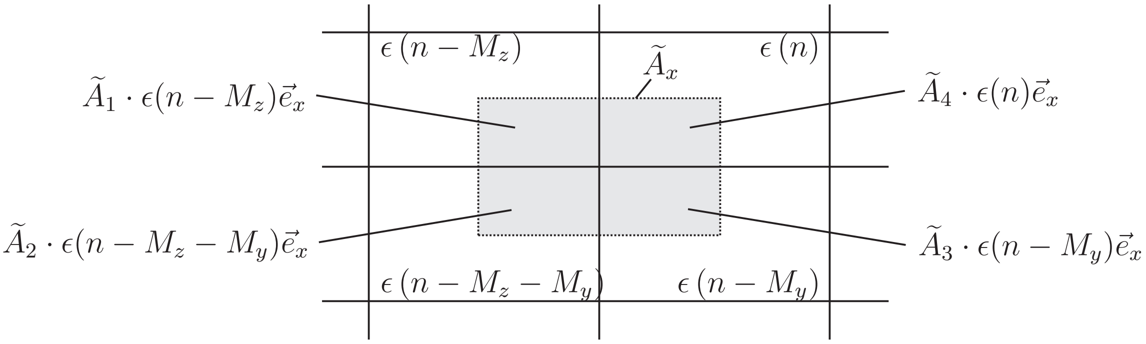

Figure 3.8: The dual cell $\widetilde{A}_x(n)$ intersects with four volumes of the primary grid. Thus, the electric permittivity is calculated as a value averaged over the shaded area. The four areas $\widetilde{A}_1\ldots\widetilde{A}_4$ are homogeneously filled with media $\epsilon(n-M_z)$, $\epsilon(n-M_z-M_y)$, $\epsilon(n-M_y)$ and $\epsilon(n)$.

area, is computed as

$$\begin{aligned}\overline{\epsilon_x}(n) &:= \frac{\int_{\widetilde{A}(n)}\epsilon\,\mathrm{d}A}{\int_{\widetilde{A}(n)}\mathrm{d}A}\\ &= \frac{1}{\widetilde{A}_1+\widetilde{A}_2+\widetilde{A}_3+\widetilde{A}_4}\Big(\quad \epsilon_x(n-M_z)\cdot\widetilde{A}_1\\ &\qquad +\epsilon_x(n-M_y-M_z)\cdot\widetilde{A}_2\\ &\qquad +\epsilon_x(n-M_y)\cdot\widetilde{A}_3\\ &\qquad +\epsilon_x(n)\cdot\widetilde{A}_4\Big).\end{aligned}\tag{3.17}$$

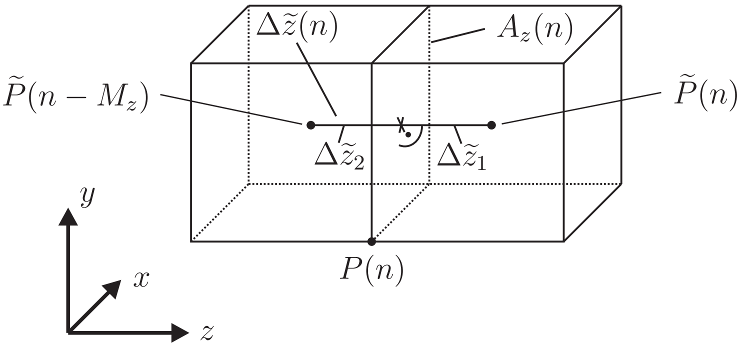

Figure 3.9: The inverse permeability is calculated as a value averaged over an edge $\Delta\widetilde{z}(n)$ which intersects with two primary volumes of G of permeability μ_1 and μ_2, respectively.

The inverse of the magnetic permeability, which connects the magnetic grid flux to the magnetic grid voltage, is calculated by averaging along the edges as shown in Fig. 3.9

$$\overline{\mu_z^{-1}}(n) := \frac{\int_{\widetilde{L}(n)}\mu^{-1}\,\mathrm{d}s}{\int_{\widetilde{L}(n)}\mathrm{d}s} = \frac{\frac{\Delta\widetilde{z}_1}{\mu(n)}+\frac{\Delta\widetilde{z}_2}{\mu(n-M_z)}}{\Delta\widetilde{z}(n)}.\tag{3.18}$$

Using the matrix notation, the two matrices $\mathbf{M}_\epsilon$ and $\mathbf{M}_{\mu^{-1}}$, describe the relations of the electric grid voltages $\widehat{\mathbf{e}}$ to the electric grid fluxes $\widehat{\widehat{\mathbf{d}}}$ and of the magnetic grid fluxes $\widehat{\widehat{\mathbf{b}}}$ to the magnetic grid voltages $\widehat{\mathbf{h}}$

$$\widehat{\widehat{\mathbf{d}}} = \mathbf{M}_{\epsilon}\, \widehat{\mathbf{e}}, \tag{3.19}$$

$$\widehat{\widehat{\mathbf{b}}} = \mathbf{M}_{\mu}\, \widehat{\mathbf{h}}, \tag{3.20}$$

connecting the primary grid G and the dual grid $\widetilde{G}$.

3.1.5 Boundary Conditions and Material Interfaces

Since the Maxwell-Grid-Equations (eqns. (3.11a)-(3.11d)) describe a discrete version of Maxwell's equations (2.3a-2.3d), boundary conditions have to be given in order to solve the boundary value problem.

For example, two possible boundary conditions are the Dirichlet boundary condition and the Neumann boundary condition. The former forces the field solution to specific values on the boundary. The latter forces the normal derivative of the fields at the boundary to a defined value. Additionally, so-called *absorbing boundary conditions* can be introduced. One example for these are the *perfectly matched layer* (PML) boundaries.

All the boundary conditions mentioned above are incorporated via the material matrices $\mathbf{M}_{\epsilon^{-1}}$ and $\mathbf{M}_{\mu^{-1}}$. A PEC boundary, for example, is implemented by using the Dirichlet boundary condition which leads to modified material matrices. Each entry corresponding to an electric grid voltage located on an edge of the PEC boundary is set to zero. Solving Maxwell-Grid-Equations , this leads to voltages automatically fixed to zero, resulting in a zero tangential field component for the electric field at the PEC boundary.

This short section about boundary conditions is intended to remind the reader that they are indispensable for solving any kind of differential equations. Nevertheless, a more detailed description of boundaries and particularly modeling the interface between two different media is given in section 4.4.

3.2 Leapfrog Scheme

In the preceding section, the FIT was introduced and the semi-discrete Maxwell-Grid-Equations were derived (eqns. (3.11a)-(3.11d)). For a fully discretized version of Maxwell's equations, the time derivative has to be discretized as well. The energy conservation is inherently given by the properties of the primary and dual curl matrices of the FIT (eqn. (3.12)). Therefore, the Maxwell-Grid-Equations can be symplectically [26] integrated in time. The simplest explicit time integration scheme is the *leapfrog scheme*. The continuous time derivatives are substituted by the second order accurate central difference quotients

$$\frac{\mathrm{d}}{\mathrm{d}t}\widehat{\mathbf{h}}^{\left(m+\frac{1}{2}\right)} = \frac{\widehat{\mathbf{h}}^{(m+1)} - \widehat{\mathbf{h}}^{(m)}}{\Delta t} + \mathcal{O}\left(\Delta t^2\right), \tag{3.21a}$$

$$\frac{\mathrm{d}}{\mathrm{d}t}\widehat{\mathbf{e}}^{(m+1)} = \frac{\widehat{\mathbf{e}}^{\left(m+\frac{3}{2}\right)} - \widehat{\mathbf{e}}^{\left(m+\frac{1}{2}\right)}}{\Delta t} + \mathcal{O}\left(\Delta t^2\right). \tag{3.21b}$$

This scheme corresponds to an allocation of the vectors $\widehat{\mathbf{e}}$ and $\widehat{\mathbf{h}}$ on a staggered grid in time (Fig. 3.10). The outstanding benefit of the leapfrog scheme is that no auxiliary arrays are required. This results in a computationally efficient time update scheme, because memory overhead is avoided.

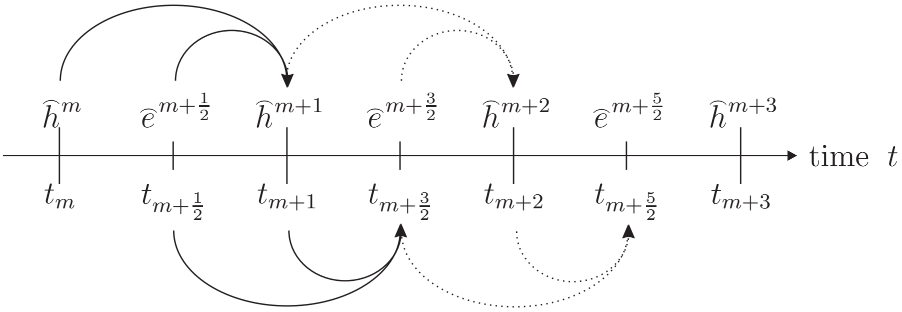

Figure 3.10: Time update scheme for the staggered electromagnetic grid voltages $\widehat{e}$ and $\widehat{h}$. The electric grid voltage is allocated in-between two magnetic grid voltages.

The discretized time derivatives (eqns. (3.21a) and (3.21b)) are substituted into the Maxwell-Grid-Equations (eqns. (3.11a) and (3.11d)). This leads to a recursion formula for the electric and magnetic grid voltages

$$\widehat{\mathbf{h}}^{(m+1)} := \widehat{\mathbf{h}}^{(m)} - \Delta t\, \mathbf{M}_{\mu^{-1}} \mathbf{C}\, \widehat{\mathbf{e}}^{\left(m+\frac{1}{2}\right)}, \tag{3.22a}$$

$$\widehat{\mathbf{e}}^{\left(m+\frac{3}{2}\right)} := \widehat{\mathbf{e}}^{\left(m+\frac{1}{2}\right)} - \Delta t\, \mathbf{M}_{\epsilon}^{-1} \left(\widetilde{\mathbf{C}}\, \widehat{\mathbf{h}}^{(m+1)} - \widehat{\widehat{\mathbf{j}}}^{(m+1)} \right). \tag{3.22b}$$

The leapfrog scheme is a symplectic time update scheme. This means, in particular, that in an accelerator cavity with $\epsilon_r = 1$, $\mu_r = 1$, and perfectly conducting metallic walls no dissipative effects occur. Additionally, multiplying equation (3.22b) with the dual divergence matrix $\widetilde{\mathbf{S}}$ gives

$$\begin{aligned} \widetilde{\mathbf{S}}\mathbf{M}_{\epsilon}^{-1}\, \widehat{\mathbf{e}}^{\left(m+\frac{3}{2}\right)} &= \widetilde{\mathbf{S}}\mathbf{M}_{\epsilon}^{-1}\, \widehat{\mathbf{e}}^{\left(m+\frac{1}{2}\right)} - \Delta t \left(\cancelto{0}{\widetilde{\mathbf{S}}\widetilde{\mathbf{C}}}\, \widehat{\mathbf{h}}^{(m+1)} - \widetilde{\mathbf{S}}\, \widehat{\widehat{\mathbf{j}}}^{(m+1)} \right) \\ 0 &= \frac{\mathbf{q}^{\left(m+\frac{3}{2}\right)} - \mathbf{q}^{\left(m+\frac{1}{2}\right)}}{\Delta t} + \widetilde{\mathbf{S}}\, \widehat{\widehat{\mathbf{j}}}^{(m+1)}, \end{aligned} \tag{3.23}$$

which proves the strict charge conservation of the leapfrog scheme in the time-discrete sense.

3.3 Numerical Dispersion

Nevertheless, the leapfrog scheme being a numerical time-integration scheme introduces numerical dispersion errors. The dispersion relation in the frequency-domain characterizes mathematically these numerical errors. It is obtained by a *von Neumann analysis* [27] which analyzes the propagation of plane electromagnetic waves in the discrete space.

3.3.1 Spatial Discretization

Plane electromagnetic waves

$$\underline{\vec{E}}\left(\vec{r},t\right)=\vec{E}_0\,\exp\left(\mathrm{i}\left(\omega t-\vec{k}\cdot\vec{r}\right)\right) \tag{3.24}$$

in vacuum are solutions of the wave equation

$$\nabla^2\underline{\vec{E}}\left(\vec{r},t\right)-\frac{1}{c_0^2}\frac{\partial^2}{\partial t^2}\underline{\vec{E}}\left(\vec{r},t\right)=0. \tag{3.25}$$

For these waves the continuous dispersion relation

$$\vec{k}^T\cdot\vec{k}=k_x^2+k_y^2+k_z^2=\frac{\omega^2}{c_0^2} \tag{3.26}$$

holds true.

Equation (3.25) is obtained by basic vector analysis operations on Maxwell's equations [28]. However, a plane wave of frequency ω can be described in the discrete space as well. Combining equations (3.11a and 3.11b) leads to the discrete wave equation of the FIT. In the absence of exciting currents and for a non-dissipative medium, this discrete wave equation reduces to the Curl-Curl equation. It reads as follows

$$\mathbf{M}_{\epsilon_0}^{-1}\widetilde{\mathbf{C}}\mathbf{M}_{\mu_0}^{-1}\mathbf{C}\,\widehat{\mathbf{e}}=\omega^2\,\widehat{\mathbf{e}}. \tag{3.27}$$

in the frequency domain. This Curl-Curl-equation is now applied to describe the transport of a plane electromagnetic wave in a basic cell volume $V(n)$ of the grid G (Fig. 3.11). The dispersion properties of the leapfrog scheme are determined for the grid considering this cell volume $V(n)$. Due to the homogeneity of the grid and the free space, properties valid for the whole grid can be derived by considering only one single cell.

The spatial dependency of the plane electromagnetic wave (eqn. (3.24)) separates into three factors

$$\exp\left(-\mathrm{i}\vec{k}\cdot\vec{r}\right)=\exp\left(-\mathrm{i}k_x x\right)\cdot\exp\left(-\mathrm{i}k_y y\right)\cdot\exp\left(-\mathrm{i}k_z z\right). \tag{3.28}$$

Each factor corresponds to a discrete spatial phase factor

$$\underline{\Psi}_x = \exp\left(-\mathrm{i}k_x\Delta x\right), \tag{3.29a}$$

$$\underline{\Psi}_y = \exp\left(-\mathrm{i}k_y\Delta y\right), \tag{3.29b}$$

$$\underline{\Psi}_z = \exp\left(-\mathrm{i}k_z\Delta z\right), \tag{3.29c}$$

These phase factors depend on the edge lengths Δx, Δy, and Δz of a volume $V(n)$ of the grid G.

A plane electromagnetic wave propagating in a grid cell is described by the voltages allocated on the edges of the corresponding node $P(n)$. The propagation of the wave is represented by a multiplication of the grid voltages with the phase factors (eqns. (3.29a)-(3.29c)).

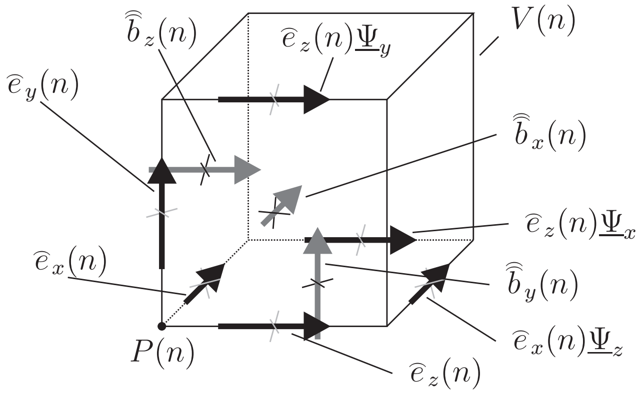

Figure 3.11: The voltages corresponding to a node $P(n)$ of the grid G are transported via multiplication with direction dependent phase factors.

Faraday's law is written for the bottom face in Fig. 3.11 as

$$\begin{aligned}-\frac{\mathrm{d}}{\mathrm{d}t}\overset{\frown}{\overset{\frown}{b}}_y(n) &= \overset{\frown}{e}_z(n)+\overset{\frown}{e}_x(n)e^{-ik_z\Delta z}-\overset{\frown}{e}_z(n)e^{-ik_x\Delta x}-\overset{\frown}{e}_x(n)\\ &= \overset{\frown}{e}_z(n)\left(1-e^{-ik_x\Delta x}\right)+\overset{\frown}{e}_x(n)\left(-1+e^{-ik_z\Delta z}\right). \qquad (3.30a)\end{aligned}$$

For the remaining magnetic grid inductions $\overset{\frown}{\overset{\frown}{b}}_x(n)$ and $\overset{\frown}{\overset{\frown}{b}}_z(n)$, similar expressions are derived. For the primary volume $V(n)$ the relation of the three magnetic grid inductions and the electric grid voltages is written in matrix-vector form

$$\underbrace{\begin{pmatrix}0 & 1-e^{-ik_z\Delta z} & e^{-ik_y\Delta y}-1\\ e^{-ik_z\Delta z}-1 & 0 & 1-e^{-ik_x\Delta x}\\ 1-e^{-ik_y\Delta y} & e^{-ik_x\Delta x}-1 & 0\end{pmatrix}}_{\mathbf{C}_{\text{local}}}\begin{pmatrix}\overset{\frown}{e}_x(n)\\ \overset{\frown}{e}_y(n)\\ \overset{\frown}{e}_z(n)\end{pmatrix}=-\mathrm{i}\omega\begin{pmatrix}\overset{\frown}{\overset{\frown}{b}}_x(n)\\ \overset{\frown}{\overset{\frown}{b}}_y(n)\\ \overset{\frown}{\overset{\frown}{b}}_z(n)\end{pmatrix} \qquad (3.31)$$

The local curl matrix in equation (3.31) consists of the spatial phase factors describing the propagation of the electromagnetic wave. In a next step, the magnetic induction in equation (3.31) is expressed via equation (3.20) by the magnetic grid voltages. Applying Ampere's grid law (eqn. (3.11b)) and the equation (3.19) leads to the local Curl-Curl equation for the grid cell.

$$\mathbf{M}^{-1}_{\epsilon_0,\text{local}}\widetilde{\mathbf{C}}_{\text{local}}\mathbf{M}^{-1}_{\mu_0,\text{local}}\mathbf{C}_{\text{local}}\begin{pmatrix}\overset{\frown}{e}_x(n)\\ \overset{\frown}{e}_y(n)\\ \overset{\frown}{e}_z(n)\end{pmatrix}=\omega^2\begin{pmatrix}\overset{\frown}{e}_x(n)\\ \overset{\frown}{e}_y(n)\\ \overset{\frown}{e}_z(n)\end{pmatrix}. \qquad (3.32)$$

The solutions for the three eigenvalues of the matrix in equation (3.32) are the static solution $\lambda_1 = 0$ and the twice-degenerate eigenvalues

$$\lambda_{2,3}=\omega^2=c_0^2\left[\left(\frac{\sin\left(\frac{k_x\Delta x}{2}\right)}{\frac{\Delta x}{2}}\right)^2+\left(\frac{\sin\left(\frac{k_y\Delta y}{2}\right)}{\frac{\Delta y}{2}}\right)^2+\left(\frac{\sin\left(\frac{k_z\Delta z}{2}\right)}{\frac{\Delta z}{2}}\right)^2\right]. \qquad (3.33)$$

The eigenvalues λ_2 and λ_3 correspond to the two possible polarizations of a plane wave. They describe the properties of the propagation of the electromagnetic wave in the grid

G and depend on the spatial spacing as well as on the direction of the propagation itself. One important property of equation (3.33) is revealed if the spatial spacings Δx, Δy and Δz tend to zero. Due to

$$\lim_{\Delta j \to 0} \frac{\sin\left(k_j \frac{\Delta j}{2}\right)}{\frac{\Delta j}{2}} = k_j \qquad (j = x, y, z) \tag{3.34}$$

equation (3.33) transforms to the continuous spatial dispersion relation (eqn. (3.26)), proving a consistent spatial discretization.

3.3.2 Temporal Discretization

The grid dispersion relation in the time-domain for the fully discretized Maxwell-Grid-Equations is sought. Thus, the time dependency of the wave has to be taken into account as well.

The plane electromagnetic wave (eqn. (3.24)) has a time dependency

$$\underline{\vec{E}}\,(\vec{r}, t) = \vec{E}_0 \exp\left(-\mathrm{i}\vec{k} \cdot \vec{r}\right) \exp\left(\mathrm{i}\omega t\right), \tag{3.35}$$

which corresponds to a temporal phase factor

$$\underline{\Psi}_t = \exp\left(\mathrm{i}\omega \Delta t\right), \tag{3.36}$$

with respect to a time step Δt. All electromagnetic quantities on the grids G and $\widetilde{G}$ are transported in time by the multiplication with the phase factor $\underline{\Psi}_t$. The second derivative with respect to time in the wave equation (eqn. (3.25)) is discretized using this phase factor

$$\frac{\mathrm{d}^2}{\mathrm{d}t^2} \xrightarrow{\textit{discretized}} \frac{\left(e^{i\omega\Delta t} - 1\right)^2}{e^{i\omega\Delta t} \Delta t^2}. \tag{3.37}$$

The right hand side in equation (3.37) corresponds to the eigenvalue of the temporal discretization in the leapfrog scheme. It can be set equal to the eigenvalues $\lambda_{2,3}$ of the spatial discretization in equation (3.33), leading to the grid dispersion relation in the time-domain

$$\left(\frac{\sin\left(\frac{k_x \Delta x}{2}\right)}{\frac{\Delta x}{2}}\right)^2 + \left(\frac{\sin\left(\frac{k_y \Delta y}{2}\right)}{\frac{\Delta y}{2}}\right)^2 + \left(\frac{\sin\left(\frac{k_z \Delta z}{2}\right)}{\frac{\Delta z}{2}}\right)^2 = \frac{1}{c_0^2} \left(\frac{\sin\left(\frac{\omega \Delta t}{2}\right)}{\frac{\Delta t}{2}}\right)^2. \tag{3.38}$$

The grid spacings Δx, Δy, and Δz of G are connected to the time discretization Δt and the direction of the propagation $\vec{k}$. Again, equation (3.34) can be applied. In the limit of infinite small step sizes in space and time, the grid dispersion relation in the time-domain tends to the continuous dispersion relation, proving a consistent discretization in space and time.

3.3.3 Stability

In order to obtain a plane electromagnetic wave with a bounded limit for the amplitude, ω has to be an element of $\mathbb{R}$. This is guaranteed if the square of the trigonometric function sine in equation (3.38) is bounded as

$$\left(\sin\left(\frac{\omega\,\Delta t}{2}\right)\right)^2 \leq 1 \quad \forall\omega\in\mathbb{R}. \tag{3.39}$$

Now, the remaining sine functions in equation (3.38) are approximated by an upper limit of 1 for all possible $k_x, k_y, k_z \in \mathbb{R}$. From this follows an upper limit for the maximum stable time step $\Delta t_{\max}$ of the leapfrog scheme depending on the spatial step sizes

$$\Delta t \leq \Delta t_{\max} = \frac{1}{c_0\sqrt{\frac{1}{\Delta x^2}+\frac{1}{\Delta y^2}+\frac{1}{\Delta z^2}}}. \tag{3.40}$$

This relation is called the Courant-Friedrichs-Levy criterion (CFL). Strictly speaking, the CFL criterion is only valid for homogeneous material distributions and equidistant grids, neglecting any boundary conditions, meaning an infinitely large grid. For arbitrary spatial step sizes Δx, Δy, and Δz, the following estimate for an upper time step limit is given by

$$\Delta t_{\max} \leq \min_j\left\{\frac{1}{c_0\sqrt{\frac{1}{\Delta x_j^2}+\frac{1}{\Delta y_j^2}+\frac{1}{\Delta z_j^2}}}\right\} \qquad \forall j\in\{1,N_p\}. \tag{3.41}$$

In order to visualize the stability criterion the Courant number is defined as

$$\nu_c = \frac{\Delta t}{\min_j\left\{\frac{1}{c_0\sqrt{\frac{1}{\Delta x_j^2}+\frac{1}{\Delta y_j^2}+\frac{1}{\Delta z_j^2}}}\right\}} \qquad \forall j\in\{1,N_p\}. \tag{3.42}$$

The graphs in Fig. 3.12 show the normalized numerical phase velocity of a plane electromagnetic wave on a 2D grid versus ν_c. The direction is characterized by the angle ϕ being defined as

$$\phi = \sphericalangle\left(\vec{k},\vec{e}_z\right). \tag{3.43}$$

A Courant number $\nu_c = 1$ leads to a normalized numerical phase velocity with the maximum value equal to 1. A Courant number smaller than 1 decreases the maximum velocity of the wave on the grid. Whereas a Courant number larger than 1 leads to a maximum velocity larger than the speed of light, violating the CFL.

3.3.4 Dispersion Properties

In order to give a graphical representation of the grid dispersion relation in time-domain, the phase velocity

$$v_{\text{phase}} = \frac{\omega}{|\vec{k}|} \tag{3.44}$$

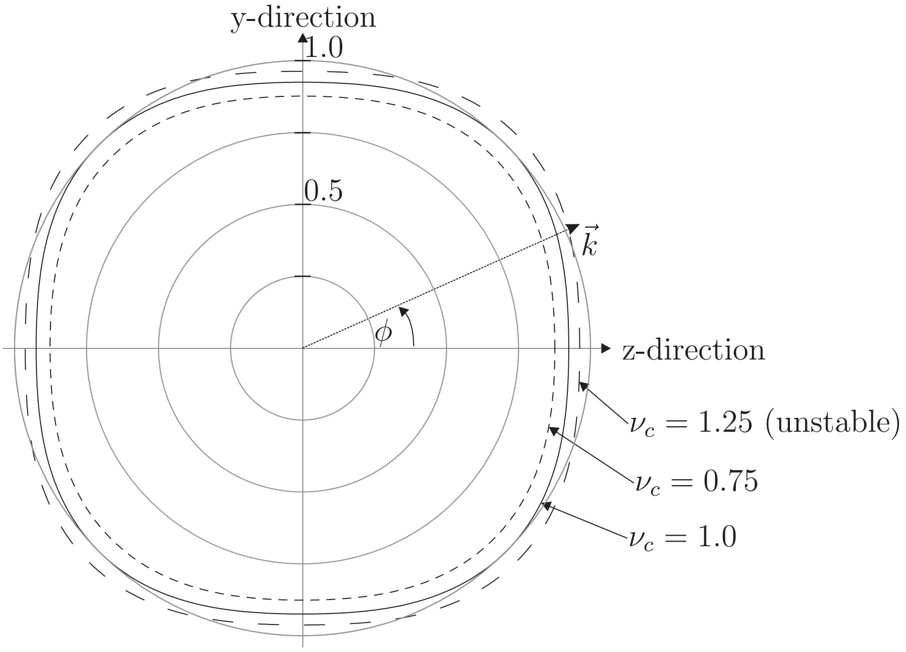

Figure 3.12: Polar plot of the normalized numerical phase velocity of a plane electromagnetic wave characterized by the wave vector $\vec{k}$ propagating through a 2D grid versus the Courant number. The angle ϕ identifies the direction of propagation with respect to $\vec{e}_z$.

is calculated using the eigenvalues corresponding to the spatial (eqn. (3.33)) and the temporal (eqn. (3.37)) discretization, respectively. The difference of these two phase velocities characterizes the numerical dispersion error of the leapfrog scheme. The difference is normalized to its maximum and plotted in Fig. 3.13 for all directions in a 2D plane:

$$\vec{k} = \begin{pmatrix} k_y \\ k_z \end{pmatrix} = |\vec{k}| \begin{pmatrix} \cos\phi \\ \sin\phi \end{pmatrix} \qquad 0 \leq \phi < 2\pi. \tag{3.45}$$

Three different Courant numbers ν_c are chosen to illustrate the dispersion properties of the leapfrog scheme (Fig. 3.13). Both Courant numbers smaller than 1 lead to a numerical dispersion error in all directions. The maximum of 1 stands against a minimum of 0.45 and 0.32 respectively. Only the Courant number $\nu_c = 1$ leads to a particularly outstanding result. The numerical dispersion error still has its maximum of 1, but it is reduced to zero for certain directions on the grid. These directions with zero numerical dispersion errors are

$$(2n-1) \cdot \frac{\pi}{4} \qquad n = 1, 2, 3, 4. \tag{3.46}$$

The time step corresponding to $\nu_c = 1$ equals the maximum time step allowed by the CFL criterion and is often referred to as the *magic time step*.

The dispersion-free directions are shown in Fig. 3.14 for different wave numbers of the plane wave solution. The magic time step allows for a numerical phase velocity c_0 in the dispersion-free directions for all three wave vectors $\vec{k}$. Despite this, in all other directions, e.g. along the z-axis, the numerical phase velocity depends on the wavelength of the plane electromagnetic wave.

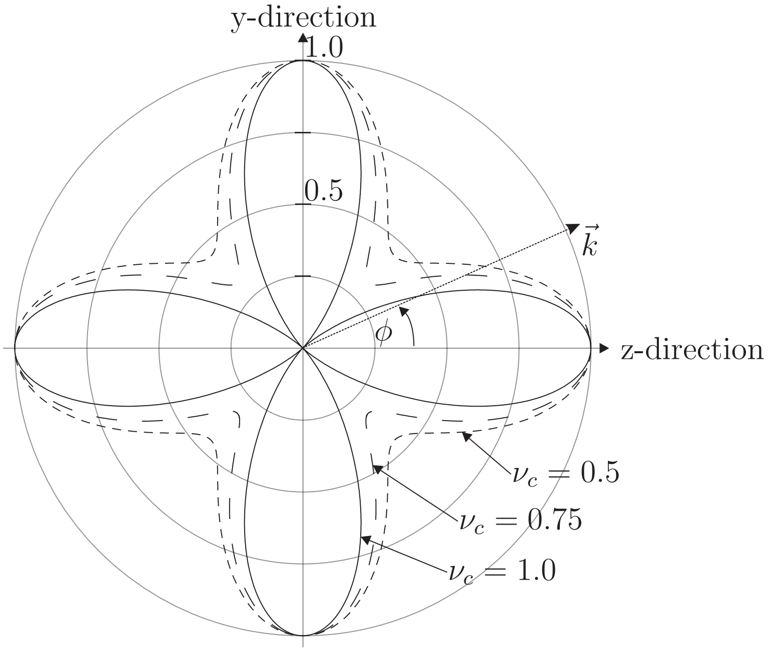

Figure 3.13: Polar plot of the normalized numerical dispersion error for a plane electromagnetic wave characterized by the wave vector $\vec{k}$ propagating through a 2D grid for different Courant numbers ν_c. The angle ϕ identifies the direction of the propagation with respect to $\vec{e}_z$.

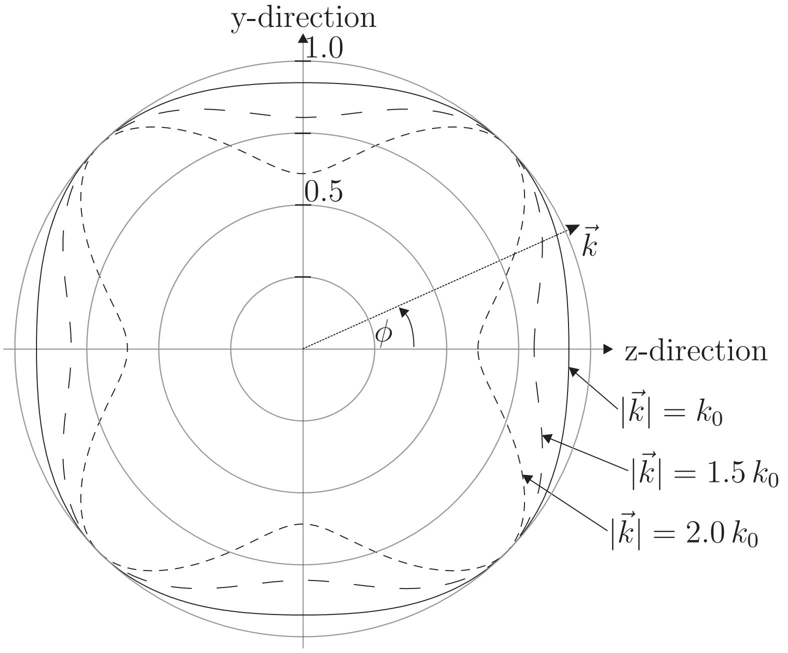

Figure 3.14: Polar plot of the normalized numerical phase velocity of a plane electromagnetic wave characterized by the wave vector $\vec{k}$ propagating through a 2D grid versus different absolute values of the wave vector. The angle ϕ identifies the direction of propagation with respect to $\vec{e}_z$. The time step is $\Delta t = \Delta t_{\max}$.

Chapter 4

Algorithm

The numerical calculation of wake fields is a challenging problem. The large dimensions of the accelerator structures compared to the short particle bunches paired with the demand for accurate results are the crucial points in writing a computer code for this task.

The large amount of computer memory which is necessary to simulate a whole accelerator structure at a sufficiently high resolution can be dealt with by the *Moving Window Technique* [29]. Here, a window co-moving with the particle bunch at the speed of light is considered. Only the geometrical details within this window have to be stored. This technique reduces the memory demands to an acceptable level. However, the moving window requires zero numerical dispersion at least in the propagation direction of the bunch. If dispersion errors occur, the velocity of the electromagnetic fields in the direction of the bunch motion can be lower or nonphysically higher than the speed of light. These are numerical artifacts which are introduced by the applied time integration scheme. For example, electromagnetic fields which travel faster than the bunch are reflected at the leading front of the moving window. Causality is clearly violated and errors are accumulated which spoils the result for the wake fields and the wake potentials.

Additionally, the discretization of the material interface of the accelerator structure is an important task. The staircase approximation method is easy to implement and low in computational costs. But it is very inaccurate at low resolutions. Conformal boundary approximation methods allow for a more accurate discretization of the material interface. Unfortunately, they usually increase the computational costs of the computer code.

Finally, the parallelization of computer codes allows for simulating electromagnetic fields in even larger structures. In Tab. 4.1 a list of computer codes is presented in chronological order which were developed for the purpose of wake field calculations. Early codes as TBCI and MAFIA already made use of the moving window technique. These codes were not dispersion-free. Also, the conformal discretization of the material interface is missing. The parallelization of computer codes did not play a role at that time. Later on, for the simulation of electromagnetic fields excited by short bunches, dispersion-free codes were absolutely necessary. For this reason, ECHO with zero numerical dispersion in the direction of the bunch motion was developed. ECHO is also capable of a conformal boundary approximation. One of the latest developments is the code PBCI. Here, the dispersion-free

Code	Dispersion-free	Moving Window	Conformal	Parallel
TBCI	−	+	−	−
MAFIA	−	+	−	−
ABCI	−	+	−	−
ECHO	+	+	+	−
CST Particle Studio	−	−	+	−
PBCI	+	+	−	+

Table 4.1: List of wake field codes and their properties in chronological order.

propagation of fields is combined with the moving window technique. Moreover, PBCI is a parallelized code. Electromagnetic field simulations at high resolutions as well as for large structures are now possible.

In the previous chapter, the spatial and temporal discretization of Maxwell's equations were discussed. It became apparent that numerical dispersion errors deteriorate the accuracy of the results. In this chapter, an algorithm to overcome the numerical dispersion errors in the special case of the computation of longitudinal wake potentials is discussed. Advantage is taken of the dispersion properties of the leapfrog scheme in the discrete space. The moving window technique and several boundary approximation methods are implemented. Additionally, the excitation of fields and the initial fields for the leapfrog scheme are described. This results in a code which features three of the properties given in Tab. 4.1. The parallelization of the code is omitted in this work.

4.1 Utilizing Grid Properties

As shown in the previous chapter, the numerical dispersion errors of the leapfrog scheme have a directional dependency. In order to benefit from this, the dispersion-free direction of the grid is aligned to the preferred direction of an accelerator structure – the direction of bunch motion [30, 31, 32]. Below, the construction of such a rotated grid using appropriate coordinate transformations is introduced.
Furthermore, the excitation of the fields and the boundary approximation of a given surrounding structure are described. This leads to the implementation of an algorithm which is capable of calculating longitudinal wake potentials, avoiding the accumulation of numerical dispersion errors.

Consider a position vector $\vec{p}$ which describes an arbitrary point P on the Cartesian grid G by a set of coordinates (p_x, p_y, p_z) with respect to the base vectors $\vec{e}_x$, $\vec{e}_y$, and $\vec{z}$

$$\vec{p} = p_x\vec{e}_x + p_y\vec{e}_y + p_z\vec{e}_z. \tag{4.1}$$

The point P in the frame K (Fig. 4.1) is described in another frame K^{rot} by a different set of coordinates $\left(p_x^{\mathrm{rot}}, p_y^{\mathrm{rot}}, p_z^{\mathrm{rot}}\right)$, resulting in the new position vector $\vec{p}^{\mathrm{rot}}$ (Fig. 4.2). These new coordinates are obtained by an orthogonal transformation $\mathbf{R}$. The point P remains fixed with respect to the origin of both frames K and K^{rot}. Therefore, the base vectors have to be rotated in order to obtain the new coordinates for P^{rot}.

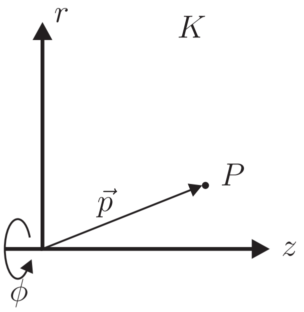

Figure 4.1: Point P and its position vector in the frame K representing the r/z-plane of a cylindrically symmetric coordinate system.

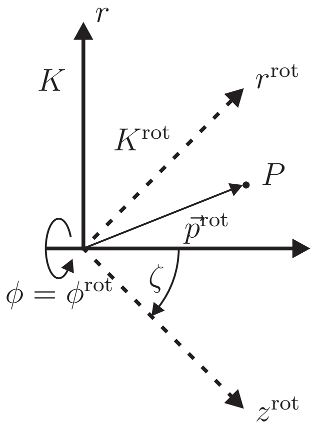

Figure 4.2: The frame K from Fig. 4.1 is rotated by an angle ζ in order to obtain K^{rot}. The new position vector $\vec{p}^{\mathrm{rot}}$ describes P in K^{rot}.

Throughout this thesis, structures exhibiting a cylindrical symmetry are described in an (r, ϕ, z)-coordinate system. This is referred to as *2D*. Arbitrary structures are described in a Cartesian coordinate system with coordinates (x, y, z). This is referred to as *3D*.

In 2D, the r/z-plane of the cylindrically symmetric coordinate system is rotated using a 2×2 rotation matrix $\mathbf{R}_{\mathrm{2D}}$ which is applied to the grid G, i.e. to its base vectors $\vec{e}_r$ and $\vec{e}_z$. The resulting base vectors

$$\vec{e}_j^{\,\mathrm{rot}} = \mathbf{R}_{\mathrm{2D}}\, \vec{e}_j \qquad j = \{r, z\} \tag{4.2}$$

define a new rotated grid G^{rot}. The angle ζ defining the rotation $\mathbf{R}_{\mathrm{2D}}$ is chosen such, that the normalized diagonal $\frac{1}{|\vec{d}^{\mathrm{rot}}|}\vec{d}^{\mathrm{rot}}$ of a rotated grid cell of G^{rot} equals $\vec{e}_z$ of the grid G

$$\frac{1}{|\vec{d}^{\mathrm{rot}}|}\vec{d}^{\mathrm{rot}} = \frac{1}{\sqrt{2}} \begin{pmatrix} 1 \\ 1 \end{pmatrix}\Bigg|_{G^{\mathrm{rot}}} = \vec{e}_z\big|_G \,. \tag{4.3}$$

The resulting rotated grid G^{rot} is illustrated in Fig. 4.3.

Rotating a grid in 3D is conducted by defining a 3×3 rotation matrix $\mathbf{R}_{\mathrm{3D}}$ which allows for transforming the three Cartesian base vectors from the frame K to K^{rot}.

$$\vec{e}_j^{\,\mathrm{rot}} = \mathbf{R}_{\mathrm{3D}}\, \vec{e}_j \qquad j = \{x, y, z\} \tag{4.4}$$

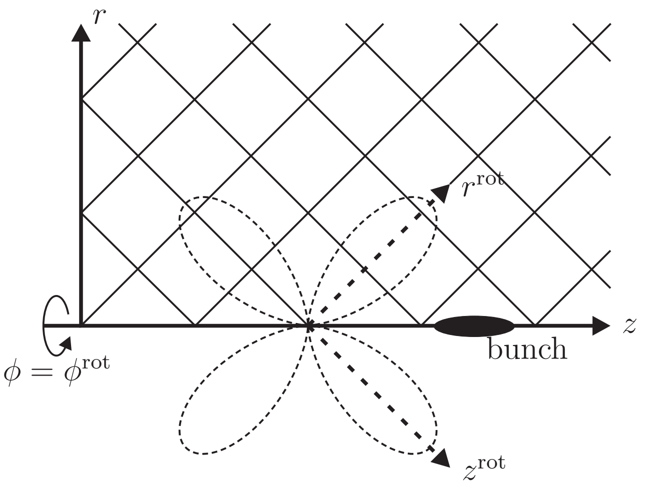

Figure 4.3: The non-rotated base vectors $\vec{e}_r$ and $\vec{e}_z$ and the two rotated base vectors $\vec{e}_r^{\,\text{rot}}$ and $\vec{e}_z^{\,\text{rot}}$ are shown. Additionally, the numerical dispersion error for a Courant factor (eqn. (3.42)) of 1.0 from Fig. 3.13 is shown in relation to the rotated grid.

The angles defining $\mathbf{R}_{3\text{D}}$ are chosen as such, that the normalized diagonal of the rotated grid cell equals $\vec{e}_z$

$$\frac{1}{|\vec{d}^{\,\text{rot}}|}\vec{d}^{\,\text{rot}} = \frac{1}{\sqrt{3}}\left.\begin{pmatrix}1\\1\\1\end{pmatrix}\right|_{G^{\text{rot}}} = \vec{e}_z|_G\,. \tag{4.5}$$

The base vectors in the non-rotated frame K, the rotated base vectors in K^{rot} and one mesh cell of the rotated 3D grid are depicted in Fig. 4.4.

Recalling the dispersion properties of the leapfrog scheme in the discrete space derived in the previous chapter shows the great advantage of the rotated grid. Choosing the correct angles for $\mathbf{R}_{2\text{D}}$ and $\mathbf{R}_{3\text{D}}$ respectively, allows for the alignment of the dispersion-free direction with an arbitrary direction on the non-rotated grid, e.g. the direction of the bunch propagation $\vec{e}_z$. Electromagnetic fields propagating along this direction do not exhibit numerical dispersion errors.

In order to implement a rotated grid in discrete simulations, the electromagnetic fields and thus Maxwell's equations have to be described in the rotated frame K^{rot}. Maxwell's equations are invariant under rotations. The dot product in equations (2.5a and 2.5b) equals the same values in the frames K and K^{rot}. Furthermore, the cross product in the remaining two equations (eqns. (2.5c)-(2.5d)) is invariant as well. A detailed proof is given in the appendix E.

From a physical point-of-view, it is of no relevance whether a long accelerator structure is described on a rotated grid or a rotated accelerator structure is described in a standard non-rotated grid. Simulating an accelerator structure which is rotated relatively to the direction of beam motion in MAFIA would lead to a waste of memory. Therefore, a dedicated implementation of the rotated grid approach in a numerical scheme is required.

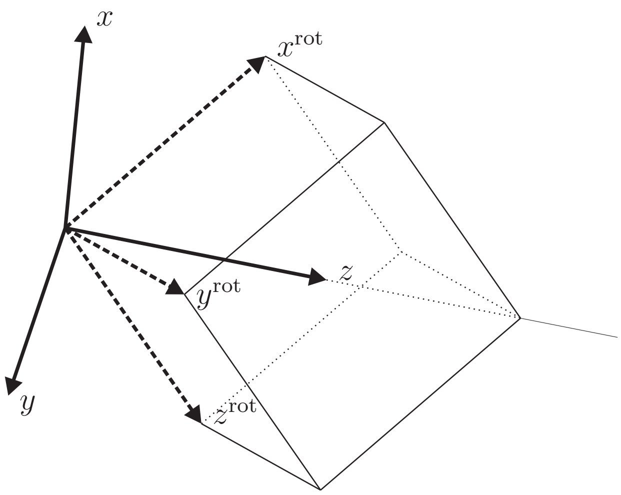

Figure 4.4: The non-rotated and the rotated frames K and K^{rot} are shown. $\vec{e}_x$ and $\vec{e}_y$ are rotated by an angle of $-45°$ about $\vec{e}_z$. Afterwards a rotation of $-54.7°$ about $\vec{e}_y$ is applied. For reasons of clarity, a complete rotated mesh cell with equally long edges is added to the figure.

4.1.1 Resolution and Degrees of Freedom

The memory cost for a numerical simulation strongly depends on the spatial spacing of the employed grid. Two characteristic spacings have to be considered, i.e. the spatial spacing of the grid L and the effective spacing determining the sampling resolution of the excitation bunch L_{b}. The spatial spacings L and L^{rot} are given by the edge length of the non-rotated grid and the rotated grid as well (Fig. 4.5). The number of *degrees of freedom* in 2D, for both types of grids is proportional to the square of the inverse of these spacings

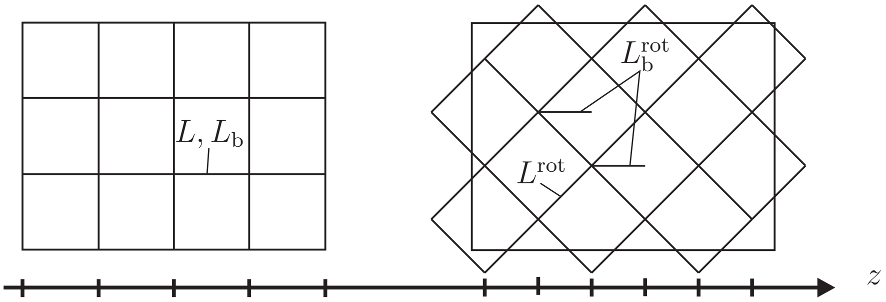

Figure 4.5: The spatial spacings L and L^{rot} and the sampling spacings L_{b} and $L_{\mathrm{b}}^{\mathrm{rot}}$ for the sampling of the bunch in a non-rotated and a rotated 2D grid.

$$N_{\mathrm{DoF}}^{\mathrm{2D}} \propto \left(\frac{1}{L}\right)^2, \tag{4.6}$$

$$N_{\mathrm{DoF}}^{\mathrm{2D,rot}} \propto \left(\frac{1}{L^{\mathrm{rot}}}\right)^2. \tag{4.7}$$

The number of sampling points for a bunch with a *root mean square* (RMS) length σ is defined by

$$N_{\mathrm{b}}^{\mathrm{2D}} = \frac{\sigma}{L_{\mathrm{b}}} = \frac{\sigma}{L}, \tag{4.8}$$

$$N_{\mathrm{b}}^{\mathrm{2D,rot}} = \frac{\sigma}{L_{\mathrm{b}}^{\mathrm{rot}}} = \frac{\sigma}{L^{\mathrm{rot}}} \cdot \sqrt{2}, \tag{4.9}$$

for the non-rotated and the rotated grid type, respectively. Thus, while the number of degrees of freedom for the two types of grids is the same, the number of sampling points for the RMS bunch length σ on the rotated grid is larger by a factor of $\sqrt{2}$ compared to the non-rotated grid.

Vice versa, if the number of sampling points is required to be equal on both grids

$$N_{\mathrm{b}}^{\mathrm{2D}} \overset{!}{=} N_{\mathrm{b}}^{\mathrm{2D,rot}}, \tag{4.10}$$

the spatial spacing of the rotated grid becomes larger by a factor of $\sqrt{2}$ compared to the spatial spacing of the non-rotated grid. Therefore, the number of degrees of freedom is smaller than for the non-rotated grid by a factor of 2.

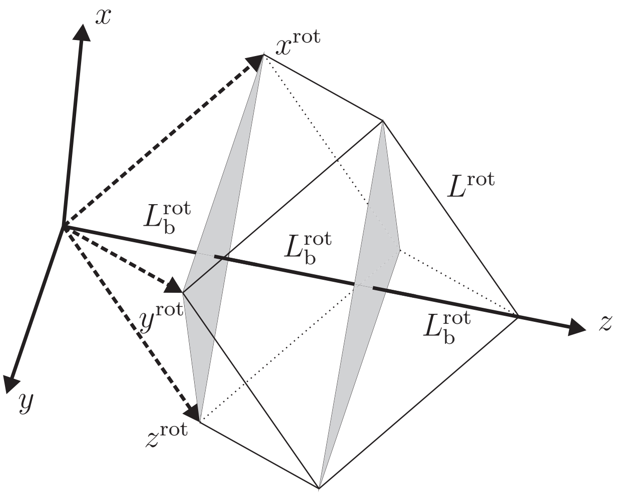

Figure 4.6: The spatial spacing L^{rot} and the sampling spacing $L_{\mathrm{b}}^{\mathrm{rot}}$ for a rotated grid cell in 3D.

The above considerations can be made analogously for a rotated 3D grid (Fig. 4.6). Here, the numbers of degrees of freedom are

$$N_{\mathrm{DoF}}^{\mathrm{3D}} \propto \left(\frac{1}{L}\right)^3, \tag{4.11}$$

$$N_{\mathrm{DoF}}^{\mathrm{3D,rot}} \propto \left(\frac{1}{L^{\mathrm{rot}}}\right)^3. \tag{4.12}$$

The factor in the calculation of the number of sampling points for a bunch changes from $\sqrt{2}$ to $\sqrt{3}$:

$$N_{\mathrm{b}}^{\mathrm{3D}} = \frac{\sigma}{L_{\mathrm{b}}} = \frac{\sigma}{L}, \tag{4.13}$$

$$N_{\mathrm{b}}^{\mathrm{3D,rot}} = \frac{\sigma}{L_{\mathrm{b}}^{\mathrm{rot}}} = \frac{\sigma}{L^{\mathrm{rot}}} \cdot \sqrt{3}. \tag{4.14}$$

If the spatial spacings are assumed to be equal on both grids, the number of degrees of freedom are equal. The number of sampling points on the rotated grid, however, increases by a factor of $\sqrt{3}$.

If the number of sampling points per σ is equal for both types of grids, the number of degrees of freedom for the rotated 3D grid is smaller by $\sqrt{3}^3 \approx 5.2$ compared to the non-rotated grid. A numerical simulation which confirms this ratio will be presented in section 7.1.

4.2 Scattered Field Formulation

In section 2.2 the total field was described as a superposition of the exciting field and the scattered field. In this section, the *scattered field formulation* [33] for the excitation of fields is introduced.

As previously shown, the total field can be separated into two parts due to the linearity of Maxwell's equations in vacuum. The subscripts t, 0 and s denote the total, the exciting and the scattered fields

$$\begin{aligned} \vec{E}_{\mathrm{t}} &= \vec{E}_0 + \vec{E}_{\mathrm{s}}, \qquad (4.15) \\ \vec{H}_{\mathrm{t}} &= \vec{H}_0 + \vec{H}_{\mathrm{s}}. \qquad (4.16) \end{aligned}$$

The exciting fields $\vec{E}_0$ and $\vec{H}_0$ are the fields of a charge distribution traveling at the speed of light in free space. In the scope of this thesis, the charge distribution is an on-axis line charge distribution with a Gaussian shape in the longitudinal direction, i.e. the z-direction. It is characterized by its charge Q and its RMS length σ,

$$\lambda\left(r, \phi, z, t\right) = \frac{Q}{\sigma\sqrt{2\pi}} \exp\left(-\frac{\left(z - c_0 t\right)^2}{2\,\sigma^2}\right) \delta\left(x\right) \delta\left(y\right). \qquad (4.17)$$

The exciting fields of a charged particle bunch in a tube at the speed of light are given in equation (2.12). If the bunch is divided in infinitesimally short disks carrying the charge $\lambda\left(r, \phi, z, t\right) \mathrm{d}z$ at their center, the electric field $\vec{E}_0$ reads:

$$\vec{E}_0\left(r, z, t\right) = \frac{1}{2\pi\epsilon_0} \frac{1}{r} \frac{Q}{\sigma\sqrt{2\pi}} \exp\left(-\frac{\left(z - c_0 t\right)^2}{2\,\sigma^2}\right) \vec{e}_r. \qquad (4.18)$$

The scattered fields in the tube are identically zero and, therefore, do not contribute to the total fields (eqns. (4.15) and (4.16)). The situation is different for a bunch propagating in a longitudinally inhomogeneous accelerator structure. Here, scattered fields are generated at geometrical discontinuities leading to bunch-structure interactions. Furthermore, since $\vec{E}_0$ and $\vec{H}_0$ are known it is sufficient to determine $\vec{E}_{\mathrm{s}}$ and $\vec{H}_{\mathrm{s}}$ for obtaining the total field solution. This approach is referred to as scattered field formulation.

In a full field approach the excitation is introduced directly by the bunch current density into Maxwell's equations. The fields travel from the axis to the surrounding boundary and back, accumulating numerical errors. In the scattered field formulation, the exciting fields are calculated once in a preprocessing step. They are imposed onto the computational domain and excite scattered fields on the walls of the accelerator structure. These travel back to the axis, accumulating less errors compared to the full field approach.

Inserting the superposition of the exciting and scattered fields into the Maxwell-Grid-Equations (eqns. (3.11a)-(3.11d)) leads to a new set of equations. The additive grid current $\widehat{\widehat{\mathbf{j}}}$ is replaced by additive driving terms in two of the four Maxwell-Grid-Equations, introducing the exciting fields into the set of differential equations:

$$\begin{aligned}
\mathbf{C}\,\widehat{\mathbf{e}}^{\mathrm{t}} &= -\frac{\mathrm{d}}{\mathrm{d}t}\left(\mathbf{M}^{-1}_{\mu^{-1}}\,\widehat{\mathbf{h}}^{\mathrm{t}}\right)\\
&\qquad\qquad\qquad\qquad\qquad = \mathbf{M}_{\mu_0^{-1}}\mathbf{C}\,\widehat{\mathbf{e}}^{0}\\
\frac{\mathrm{d}}{\mathrm{d}t}\widehat{\mathbf{h}}^{\mathrm{s}} &= -\mathbf{M}_{\mu^{-1}}\mathbf{C}\left(\widehat{\mathbf{e}}^{\mathrm{s}}+\widehat{\mathbf{e}}^{0}\right)-\cancel{\frac{\mathrm{d}}{\mathrm{d}t}\widehat{\mathbf{h}}^{0}}\\
\frac{\mathrm{d}}{\mathrm{d}t}\widehat{\mathbf{h}}^{\mathrm{s}} &= -\mathbf{M}_{\mu^{-1}}\mathbf{C}\,\widehat{\mathbf{e}}^{\mathrm{s}}-\left(\mathbf{M}_{\mu^{-1}}-\mathbf{M}_{\mu_0^{-1}}\right)\mathbf{C}\,\widehat{\mathbf{e}}^{0},
\end{aligned}\tag{4.19}$$

$$\begin{aligned}
\widetilde{\mathbf{C}}\,\widehat{\mathbf{h}}^{\mathrm{t}} &= \frac{\mathrm{d}}{\mathrm{d}t}\left(\mathbf{M}_{\epsilon}\,\widehat{\mathbf{e}}^{\mathrm{t}}\right)\\
&\qquad\qquad\qquad\qquad\qquad = \mathbf{M}_{\epsilon_0}\,\widehat{\mathbf{e}}^{0}\\
\frac{\mathrm{d}}{\mathrm{d}t}\widehat{\mathbf{e}}^{\mathrm{s}} &= \mathbf{M}_{\epsilon^{-1}}\widetilde{\mathbf{C}}\,\widehat{\mathbf{h}}^{\mathrm{s}}-\frac{\mathrm{d}}{\mathrm{d}t}\widehat{\mathbf{e}}^{0}+\mathbf{M}_{\epsilon^{-1}}\cancel{\widetilde{\mathbf{C}}\,\widehat{\mathbf{h}}^{0}}\\
\frac{\mathrm{d}}{\mathrm{d}t}\widehat{\mathbf{e}}^{\mathrm{s}} &= \mathbf{M}_{\epsilon^{-1}}\widetilde{\mathbf{C}}\,\widehat{\mathbf{h}}^{\mathrm{s}}+\left(\mathbf{M}_{\epsilon^{-1}}\mathbf{M}_{\epsilon_0}-\mathbf{I}\right)\frac{\mathrm{d}}{\mathrm{d}t}\widehat{\mathbf{e}}^{0}.
\end{aligned}\tag{4.20}$$

Thus, a consistent set of equations for the scattered fields is found. Note that in the formulation, both, material matrices in vacuum $\mathbf{M}_{\epsilon_0}$ and $\mathbf{M}_{\mu_0}$ as well as the full material matrices $\mathbf{M}_{\epsilon}$ and $\mathbf{M}_{\mu}$ taking into account the geometry of the structure are used.

The driving terms in equation (4.19) and equation (4.20) depend on the material filling of the particular mesh cells. In the vacuum part of the computational domain, both of the driving terms vanish, since

$$\mathbf{M}_{\mu_0^{-1}}-\mathbf{M}_{\mu_0^{-1}} = 0 \tag{4.21a}$$

$$\mathbf{M}_{\epsilon_0^{-1}}\mathbf{M}_{\epsilon_0}-\mathbf{I} = 0. \tag{4.21b}$$

Thus, in this region Equation (4.19) and equation (4.20) reduce to the usual Maxwell-Grid-Equations in absence of excitation sources. They describe the wake fields propagating in the vacuum region.

The driving terms, however, do not vanish for grid cells with metallic filling, i.e. PEC material, since

$$\mathbf{M}_{\mu^{-1}_{\mathrm{PEC}}}-\mathbf{M}_{\mu_0^{-1}} = -\mathbf{M}_{\mu_0^{-1}} \tag{4.22a}$$

$$\mathbf{M}_{\epsilon^{-1}_{\mathrm{PEC}}}\mathbf{M}_{\epsilon_0}-\mathbf{I} = -\mathbf{I}. \tag{4.22b}$$

Analogously, the driving terms for partially filled cells must be considered. Here, the appropriate matrices $\mathbf{M}_{\mu^{-1}}$ and $\mathbf{M}_{\epsilon^{-1}}$ depending on the geometrical approximation used (sec. 4.4) are employed..

In the implementation, the computational domain Ω is separated into two parts. The vacuum part and the metallic part

$$\Omega = \Omega_{\mathrm{Vacuum}} \cup \Omega_{\mathrm{PEC}}. \tag{4.23}$$

The excitation of scattered fields is incorporated at the interface between PEC and vacuum, i.e. at the boundary of the vacuum part $\partial\Omega_{\mathrm{Vacuum}}$. Here, the tangential total electric field is zero. Thus, it is sufficient to set as a boundary condition the tangential component of the scattered electric field to the negative tangential component of the exciting electric field

$$\vec{E}_{\mathrm{t,tan}} = 0 \quad \Rightarrow \quad \vec{E}_{\mathrm{s,tan}} = -\vec{E}_{0,\mathrm{tan}} \tag{4.24}$$

4.3 Excitation

Below, the exciting field mentioned above is calculated for a given charge distribution, and the exciting grid voltages $\widehat{\mathbf{e}}^0$ are determined. Only the exciting electric grid voltages are required, since the time derivative of the exciting magnetic field is replaced by applying Faraday's law (eqn. (4.20)).

According to equation (3.2), the electric voltages $\widehat{\mathbf{e}}^0$ can be computed from the electric field $\vec{E}_0$ (eqn. (4.18)) along a primary edge L of the grid G

$$\widehat{e}(t) = \int\limits_L \vec{E}_0\,(r,z,t) \cdot \mathrm{d}\vec{s}. \tag{4.25}$$

This procedure fails for all edges in the computational domain Ω containing points with $r = 0$. However, grid consistent exciting voltages can be still obtained by the FIT.

The main idea of the computation of the exciting field is presented for the 2D grid (Fig. 4.7). The electric field of a charged particle in the ultrarelativistic limit corresponds to an electrostatic Coulomb field in the plane transverse to the particle's direction of motion. It is therefore sufficient to determine the electrostatic potential in this plane. The total charge Q_{cell} of the particle inside a primary cell is allocated at a dual on-axis grid node. For the rectangular subdomain Ω_r of Ω with length d along the z-axis which equals the diagonal of the rotated primary grid cell Poisson's equation is solved. The total charge Q_{cell} of one grid cell is set to 1 for now.

The potentials are allocated on the primary grid nodes P_j in Ω_r. In order to solve the boundary value problem, appropriate boundary conditions have to be given. For the potentials located at the upper and lower z end of Ω_r, a periodic boundary is chosen. Thus, the potential in the radial direction is calculated for a constant line charge distribution on the axis. Both potentials at the on-axis nodes P_1 and P_9 are additionally subject to a magnetic boundary condition due to the cylindrical symmetry. To the potential at P_8, a

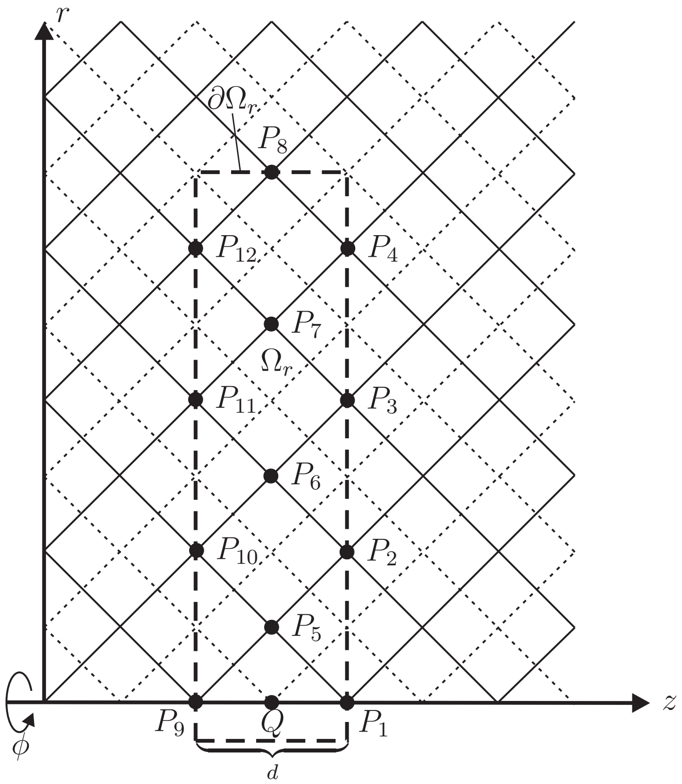

Figure 4.7: The total charge Q and the subdomain Ω_r of the r/z-plane for which the discretized Poisson's equation is solved.

Dirichlet boundary condition is assigned

$$\phi\left(P_8\right) = 0. \tag{4.26}$$

After a solution for the unit charge distribution is found, the potential for the computational domain Ω is calculated by scaling the potentials of the subdomain Ω_r with the total charge of each primary grid cell located on the axis

$$Q_{\text{cell}}(t) = \int\limits_{V_{\text{cell}}} \lambda\left(r, \phi, z, t\right) \mathrm{d}V. \tag{4.27}$$

From the potentials inside Ω, the exciting electric grid voltages are computed, applying the discrete analogy $\widetilde{\mathbf{S}}^T$ of the nabla operator

$$\widehat{\mathbf{e}}^0 = \widetilde{\mathbf{S}}^T \phi. \tag{4.28}$$

Computing the exciting electric grid voltages by solving Poisson's equation on a subdomain of Ω can be adopted analogously to the 3D case. Again, Poisson's equation is set up for a subdomain Ω_s of the computational domain Ω. Its thickness in the longitudinal direction is the length of the diagonal of a rotated grid cell (Fig. 4.4). For the boundary conditions in the longitudinal direction a periodic boundary condition is chosen. At the outward boundary the Dirichlet condition is implemented imposing the analytical expression of the potential for a unit charge

$$\phi_{\partial\Omega_s} = \phi\left(P_j\right) \qquad\qquad P_j \in \partial\Omega_s. \tag{4.29}$$

After solving Poisson's equation, the true potential distribution in Ω_s is obtained by appropriate scaling with the bunch charge distribution and $\widehat{\mathbf{e}}^0$ is computed according to equation (4.28).

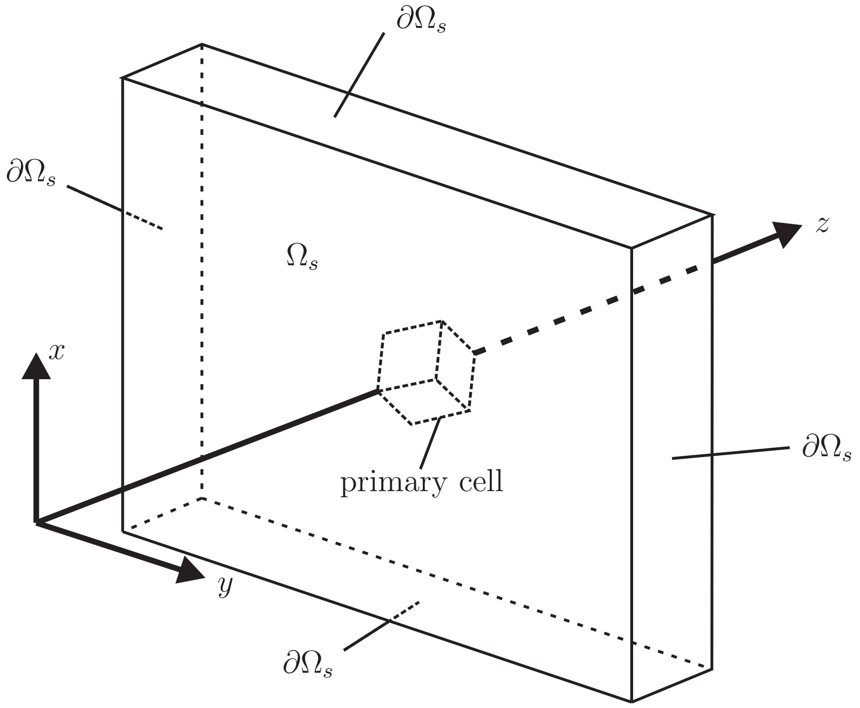

Figure 4.8: The subdomain Ω_s, containing one on-axis primary grid cell, as used for the solution of Poisson's equation in the 3D case.

Note that the spatial distribution of the exciting fields remains constant in every time step except for a longitudinal shift by $c_0\Delta t$. Indeed, in homogeneous structures, exciting fields move unchanged, synchronously with the bunch at the speed of light c_0. Therefore, the time dependence in equation (4.18) and equation (4.27) is neglected in the computation of $\widehat{\mathbf{e}}^0$. However, the shift $c_0\Delta t$ is incorporated in the simulations via the moving window technique. The computational domain Ω is interpreted as a moving window which is shifted in every time step together with the fields by $c_0\Delta t$.

4.3.1 Initial Fields

The leapfrog scheme is a one-step time integration scheme. Therefore, initial scattered electric and magnetic fields separated by half a time step are needed. Without these initial field values the electromagnetic fields of the particle bunch would appear suddenly in the computational domain, which is non-physical. For a bunch starting to travel in a tube sufficiently far away from the wake field generating structure, the initial fields can be determined in a consistent way.

The initial scattered electric field is set up directly from the exciting electric field of the bunch. The total field in the PEC material has to be zero. Whereas in the vacuum, the total field is identical to the field of the bunch. Only the *Partially Filled Cells* (PFC) need to be considered differently (sec. 4.4.2). Applying equation (4.15) leads to

$$\widehat{\mathbf{e}}^{\mathrm{s}}_{m+\frac{1}{2}} = \begin{cases} -\,\widehat{\mathbf{e}}^{0}_{m+\frac{1}{2}} & \text{for PEC} \\ -\bar{f}_{\mathrm{L}} \cdot \widehat{\mathbf{e}}^{0}_{m+\frac{1}{2}} & \text{for PFC} \\ 0 & \text{for Vacuum.} \end{cases} \tag{4.30}$$

The parameter $\bar{f}_{\mathrm{L}}$ quantifies the part of an edge intersecting the interface of PEC and vacuum which is located in the PEC material. Only a fraction of the negative exciting electric voltage is assigned to the scattered grid voltage. This corresponds to the integral in equation (3.2) over the PEC part of the edge L.

The scattered magnetic field voltages are determined using the exciting electric grid voltages. It is important to consider their correct allocation in space and in time as well. A detailed description of the calculation of the initial fields is presented in the appendix A.

4.4 Interface Modeling

The material interface between the PEC material and vacuum is defined by the shape of the considered structures, e.g. cavities. These interfaces have to be incorporated into the mathematical framework of the numerical electromagnetic field computation. The description of the interfaces is provided by an analytical function $r(z)$ in the 2D case and by a triangulated description of the structures' shape in 3D. These mathematical descriptions of the material interfaces allow for the assembling of the matrices $\mathbf{M}_\epsilon$ and $\mathbf{M}_\mu$.

The position of a grid cell is identified with respect to the shape of the given model. If the grid cell does not touch the interface of the PEC material and the vacuum, it is completely assigned to either the PEC or the vacuum part of Ω. The cells intersected by the material interface can be handled by several non-conformal and conformal boundary approximation techniques. In the following, three of these methods for the assembly of $\mathbf{M}_\epsilon$ and $\mathbf{M}_\mu$ are introduced.

4.4.1 Staircase Approximation

The straightforward way to discretize the interface of vacuum and PEC material is the staircase boundary approximation. A primary grid cell which contains PEC material is considered to be in vacuum if the fraction of PEC material is less than 50%. Otherwise, the cell is considered to be completely filled with PEC material. This boundary approximation is inaccurate and, hence, only suitable for high grid resolutions. Nevertheless, its handling is extremely implementation-friendly regarding the computation of the material matrices $\mathbf{M}_\epsilon$ and $\mathbf{M}_\mu$.

Two primary grid cells are now separated by the interface between PEC material and vacuum. Each cell is completely filled with a unique material. Thus, the material interface coincides exactly with one primary grid edge (Fig. 4.9).

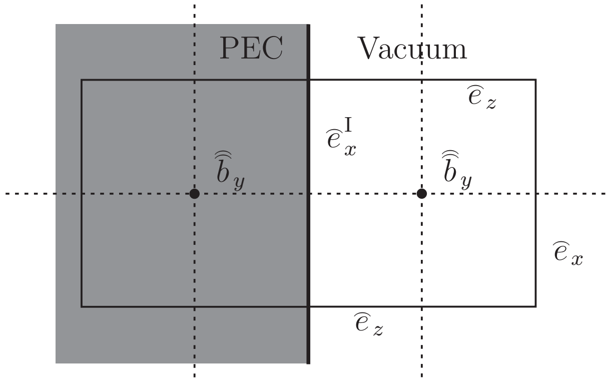

Figure 4.9: Two adjacent primary cells in 2D. One is completely filled with PEC material. The other cell is in vacuum. Due to the boundary conditions, the tangential electric grid voltage $\widehat{e}_x^{\mathrm{I}}$ is always zero.

These material fillings are incorporated by simply setting all entries of $\mathbf{M}_{\epsilon}^{\mathrm{staircase}}$ corresponding to primary grid edges of cells filled with PEC material to zero. There is no need to modify $\mathbf{M}_{\mu}^{\mathrm{staircase}}$. The boundary conditions are automatically fulfilled, i.e. the tangential $\widehat{e}_x^{\mathrm{I}}$ and the normal $\widehat{h}_z$ remain zero in every time step.

4.4.2 Partially Filled Cells

A more accurate boundary approximation is achieved if the staircase approximation is replaced by a conformal discretization technique [34, 35, 36]. One of these conformal techniques is obtained by the Partially Filled Cells (PFC) method. The interface between PEC material and vacuum arbitrarily cuts primary edges and primary faces (Fig. 4.10). At first, the only constraint is that the PEC material exists only in a small part of the cell, i.e. every dual edge stabbing the primary grid cell is located in vacuum. The magnetic induction allocated at the center of such a face can still be associated with a physical field distribution in the vacuum, outside the PEC region.

Only the shortened primary edges and the reduced face area have to be taken into account. This implies a modification of Faraday's law (eqn. (3.4)) for this particular grid cell. In 2D e.g. this reads,

$$-\frac{\mathrm{d}}{\mathrm{d}t}\,\widehat{\widehat{b}}_y^{\mathrm{r}}(n) = \widehat{e}_x + \widehat{e}_z - \widehat{e}_x^{\mathrm{r}} - \widehat{e}_z^{\mathrm{r}}. \tag{4.31}$$

According to equation (3.2) and equation (3.3), the magnetic grid flux is equal to the integral of the magnetic induction $\vec{B}(x, y, z)$ over the reduced area of the face

$$\widehat{\widehat{b}}^{\mathrm{r}} = \int\limits_{f_{\mathrm{A}}\cdot A} \vec{B}(x, y, z)\cdot \mathrm{d}\vec{A}, \tag{4.32}$$

f_{A} being the relative part of the cell area in vacuum. The grid voltages correspond to the

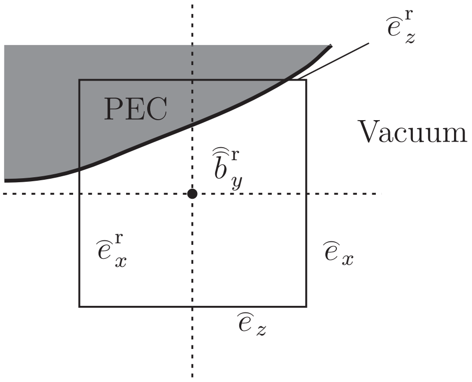

Figure 4.10: A primary cell which is partially filled with PEC material in 2D. The filling is less than 50% and the dual grid edge is allocated in free space. The interface of PEC material and vacuum defines a reduced cell area and shortened cell edges.

integral along the reduced primary edges

$$\widehat{e}^{\mathrm{r}} = \int\limits_{f_{\mathrm{L}} \cdot L} \vec{E}(x, y, z) \cdot \mathrm{d}\vec{s}, \tag{4.33}$$

f_{L} being the fraction of the cell edge in vacuum.

The corresponding matrix entries in $\mathbf{M}_{\mu}^{\mathrm{PFC}}$ and $\mathbf{M}_{\epsilon}^{\mathrm{PFC}}$ are scaled respectively by f_{L} and f_{A} [37]. For example, $\left(\mathbf{M}_{\mu}^{\mathrm{PFC}}\right)_i$ and $\left(\mathbf{M}_{\epsilon}^{\mathrm{PFC}}\right)_j$ read as follows

$$\left(\mathbf{M}_{\mu}^{\mathrm{PFC}}\right)_i = f_{\mathrm{A}} \cdot \left(\mathbf{M}_{\mu_0}\right)_i , \tag{4.34a}$$

$$\left(\mathbf{M}_{\epsilon}^{\mathrm{PFC}}\right)_j = \frac{1}{f_{\mathrm{L}}} \cdot \left(\mathbf{M}_{\epsilon_0}\right)_j . \tag{4.34b}$$

If the PEC filling of the cell is arbitrary, the dual edge stabbing the grid cell face may be located completely inside the PEC region (Fig. 4.11). The interpretation for the corresponding entries of the material matrices is less obvious, because the magnetic grid voltage $\widehat{h}_y$ has to be zero, whereas the curl of the electric grid voltages and hence the magnetic grid flux $\widehat{\widehat{b}}_y$ does not necessarily vanish. However, equations (4.34a-4.34b) can still be applied formally. Numerical simulation tests indicate the validity of this approach [37].

Despite of the better numerical accuracy compared with the staircase approach, there is an important disadvantage of the PFC method as described above. The maximum stable time step of free space defined by the Courant criterion (eqn. (3.40)) is no longer preserved. Reduced cells, i.e. shortened cell edges and diminished cell faces, decrease the maximum allowed time step for the leapfrog scheme [38, 39]. This is a crucial restriction in wake field computations, since the zero dispersion property of the rotated grid in the longitudinal direction does only apply for this particular choice of the time step. In the following subsections, two boundary approximation methods are introduced which allow for a conformal discretization of the interface and simultaneously preserve the maximum stable time step for free space or in the staircase boundary approximation.

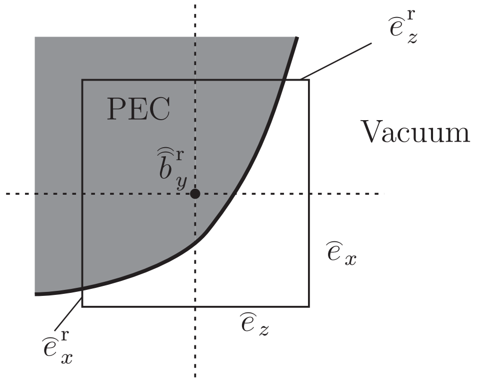

Figure 4.11: A primary cell with more than 50% filling of PEC material. The non-vanishing magnetic grid voltage and the magnetic grid induction, respectively, are allocated inside the PEC material.

Uniformly Stable Conformal Scheme

The basic idea of the *Uniformly Stable Conformal* (USC) algorithm is to virtually dispose of the reduced cells. The electric grid voltages in the PFC approximation are allocated on shortened edges. In order to overcome the resulting time step reduction, in the USC approach, the reduced cell A is virtually extended to A_{mod} (Fig. 4.13). The modifications arising due to the extension of the partially filled boundary cells are incorporated into $\mathbf{M}_{\mu^{-1}}^{\mathrm{PFC}}$. Thus, leading to a modified inverse permeability matrix $\mathbf{M}_{\mu^{-1}}^{\mathrm{USC}}$. The magnetic grid flux $\widehat{\widehat{b}}_y^{\mathrm{r}}$ is computed from the two electric grid voltages and the magnetic grid flows of the neighboring cells. This enlarged stencil stabilizes the time update scheme for the partially filled boundary cell A.

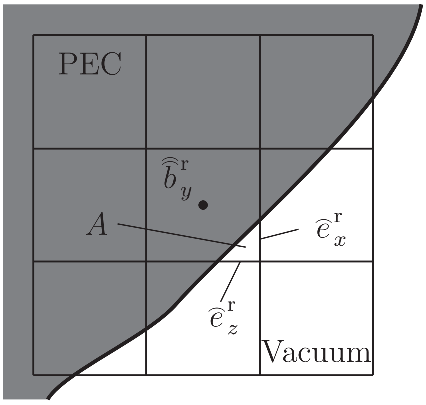

Figure 4.12: The primary cell face A connected to the magnetic grid flux $\widehat{\widehat{b}}_y^{\mathrm{r}}$ is a reduced cell. Only the electric grid voltages $\widehat{e}_x^{\mathrm{r}}$ and $\widehat{e}_z^{\mathrm{r}}$ are relevant.

The maximum stable time step for free space in the domain Ω is equal to the time step for a staircase boundary approximation of an arbitrary structure. Thus, the largest eigenvalue of the system matrix assembled for a staircase boundary approximation

$$\mathbf{A}^{\text{staircase}} = \frac{1}{\mu_0\epsilon_0}\mathbf{M}_{\mu^{-1}}^{\text{staircase}}\mathbf{C}\mathbf{M}_{\epsilon^{-1}}^{\text{staircase}}\widetilde{\mathbf{C}}. \tag{4.35}$$

determines the maximum stable time step.

The modifications of the USC algorithm applied to $\mathbf{M}_{\mu^{-1}}^{\text{PFC}}$ lead to a new system matrix $\mathbf{A}^{\text{USC}}$

$$\mathbf{A}^{\text{USC}} = \frac{1}{\mu_0\epsilon_0}\mathbf{M}_{\mu^{-1}}^{\text{USC}}\mathbf{C}\mathbf{M}_{\epsilon^{-1}}^{\text{PFC}}\widetilde{\mathbf{C}} \tag{4.36}$$

but with the same maximum eigenvalue as $\mathbf{A}^{\text{staircase}}$. Numerical tests show that no reduction of the maximum stable time step occurs.

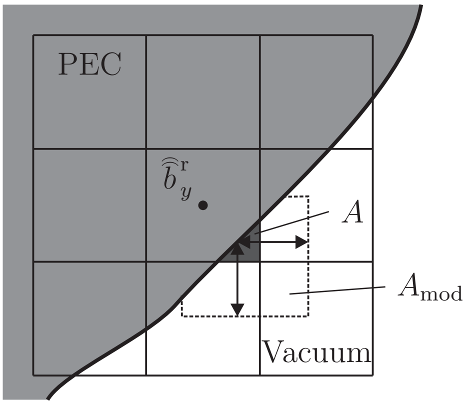

Figure 4.13: The grid cell A from (Fig. 4.12) is extended to a virtual grid cell A_{mod}.

A major disadvantage of the USC scheme is the enlarged stencil. The previously diagonal structure of $\mathbf{M}_{\mu^{-1}}^{\text{PFC}}$ is lost with $\mathbf{M}_{\mu^{-1}}^{\text{USC}}$ containing a maximum of eight additional off-diagonal entries. However, the advantage of the USC scheme is clearly the preservation of the maximum time step for free space. Also, the global second order convergence observed in simulations using the PFC approximation is maintained by the USC scheme.

Simplified Conformal Scheme

A second approach to avoid the time step reduction in conformal boundary approximations can be made if the requirement on second order numerical accuracy is relaxed. This *Simplified Conformal* (SC) scheme aims primarily to the preservation of the maximum allowed time step. For this purpose, the largest eigenvalue of the system matrix

$$\mathbf{A}^{\text{SC}} = \frac{1}{\mu_0\epsilon_0}\mathbf{M}_{\mu^{-1}}^{\text{PFC}}\mathbf{C}\mathbf{M}_{\epsilon^{-1}}^{\text{SC}}\widetilde{\mathbf{C}}. \tag{4.37}$$

has to be equal to the corresponding one in the staircase approximation

$$\rho\left(\mathbf{A}^{\text{SC}}\right) \overset{!}{=} \rho\left(\mathbf{A}^{\text{staircase}}\right). \tag{4.38}$$

In order to obtain $\mathbf{M}^{\mathrm{SC}}_{\epsilon^{-1}}$, the properties of the grid itself are changed. Reduced edge lengths or reduced areas of the grid cells are altered in order to meet the required condition (eqn. (4.38)). However, changing the reduced edge lengths is a less severe distortion of the grid than changing the area of the cell faces. Thus in the SC scheme, each edge length of the grid belonging to a grid cell coinciding with the material interface is adapted by taking into account the four adjacent cell faces such that the condition given in equation (4.38) remains fulfilled.

The resulting modified matrix $\mathbf{M}^{\mathrm{SC}}_{\epsilon^{-1}}$ forms a system matrix whose maximum eigenvalue allows for a leap-frog time integration with the maximum stable time step of free space. Both matrices, $\mathbf{M}^{\mathrm{PFC}}_{\mu^{-1}}$ and $\mathbf{M}^{\mathrm{SC}}_{\epsilon^{-1}}$ remain diagonal. Due to that, they are easy to implement and low in computational cost. However, simulation tests indicate a slightly lower numerical accuracy of the SC approach compared to the USC scheme.

4.5 Numerical Surface Roughness Wake Fields

However, there is a drawback of using rotated grids for the discretization of material interfaces. As an example, a metallic tube is considered. The discretization of this tube on a rotated grid in the 2D case is illustrated in Fig. 4.14. The smooth interface which is oriented parallel to the z-axis is discretized and results in a jagged edge. This effect is most evident for the staircase boundary approximation method. Here, only full PEC or full vacuum cells exist. The material interface described by the material matrices $\mathbf{M}_\epsilon$ and $\mathbf{M}_\mu$ does not render the metallic tube exactly. Anyhow, the rotational symmetry of the discretization error is preserved (Fig. 4.14).

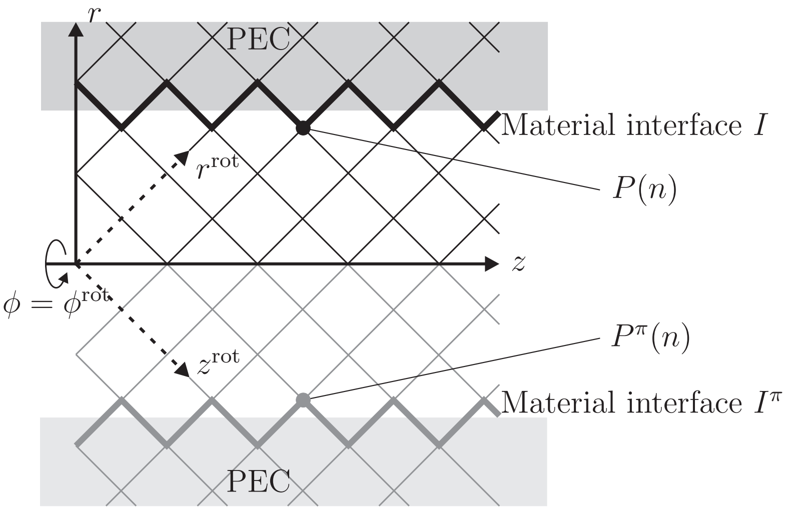

Figure 4.14: A tube is discretized on the rotated grid in 2D. The resulting jagged material interface resembles the tube very inaccurately. Nevertheless, the filling of the n-th primary grid cell referred to by the node $P(n)$ is equal for all angles ϕ. Here, the virtual interface and the virtual node at $\phi = \pi$ are depicted.

Performing a discretization of the tube with the staircase method on a grid in 3D introduces a surface roughness as well. But, in the rotated 3D grid the rotational symmetry of the tube is destroyed. This behavior is depicted in Fig. 4.15. Two grid cells intersecting the material interface are treated differently. The cell allocated at the node $P(n_1)$ is filled completely with PEC material. In contrast to that, the cell referred to by the node $P(n_2)$ is inside the tube for the most part and therefore considered to be completely in vacuum.

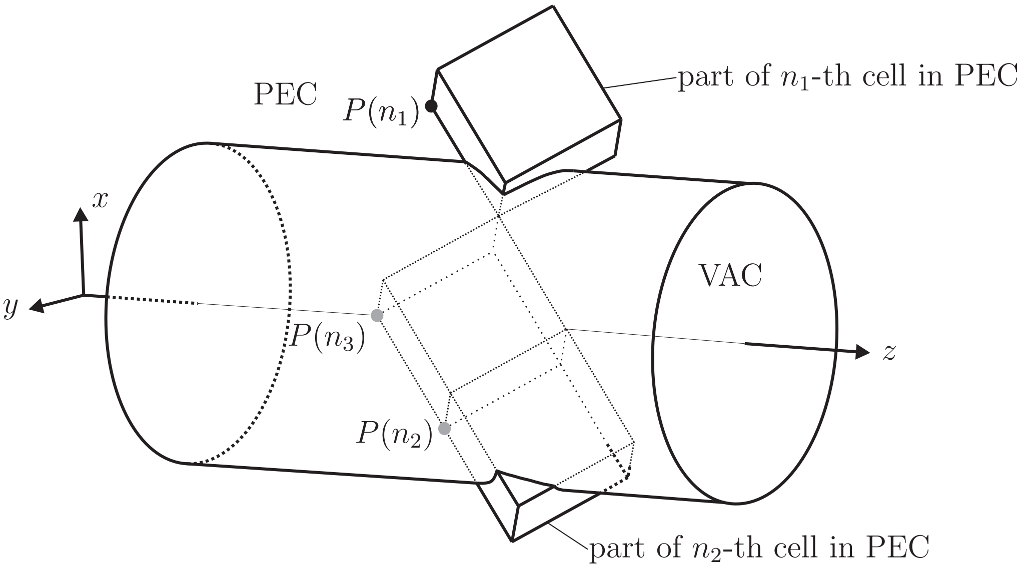

Figure 4.15: A tube is discretized on the rotated grid in 3D. The grid cell referred to by $P(n_1)$ is filled completely with PEC material. The grid cell belonging to $P(n_2)$ is filled completely with vacuum. The rotational symmetry of the tube is broken. For the sake of clarity, the intersection lines of the grid cells and the tube on its backside are omitted.

Due to the different distances of these two cells to the axis, different electric grid voltages are imposed on the cell edges belonging to the cells, which leads to a small scattered field in the tube.

This fields which are excited due to the discretization error in 2D and 3D are comparable to surface roughness wake fields of a real rough surface [40]. Therefore, they are called *numerical surface roughness wake fields.*

Applying a conformal boundary approximation method leads to smoother boundaries. The symmetry is not broken any more. Only numerical surface roughness wake fields are generated due to the discretization on the rotated grid.

ROCOCO and ROCOCO3D

The implementation of the algorithm presented in this chapter in a numerical code for wake field calculations is called *Rotated and Conformal Grid Code* or ROCOCO for the 2D case. Analogously, the implementation is called *Rotated and Conformal Grid Code in 3D* or ROCOCO3D in the 3D case.

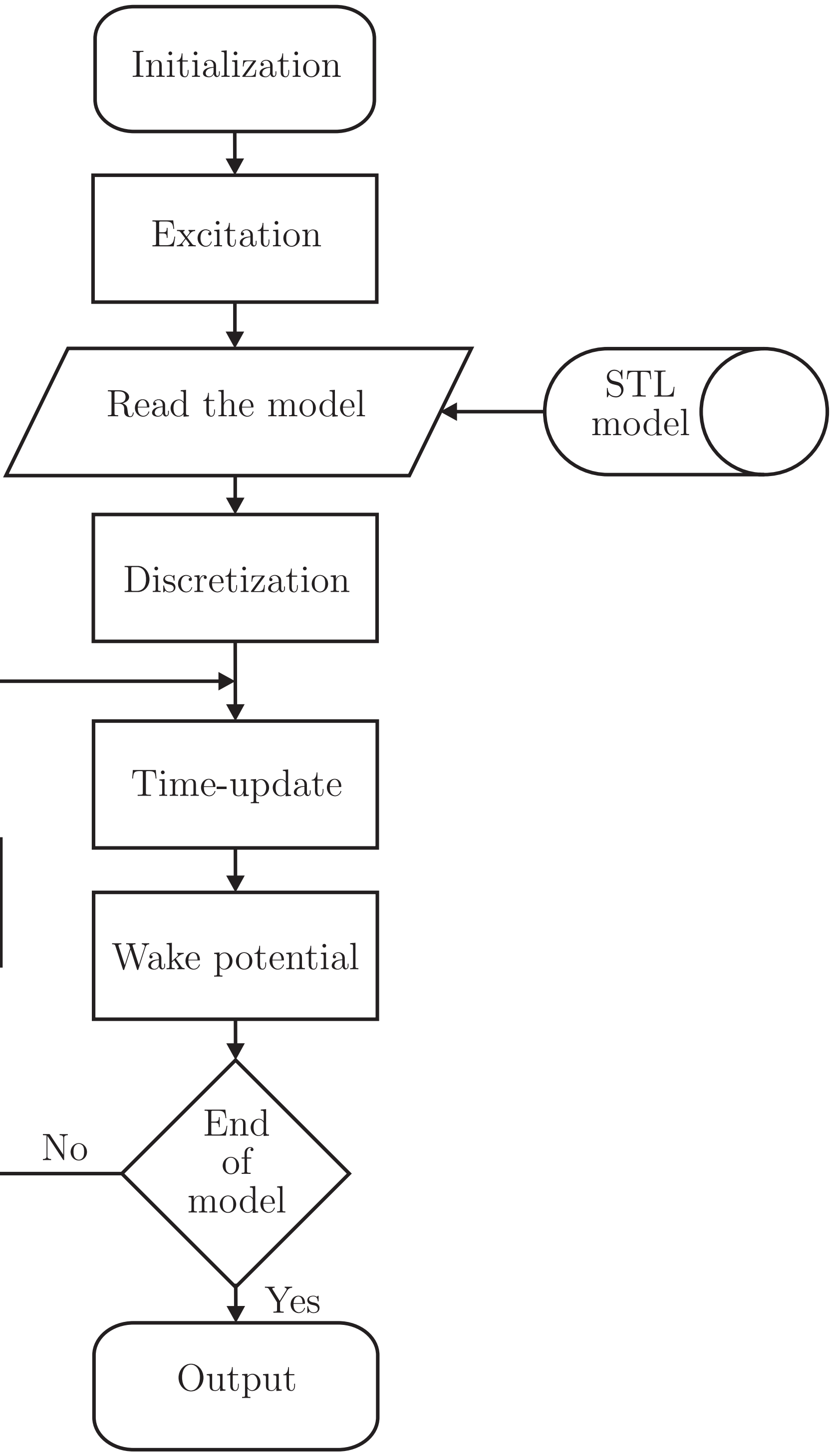

Figure 4.16: Flow chart of the ROCOCO and ROCOCO3D algorithm: After initialization, the exciting fields and the initial fields are calculated. Then, the model is read and discretized. These are the preprocessing steps. In the time-update the wakefields are integrated in every time step in order to obtain the wake potential. Finally, the results are written to files for further processing.

Chapter 5

Results of the 2D Simulations

The algorithm developed in the previous chapter is analyzed. Here, the 2D version of the algorithm is considered. A study of the dispersion properties is followed by the calculation of wake potentials for cylindrically symmetric resonators. Whenever possible, test structures are chosen for which the wake potential can be calculated analytically.

5.1 Dispersion Properties

First of all, the main feature of the algorithm is verified. Its design leads to zero numerical dispersion along the longitudinal direction. This dispersion property is proven in terms of a von Neumann dispersion analysis. However, a plane wave in free space is difficult to implement on an (r, ϕ, z)-grid due to the boundary conditions at the boundaries of the computational domain. Another type of wave with a harmonic time dependency, namely a TEM wave (eqns. (5.1a)-(5.1b)), is chosen instead. Therefore, the structure employed is a coaxial cable oriented along the z-axis. The inner and the outer radii of the coaxial cable are R_i and R_o, respectively. The radius R_i is equal to one half of a rotated grid cell diagonal, just guaranteeing the exclusion of the singularity at $r = 0$ (Fig. 5.1). Both radii are additionally chosen in such a way that the inner and outer conductor cut the grid cells exactly in two halves. Thus, a conformal discretization of the coaxial cable in 2D is possible via triangular cell fillings.

The wave propagating in this cable is a TEM wave

$$\begin{aligned}
\vec{E}^{\mathrm{TEM}}(r, z, t) &= \frac{C}{r} \exp\left(-i\left(k_z\, z - \omega\, t\right)\right) \vec{e}_r, && (5.1\mathrm{a})\\
\vec{H}^{\mathrm{TEM}}(r, z, t) &= \frac{1}{Z_0} \vec{e}_z \times \vec{E}^{\mathrm{TEM}}(r, z, t)\,, && (5.1\mathrm{b})
\end{aligned}$$

with C being a scaling parameter. Its unit is volts. The discrete electric and magnetic grid voltages are computed evaluating the integrals in equations (3.2 and 3.5). Taking

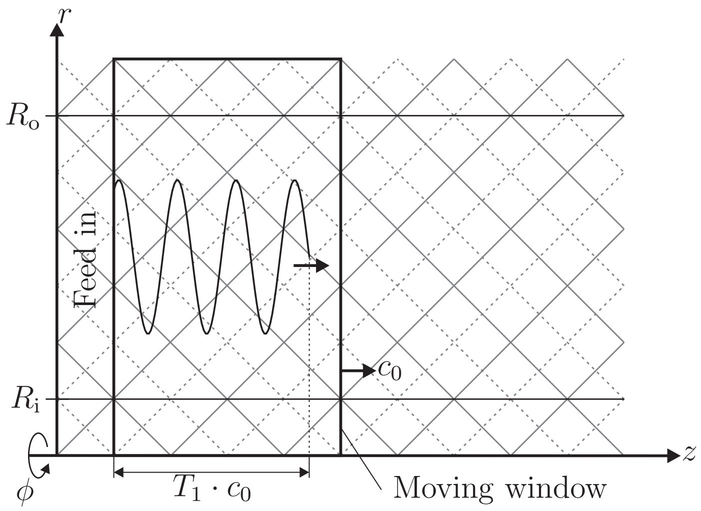

Figure 5.1: The coaxial cable with radii R_i and R_o discretized in the r/z-plane. The TEM wave has already propagated the distance $T_1 \cdot c_0$ into the stationary window.

the cylindrical symmetry into account, the voltages are defined by

$$\widehat{e}^{\,\mathrm{TEM,rot}} = \frac{\Delta r^{\mathrm{rot}}}{\sqrt{2}} \frac{C}{r} \exp\left(-i\left(k_z\, z - \omega\, t\right)\right), \tag{5.2a}$$

$$\widehat{h}^{\,\mathrm{TEM,rot}} = \frac{2\,\pi\, C}{Z_0} \exp\left(-i\left(k_z\, z - \omega\, t\right)\right). \tag{5.2b}$$

The investigation of the dispersion properties involves the moving window technique. The window, which coincides with the computational domain Ω, is at rest. The TEM wave is fed in at its lower z-end. The wave propagates into the computational domain. After a time

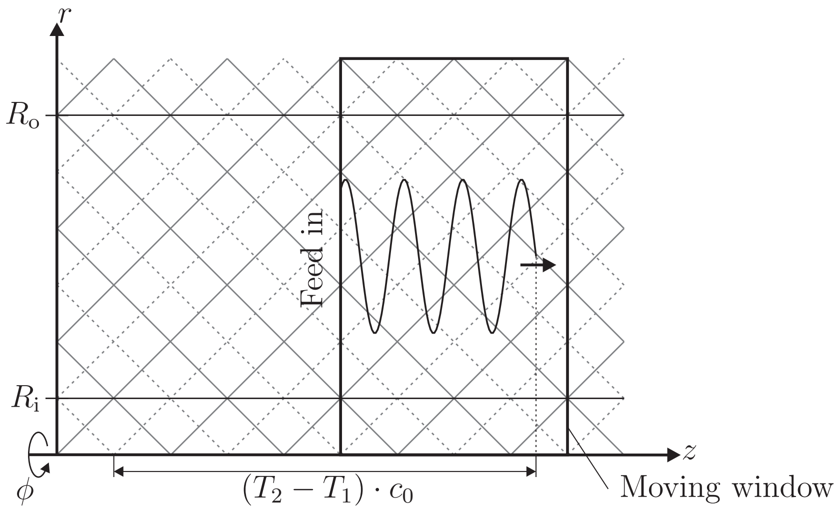

Figure 5.2: The TEM wave and the moving window have both traveled a distance $(T_2 - T_1) \cdot c_0$.

$$T_1 < \frac{\text{Length of window}}{c_0}, \tag{5.3}$$

the moving window is shifted at each time step in the positive z-direction (Fig. 5.1).

The field patterns at the time T_1 and a time $T_2 \gg T_1$ (Fig. 5.2) are compared. If no numerical dispersion errors occur, the two field patterns at T_1 and T_2 should be identical.

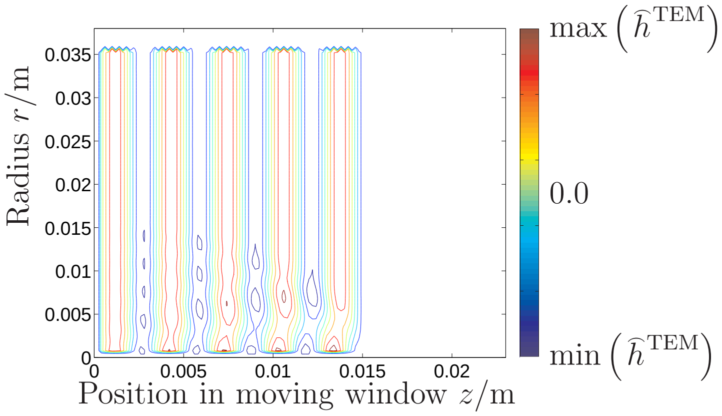

Figure 5.3: The azimuthal magnetic grid voltage $\widehat{h}^{\mathrm{TEM}}$ in the r/z-plane is shown at a time $T > T_1$. Because of the cylindrical symmetry, $\widehat{h}^{\mathrm{TEM}}$ should be radially constant for each z. However, a disturbance is observed, originating from the wave front at the inner conductor.

The dispersion test carried out as described above does not show the expected dispersion-free propagation of the TEM wave. After a few time steps, a small disturbance spreads out from the inner conductor into the computational domain Ω (Fig. 5.3).

This behavior of the numerical solution can be explained by taking a closer look on the matrix entries of $\mathbf{M}_{\mu^{-1}}$ and $\mathbf{M}_{\epsilon^{-1}}$. The entries of these matrices are usually computed in an analytical way which allows for their adjustment to the (r, ϕ, z) coordinate system using the face edges and the edge lengths of the cylindrically symmetric grid. However, these adjustments introduce radius-dependent entries in the material matrices which prevent the dispersion-free propagation of the TEM wave. In order to overcome this systematic error,

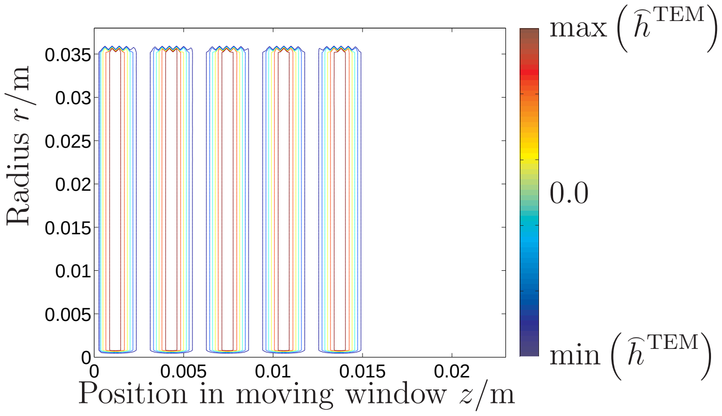

Figure 5.4: The azimuthal magnetic grid voltage $\widehat{h}^{\mathrm{TEM}}$ in the r/z-plane is shown at a time $T > T_1$. Because of the cylindrical symmetry, $\widehat{h}^{\mathrm{TEM}}$ is radially constant for each z.

a correction factor is derived and implemented. A detailed description of the derivation is given in appendix B. For the case of a TEM wave traveling in a coaxial cable, the correction factor is

$$f^{\mu}_{\text{corr}} = 1 - \left(\frac{\Delta r}{2\,r}\right)^2 . \tag{5.4}$$

Only the entries of $\mathbf{M}_{\mu^{-1}}$ have to be modified. The dispersion test which led to Fig. 5.3, now shows the expected field pattern (Fig. 5.4).

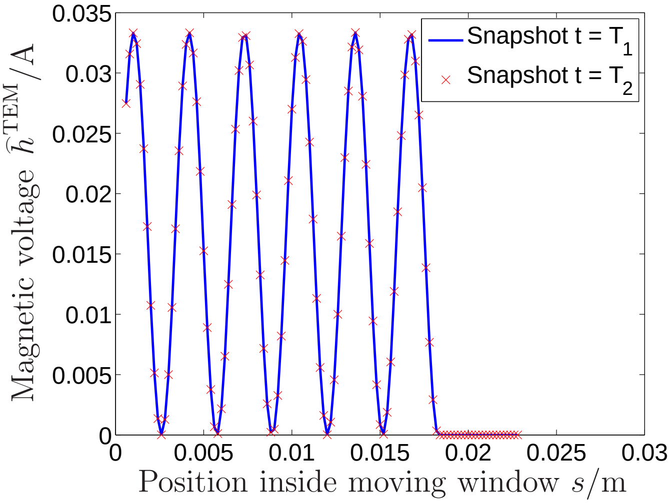

Figure 5.5: The magnetic voltage $\widehat{h}^{\text{TEM}}(r_0, z)$ at two times, T_1 and T_2, along a line parallel to the z-axis and $r_0 \neq 0$.

In order to evaluate the numerical dispersion errors, the two snapshots of the field distributions at T_1 and T_2 are compared (Fig. 5.5). The same result is obtained for different sections of the field patterns along lines parallel to the z-axis at different radii. Plotting

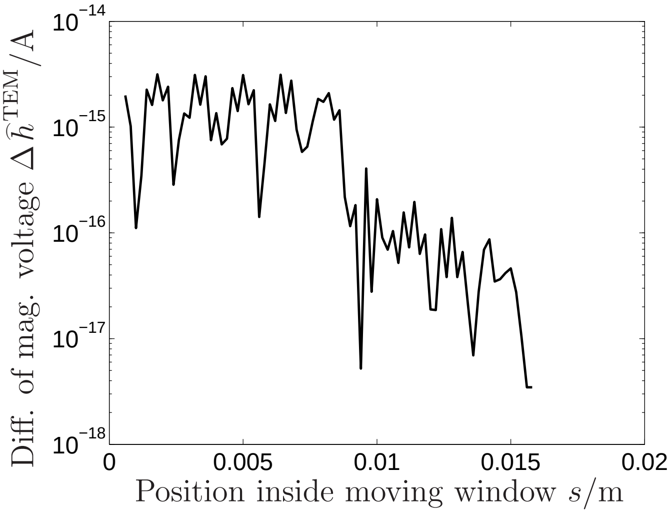

Figure 5.6: A plot of the difference of $\widehat{h}^{\text{TEM}}(T_2)$ and $\widehat{h}^{\text{TEM}}(T_1)$ from Fig. 5.5. The difference of the magnetic voltages $\widehat{h}^{\text{TEM}}(r_0, z, T_2) - \widehat{h}^{\text{TEM}}(r_0, z, T_1)$ is zero up to machine accuracy.

the difference of the magnetic voltages $\widehat{h}^{\mathrm{TEM}}$ of the two snapshots (Fig. 5.6), it becomes apparent that the difference is equal to zero within machine accuracy.

Introducing the correction factor leads to the desired dispersion properties of the algorithm. However, this correction factor is only appropriate for the dispersion-free propagation of a TEM wave (App. B). An arbitrary signal or wave traveling in a coaxial cable is composed of modes. Each of these modes would need an appropriate and therefore individual correction factor due to their different radial dependency. These different radial dependencies of the modes are given by Bessel functions of the first and second kind for coaxial cables. In the case of cylindrical waveguides, the Bessel functions of the second kind are excluded due to their singularity at $r = 0$. As an example, a wave with a radial dependency given by the 1st Bessel function of the second kind traveling in the coaxial cable is illustrated in Fig. 5.7. The correction factor for the TEM wave f^{μ}_{corr} was applied which again generates numerical dispersion errors in the propagation of the wave.

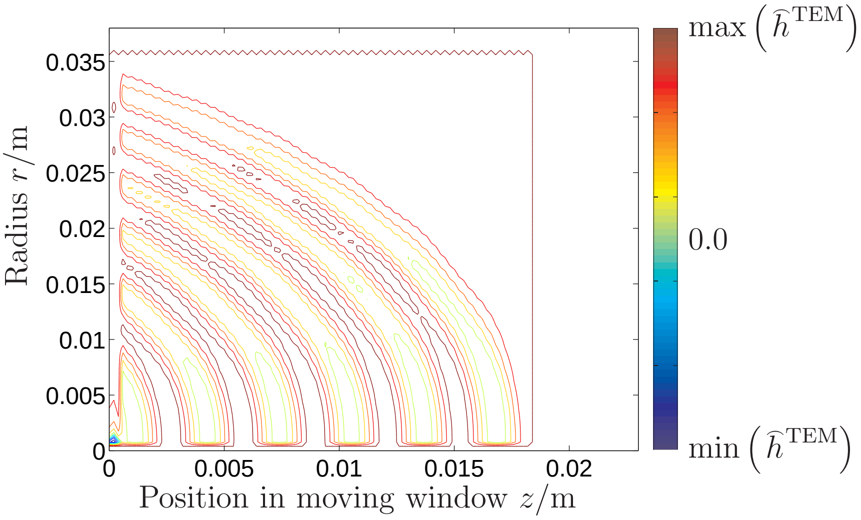

Figure 5.7: A wave with a radial dependency different from the r/z characteristic of the TEM wave travels in the coaxial cable. Applying the correction factor given in equation (5.4) in this case does not lead to a dispersion-free propagation of the wave.

5.2 Verification

After the dispersion properties of the algorithm were investigated, wake potentials of a Gaussian bunch traveling on-axis through a pillbox resonator (Fig. 5.8) and a spherical resonator (Fig. 5.9) are calculated. The results are compared to the analytically known solutions for the wake potentials [41, 42] of the respective resonator. There is one restriction in comparing the numerically obtained wake potentials and the analytical ones which requires special attention. In order to derive the latter, it is assumed that no tubes are attached to the resonators. Calculating the wake potential leads to a superposition of eigenmode solutions in the resonator. In contrast to that, the numerical simulations require in- and outgoing tubes due to the presence of a particle bunch which travels along

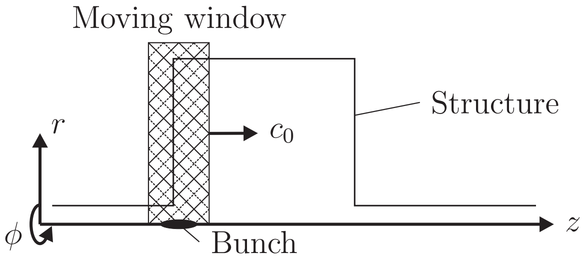

Figure 5.8: The pillbox resonator is discretized in the r/z-plane. The moving window containing the bunch is additionally shown.

the axis. In order to enable a direct comparison with analytical results, these tubes have to be of very small cross-section, so that their impact on the numerical results becomes negligible. A closer investigation with respect to the tube radius will be presented in section 6.2.

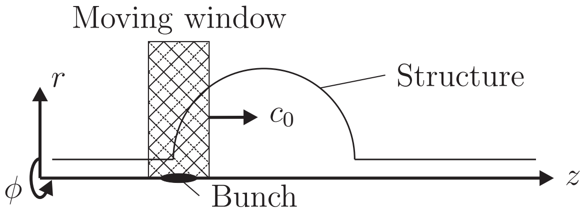

Figure 5.9: The spherical resonator is discretized in the r/z-plane. The moving window containing the bunch is additionally shown.

In Fig. 5.10(a), the wake potentials for a bunch of an RMS length of $\sigma = 2.5$ cm passing the pillbox resonator of radius $r = 5$ cm and length $l = 10$ cm are depicted. The charge distribution of the particle bunch is indicated by a gray Gaussian shaped graph. Starting with a coarse resolution of 20 sampling points per sigma (in the following the number of sampling points per σ in the legends of the figures is denoted by N_b (sec. 4.1.1)), the result approaches the analytical solution denoted by the black graph in Fig. 5.10(a). The wake potential shows a good agreement in the long range wake potential, but rather high resolutions are needed to match the analytical solution in the near range wake potential. As demonstrated below this is primarily due to the staircase method for the boundary approximation.

The remaining two boundary approximation methods mentioned in chapter 4, namely SC and USC, show a very good agreement even for the lowest number of sampling points per σ. They are both conformal schemes and describe the material interface more accurately than the staircase method (Fig. 5.11(a)). The jagged edge resulting from a staircase approximation of the pillbox resonator on the rotated grid (sec. 4.5) is smoothed out.

These smoothed material interfaces allow for more accurate results in the calculation of the wake potential. Still, the tubes necessarily attached to the pillbox resonator spoil the result. Especially in the near range wake field, the sharp corners of the entry into the pillbox are difficult to resolve (Fig. 5.11(a)).

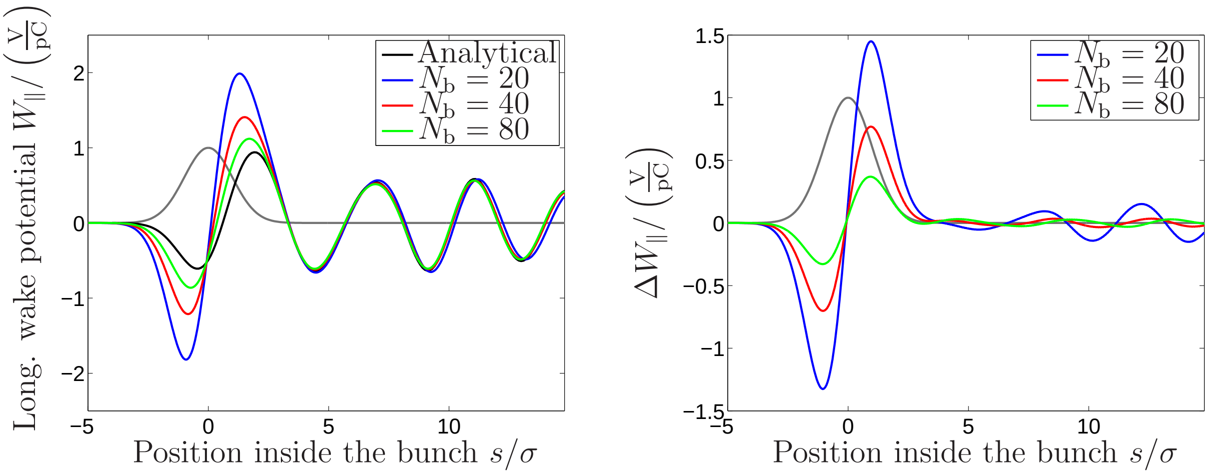

(a) Wake potentials and the analytical reference wake potential.

(b) The difference of the wake potentials to the analytical reference wake potential.

Figure 5.10: Results of ROCOCO and the analytically obtained wake potential for the pillbox resonator (radius = 5 cm, length = 10 cm). The resolutions of the three simulations are 20, 40 and 80 sampling points per σ. The material interface is discretized applying the staircase-type discretization.

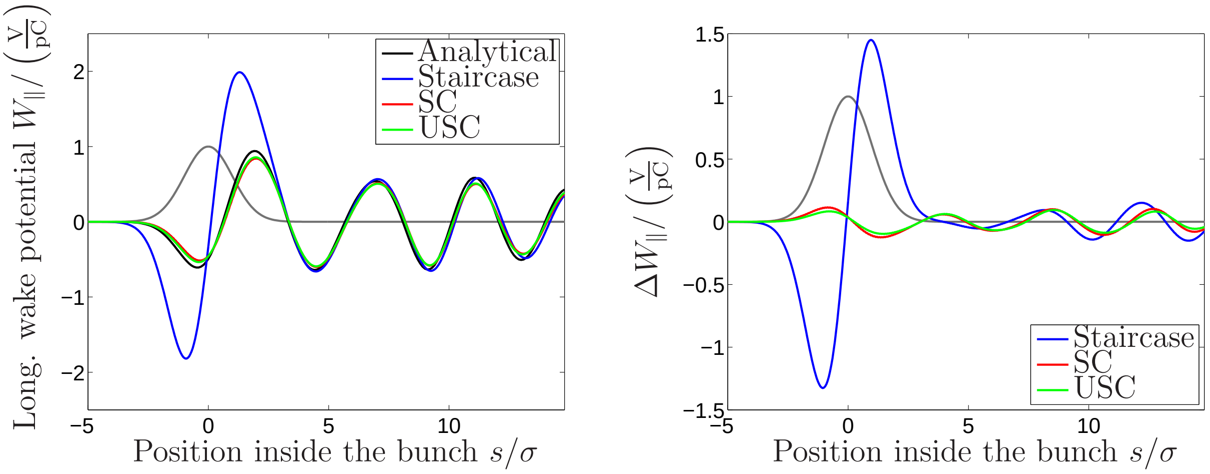

(a) Wake potentials for different boundary approximation methods and the analytical reference wake potential.

(b) The difference of the wake potentials to the analytical reference wake potential.

Figure 5.11: Comparison of the three boundary approximation methods at a resolution of 20 sampling points per σ for the pillbox resonator.

Moreover, the conformal schemes cannot discretize the tubes on the rotated grid correctly (sec. 4.5). The electromagnetic fields which are excited at this inherently non-smooth interfaces are comparable to surface roughness wake fields of a real rough surface. Due to that, at the resolution of 20 sampling points per σ, there are still deviations in the near range wake potential for the conformal boundary approximation schemes. In contrast to that, the long range wake potential matches the analytical reference very accurately. All frequencies excited in the resonator, which are below cut-off of the tubes, are trapped inside the pillbox and contribute to the long range wake potential.

The pillbox resonator consists only of straight lines in the r/z-plane. The spherical resonator has, of course, no such lines except the attached tubes. Therefore, it is particularly appropriate to test the accuracy of conformal boundary approximation techniques. The spherical resonator is cylindrically symmetric. Fig. 5.12(a) illustrates the wake potentials for the spherical resonator. The bunch has an RMS length of $\sigma = 1$ cm and the radius of the sphere is equal to 8 cm. Its material interface is discretized using the staircase method. The coarsest resolution is 20 sampling points per σ, which is increased up to 80 sampling points per σ. Additionally, two higher resolutions of 40 and 80 sampling points per σ are depicted. All three results match the analytical reference in the long range wake potential. A good agreement in the near range wake potential can only be reached with increasing resolution, i.e. a higher number of sampling points per σ.

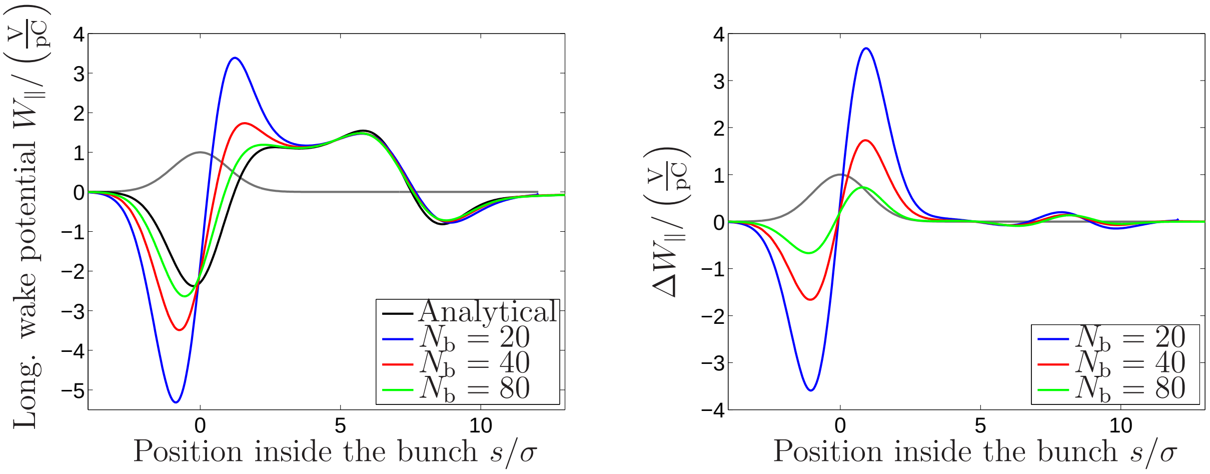

(a) Wake potentials and the analytical reference wake potential.

(b) The difference of the wake potentials to the analytical reference wake potential.

Figure 5.12: Results of ROCOCO and the analytically obtained wake potential for the spherical resonator (radius = 8 cm). The resolutions of the three graphs are 20, 40 and 80 sampling points per σ. The staircase method was used to discretize the material interface.

Again, the two conformal boundary approximation methods are compared to the result obtained by the staircase method at the resolution of 20 sampling points per σ (Fig. 5.13(a)). At this coarsest resolution, the advantage of a conformal boundary approximation becomes apparent. Nevertheless, the SC and the USC scheme still do not exactly match the near range wake potential, due to the same error sources mentioned for the pillbox resonator – the numerical surface roughness wake fields and the tubes.

Increasing the resolution shows an accurate match in the near range wake potential if the USC scheme is applied (Fig. 5.14(a)). Already a resolution of 20 sampling points per σ results in a good agreement between the numerically and analytically obtained solutions.

Further simulations show that very high resolutions are required to resemble the near range wake potential accurately enough. Even the conformal USC scheme does not improve the

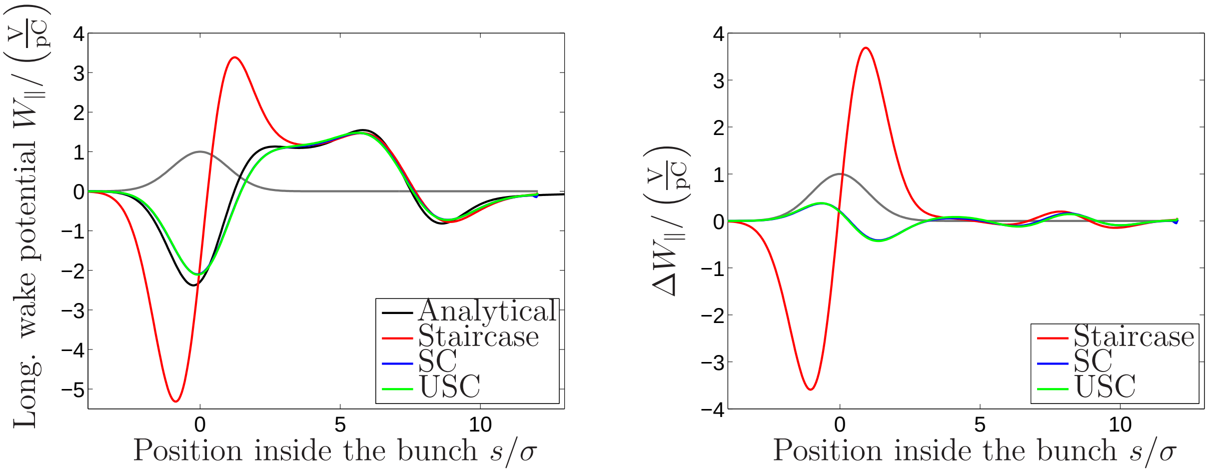

(a) Wake potentials for different boundary approximation methods and the analytical reference wake potential.

(b) The difference of the wake potentials to the analytical reference wake potential.

Figure 5.13: Comparison of the three boundary approximation methods at a resolution of 20 sampling points per σ for the spherical resonator.

situation which is explained with the numerical surface roughness wake fields introduced by the rotated grid. Conformal schemes discretize the material interface more smoothly in contrast to the staircase method. Nevertheless, they do not result in perfectly smooth interfaces. Moreover, the systematic error of the tubes attached to the resonators spoils the result inevitably compared to the analytical resolution.

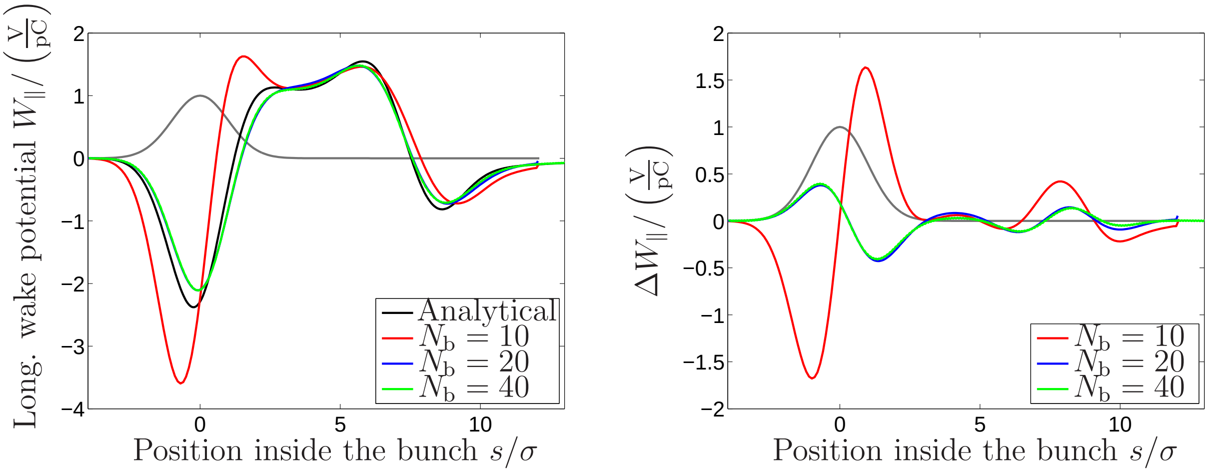

(a) The wake potential at different resolutions employing the USC boundary approximation method. Additionally, the analytical reference wake potential is depicted.

(b) The difference of the wake potentials to the analytical reference wake potential.

Figure 5.14: Comparison of the USC boundary approximation method at three resolutions of 10, 20, and 40 sampling points per $\sigma = 1$ cm for the spherical resonator.

5.3 Comparison of Dispersion Properties

The wake potentials calculated by applying ROCOCO are compared to numerical results obtained with the code ECHO [6], which is also free of numerical dispersion in the direction of the bunch motion.

In Fig. 5.15(a), the wake potentials for the pillbox cavity are compared to the analytical wake potential which is used as a reference. At a resolution of 20 sampling points per $\sigma = 2.5$ cm, the wake potentials of the two codes resemble the reference wake potential equally well. Only the near range wake potential exhibits small deviations.

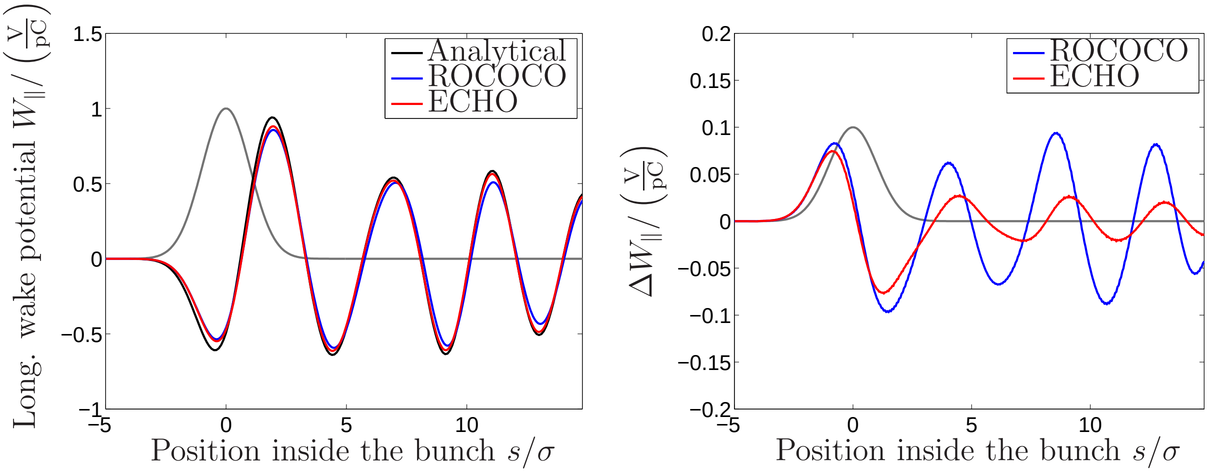

(a) The wake potentials obtained by applying ROCOCO and ECHO and the analytical reference wake potential.

(b) The difference of the wake potentials to the analytical reference wake potential.

Figure 5.15: Comparison of the pillbox resonator wake potentials computed using the 2D simulation tools ROCOCO and ECHO. The RMS length of the bunch is $\sigma = 2.5$ cm. The resolution is 20 sampling points per σ. The USC scheme was applied.

These deviations result from the different types of meshes used. ECHO uses an implicit numerical scheme incorporating a non-rotated Cartesian mesh. All straight material interfaces of the pillbox cavity are either located on or parallel to the grid lines. This allows for an accurate discretization. In particular, the tubes attached to the resonator resemble tubes with a perfectly smooth surface. In ROCOCO, a rotated mesh is implemented. The material interfaces of the pillbox are therefore discretized as jagged edges if the staircase method is applied. The result of Fig. 5.15(a) was obtained using the USC scheme. Therefore, the interface is smoother but not perfectly smooth as for a non-rotated grid, leading to numerical surface roughness wake fields, resulting in the deviations in the near range wake potential.

The same behavior is observed for the spherical resonator. Lacking any straight lines, the spherical resonator is even more difficult to discretize. Especially the conformal SC and USC techniques are of great advantage for the discretization of this type of resonator.

The wake potentials are calculated by ROCOCO and ECHO for a bunch with an RMS

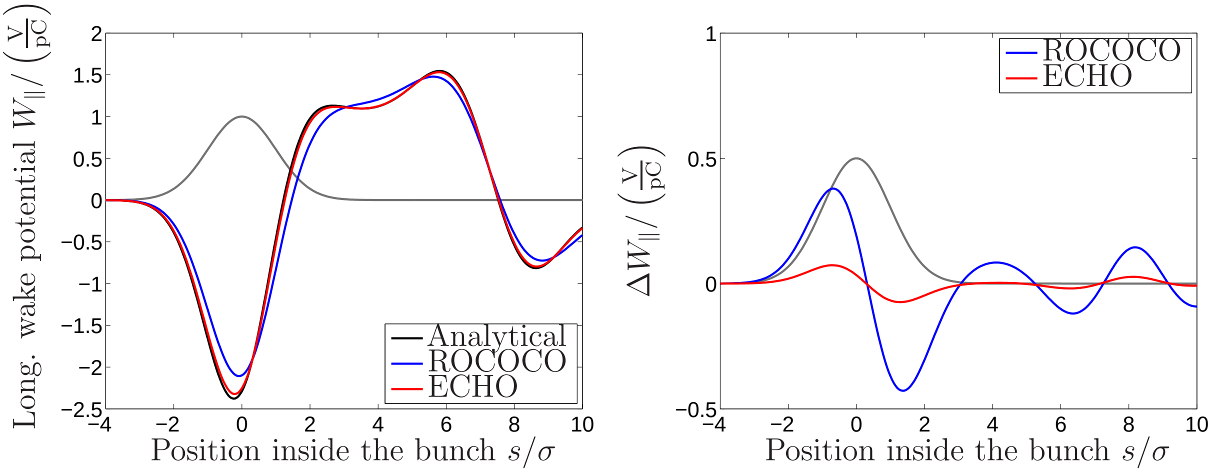

(a) Wake potentials obtained by using ROCOCO and ECHO and the analytical reference wake potential.

(b) The difference of the wake potentials to the analytical reference wake potential.

Figure 5.16: Comparison of the spherical resonator wake potentials computed using the 2D simulation tools ROCOCO and ECHO at a resolution of 20 sampling points per σ and an RMS length of the bunch of $\sigma = 1$ cm.

length of $\sigma = 1$ cm traveling through a spherical resonator. They are shown in Fig. 5.16(a). For both simulations a resolution of 20 sampling points per σ was used. The wake potential calculated using ECHO is very accurate compared to the analytically obtained wake potential. In contrast to that, the wake potential computed applying ROCOCO shows a reasonably good agreement in the long range wake potential. ROCOCO deviates from the reference wake potential in the near range wake potential. The cause for these deviations is the same as mentioned above.

Chapter 6

Results of the 3D Simulations

Analogously to the chapter presenting the results of the 2D version of the algorithm, in this chapter, the results obtained with the 3D version are presented. Cylindrically symmetric resonators are used in order to compare the results of ROCOCO and ROCOCO3D for the wake potentials. Whenever available, analytical expressions for the wake potentials are referred to for verification.

6.1 Dispersion Properties

The dispersion test for the 3D version of the algorithm is carried out incorporating a von Neumann dispersion analysis. In contrast to the cylindrical coordinate system applied in chapter 5, the 3D algorithm makes use of a rotated Cartesian grid. Thus, the computational domain Ω has the shape of a cuboid. Periodic boundary conditions are imposed on the lateral boundaries of Ω, i.e. the faces with $\pm\vec{n}_x$ and $\pm\vec{n}_y$. The plane wave traveling in

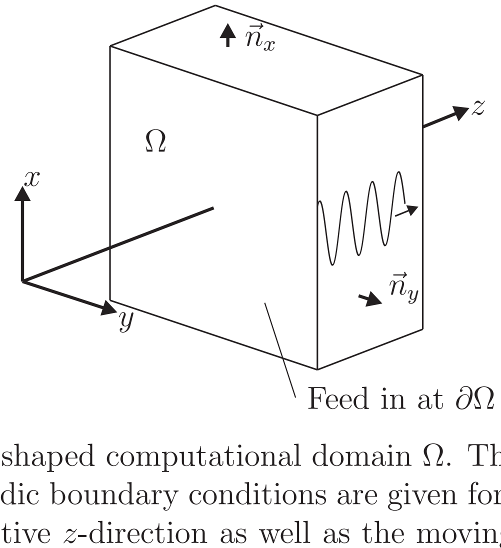

Figure 6.1: The cuboid shaped computational domain Ω. The plane wave is fed in at the lower z-plane $\partial\Omega$. Periodic boundary conditions are given for the lateral boundaries. The wave travels in the positive z-direction as well as the moving window, which is identical with Ω.

the positive z-direction is fed in at the lower z-end of Ω which corresponds to the moving window.

The plane wave is initially fed into the moving window at rest and propagates until a time

$$T_1 < \frac{\text{Length of window}}{c_0}. \tag{6.1}$$

Then, the moving window is shifted at each time step in the positive z-direction by $c_0 \Delta t$. Two snapshots of the field distributions at T_1 and at $T_2 \gg T_1$ are compared to each other. If there are no numerical dispersion errors, the difference of the two field patterns will be zero.

In the test simulation the plane wave solution

$$\begin{aligned} \vec{E}\,(x, y, z, t) &= \widehat{E} \cdot \sin\left(k_z z - \omega t\right) \cdot \vec{e}_{\mathrm{x}} \\ \vec{H}\,(x, y, z, t) &= \widehat{H} \cdot \sin\left(k_z z - \omega t\right) \cdot \vec{e}_{\mathrm{y}} \end{aligned} \tag{6.2}$$

is fed in the moving window and travels a distance equal to $(T_2 - T_1)\, c_0$. The magnetic voltage of the two snapshots taken at T_1 and T_2 along a line parallel to the z-axis is shown in Fig. 6.2.

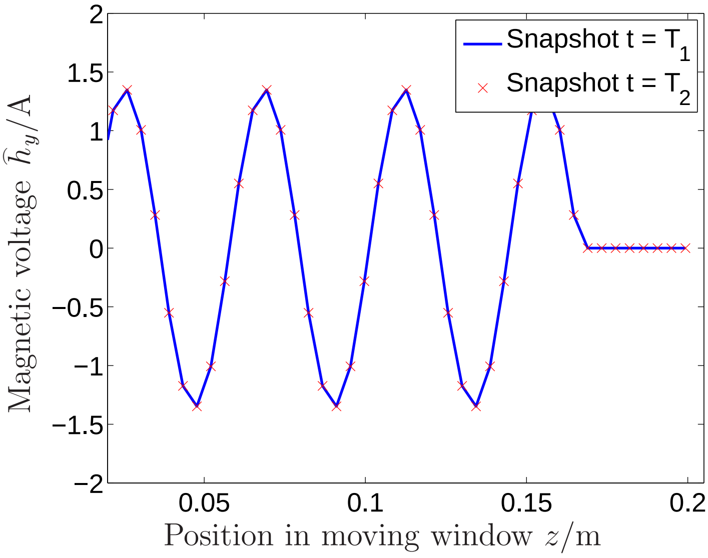

Figure 6.2: The magnetic voltage $\widehat{h}_y\,(x_0, y_0, z)$ at two times, T_1 and T_2, along a line parallel to the z-axis.

The amplitude and the phase of the plane wave of the two snapshots match each other. This proves the zero dispersion property along the z-axis. The difference of the magnetic voltage at the two times, T_1 and T_2, is equal to zero – at least up to machine accuracy (Fig. 6.3). These findings are reconfirmed at different transverse positions (x_i, y_i).

In order to emphasize this result, it is compared to the result of the dispersion test of ROCOCO. Due to the cylindrically symmetric coordinate system, a correction factor had to be introduced into the material matrices to guarantee a dispersion-free propagation of

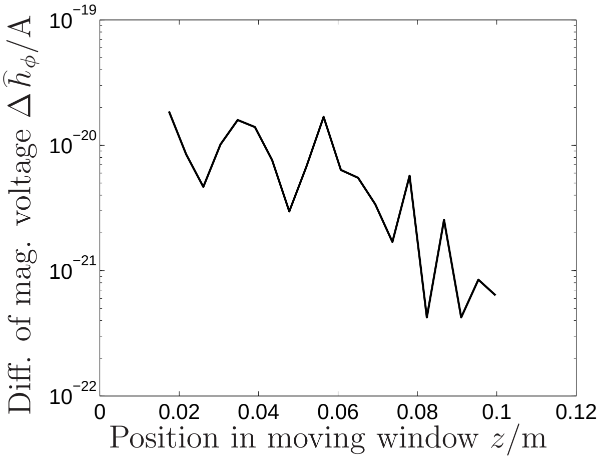

Figure 6.3: A plot of the difference of $\widehat{h}_y(T_2)$ and $\widehat{h}_y(T_1)$ from Fig. 6.2. The difference of the magnetic voltages $\widehat{h}_y\,(r_0, z, T_2) - \widehat{h}_y\,(r_0, z, T_1)$ is zero up to machine accuracy.

waves along the z-axis. Here, in the 3D version, a Cartesian coordinate system is rotated and the dispersion-free property is fulfilled without any correction factor.

Finally, the moving window in 3D along with the resulting magnetic field solution is depicted in Fig. 6.4.

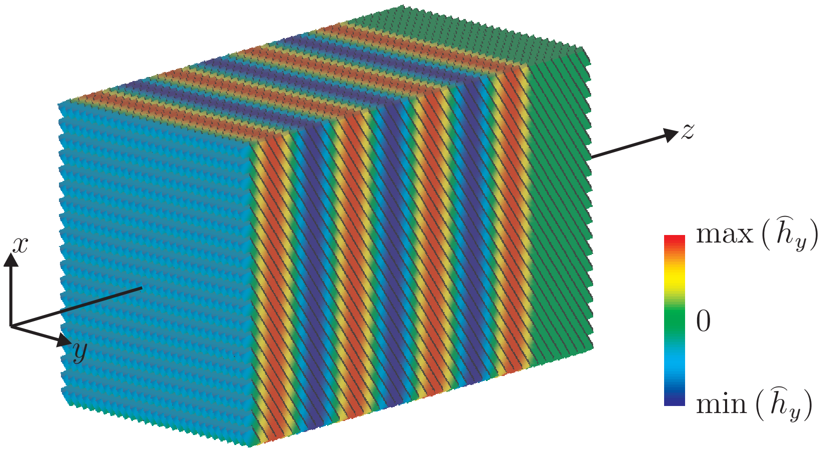

Figure 6.4: The cuboid shaped moving window including the plane wave solution propagating in the z-direction is shown.

6.2 Note on the Impact of the Tubes on the Wake Potential

In the previous chapter, the results of the 2D simulations were presented. Several times the influence of the tubes which allow the particle bunch to travel through a resonator was mentioned. Here, in this section, a study is shown which proves the impact of the tubes on the wake potential. The radii of the tubes in all previous and further investigations in this work is $R_\mathrm{b} = 5$ mm.

In Fig. 6.5(a), the near range wake potential of a bunch with an RMS length of $\sigma = 1$ cm traveling through a resonator is illustrated. The walls of this resonator are perfectly aligned to the grid lines and, therefore, its shape is of no further interest for this study. The computations were carried out applying ROCOCO3D at a resolution of 7 sampling points per σ. The four wake potentials shown in the figure correspond to different tube radii, varying from 10 mm to 1.25 mm.

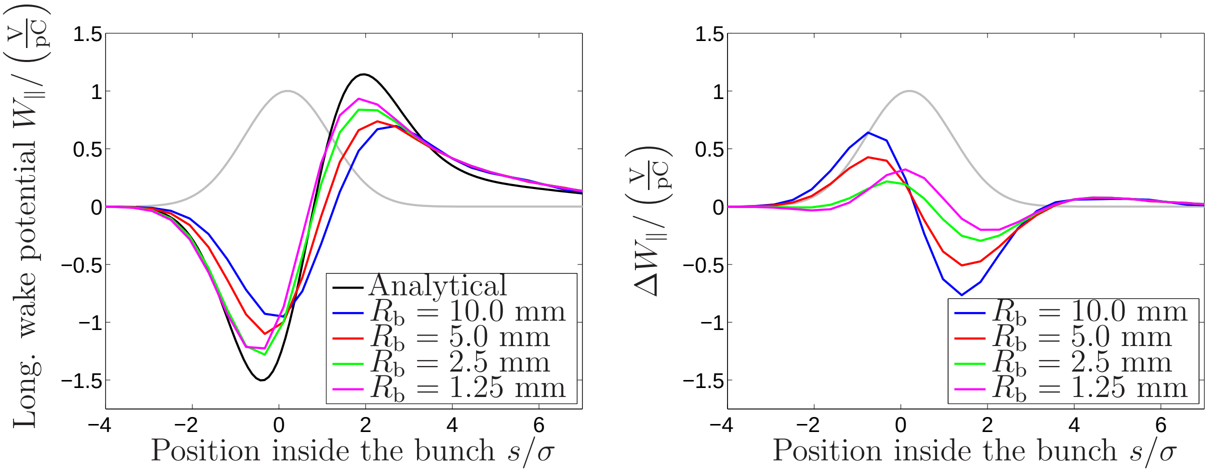

(a) The four wake potentials obtained by using simulations and the analytically obtained one.

(b) The difference of the four wake potentials to the analytical reference wake potential.

Figure 6.5: Study of the wake potential of a bunch traveling through a rotated cubic resonator and tubes with varying radius R_b. The RMS length of the bunch is $\sigma = 1$ cm. The number of sampling points per σ is 7 and the USC scheme was used for the boundary approximation.

The numerically computed wake potentials steadily approach the analytically obtained reference wake potential. In numerical simulations, however, the cross section of the tubes cannot be arbitrarily reduced. This would lead to a huge amount of grid points which are needed for resolving the tube geometry. Thus, a systematic discrepancy between the numerical results and the analytically available reference solutions has to be accepted.

6.3 Verification

The same resonators with additional tubes as in the previous chapter are considered for simulations conducted with ROCOCO3D; the 3D implementation of the algorithm being described in chapter 4. In the following, ROCOCO3D is verified against both analytical references as well as against the 2D results obtained with ROCOCO.

A particle bunch with an RMS length of $\sigma = 2.5$ cm travels through the pillbox resonator. It is discretized with the conformal SC boundary approximation method. Three different resolutions are applied; the coarsest corresponding to 6 sampling points per σ and the finest to 22 sampling points per σ. The overall good agreement of the results with the analytical solution for the wake potential is illustrated in Fig. 6.6(a).

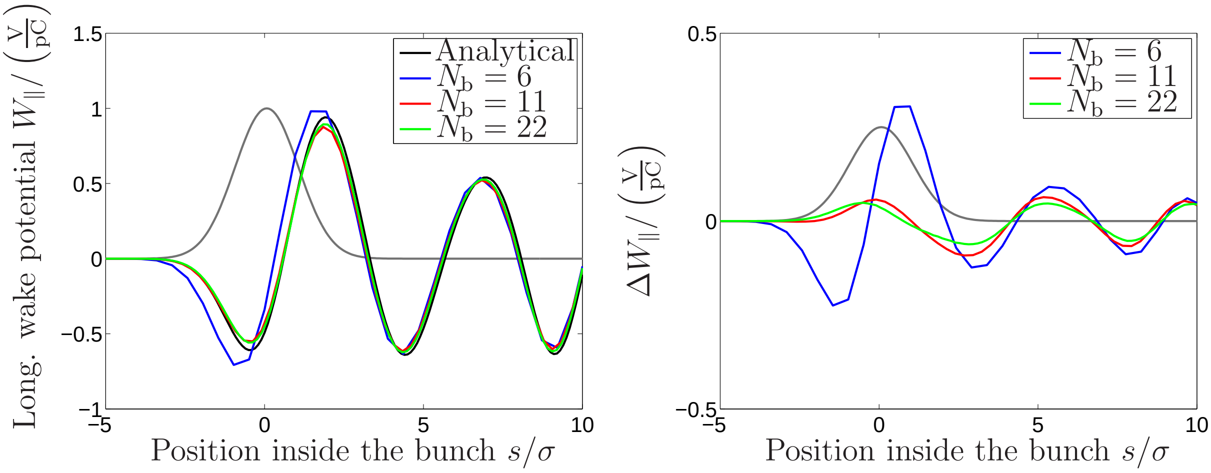

(a) The three wake potentials and the analytical reference wake potential.

(b) The difference of the three wake potentials to the analytical reference wake potential.

Figure 6.6: Results of ROCOCO3D and the analytically obtained wake potential for the pillbox resonator (radius = 5 cm, length = 10 cm). The resolutions in the three cases are 6, 11 and 22 sampling points per σ, respectively. The material interface is discretized applying the SC boundary approximation method.

The long range wake potential is almost identical for each of the three different resolutions. In the near range wake potential, small deviations occur, which however, disappear with increasing resolution.

The wake potentials obtained with two conformal boundary approximation methods at a resolution of 11 sampling points per σ are shown in Fig. 6.7(a). Both conformal methods already approach closely the analytical solution at this resolution. The wake potentials depicted in Fig. 6.6(a) and Fig. 6.7(a) show smaller extrema in the near range wake potential than the reference wake potential obtained by analytical calculation. This is due to the different models used. In the analytical computation, which uses a mode decomposition, only the resonators themselves are taken into account. In the numerical simulations, tubes are required in order to allow the bunch for traveling along the beam axis through the cavity. Due to this difference, the analytically obtained wake potential cannot be met exactly.

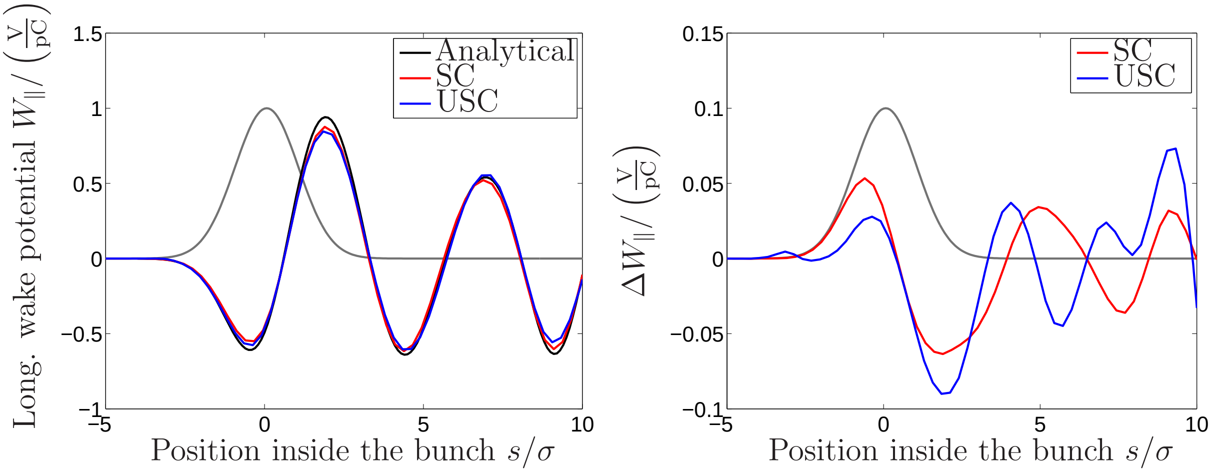

(a) The three wake potentials for two different boundary approximation methods.

(b) The difference of the two wake potentials to the analytical reference wake potential.

Figure 6.7: Comparison of the two boundary approximation methods at a resolution of 11 sampling points per σ.

The pillbox resonator considered above is a cylinder. A more challenging cavity structure in terms of the boundary approximation is the spherical resonator. Its radius is again chosen to $r = 8$ cm. The RMS bunch length is $\sigma = 1$ cm.

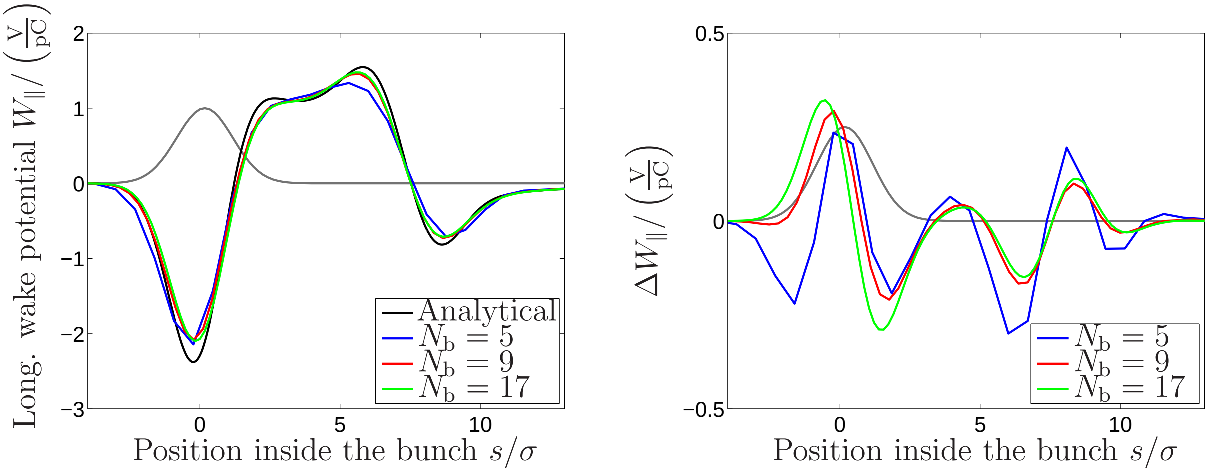

(a) The three wake potentials and the analytical reference wake potential.

(b) The difference of the three wake potentials to the analytical reference wake potential.

Figure 6.8: Results of ROCOCO3D and the analytically obtained wake potential for the spherical resonator (radius = 8 cm). The resolutions of the three graphs are 5, 9 and 17 sampling points per σ. The SC method was applied to discretize the material interface.

In Fig. 6.8(a), the wake potentials at three different resolutions are depicted. Even the coarse resolution of 5 sampling points per σ shows a good agreement with the analytical solution. In order to obtain an accurate result for the near range wake potential, a higher resolution of 9 or 17 sampling points per σ is required. For these higher resolutions, the results for the long range wake potential approach those of the analytical solution. The material interface was discretized applying the SC scheme.

Regarding the staircase discretization, the same limitations as described above apply. This leaves the conformal methods SC and USC for comparison. In Fig. 6.9(a), the wake potentials obtained by using these two boundary approximation methods at a resolution of 9 sampling points per σ are shown.

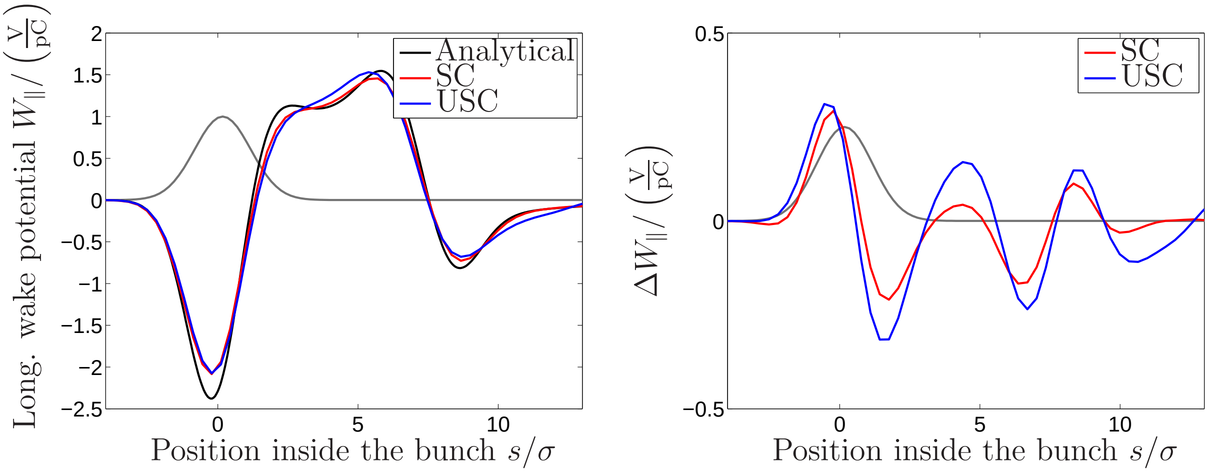

(a) The two wake potentials for two different boundary approximation methods.

(b) The difference of the two wake potentials to the analytical reference wake potential.

Figure 6.9: Comparison of the two conformal boundary approximation methods at a resolution of 9 sampling points per σ.

The two conformal schemes yield a good result in the long range wake potential. Both schemes do not show very accurate results in the near range wake potential due to the numerical surface roughness wake fields. Conformal schemes for the material interface discretization combined with a rotated grid do not produce perfectly smooth interfaces. Therefore, the analytical reference cannot be matched. Wake fields are excited in the tube. Additionally, the difference of the resonators applied in the numerical simulation and in the analytical calculation mentioned above contribute to the spoiled near range wake potential.

6.4 Comparison of Dispersion Properties

ROCOCO3D exhibits zero dispersion along the direction of bunch motion. In this section, the wake potentials for the pillbox and spherical resonator are compared to results for the same resonators obtained by using the 2D implementation of the algorithm. The analytically obtained wake potentials are referred to as the reference solution.

The wake potential obtained by ROCOCO3D in Fig. 6.10(a) shows a very good agreement with the analytical reference. ROCOCO yields a result not as accurate as the 3D result. The deviation in the near range wake potential is due to the boundary approximation of the pillbox in 2D and in 3D on the rotated grid. In terms of this surface

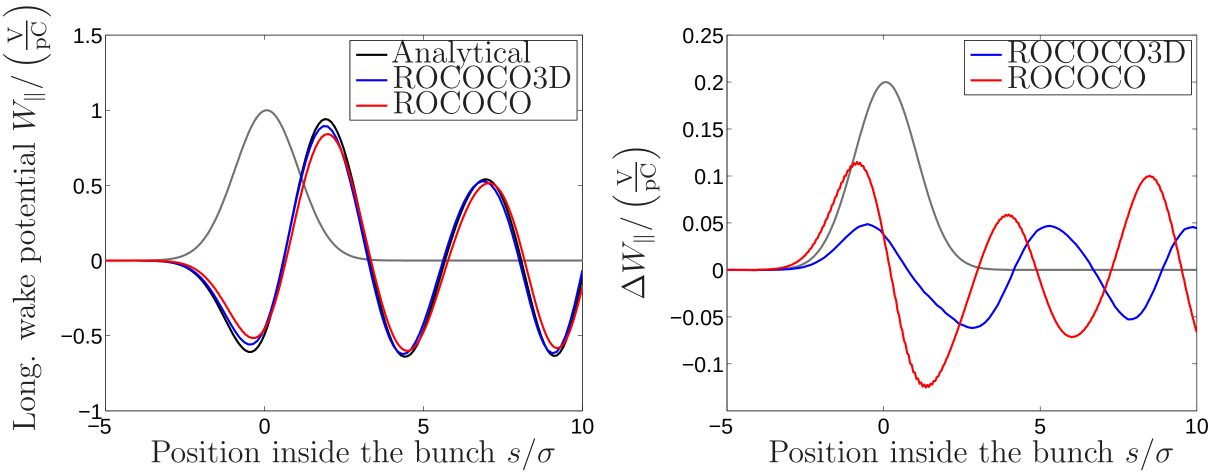

(a) The two wake potentials obtained by applying ROCOCO and ROCOCO3D and the analytical reference wake potential.

(b) The difference of the two wake potentials to the analytical reference wake potential.

Figure 6.10: Comparison of the pillbox resonator wake potentials computed using the two different simulation tools ROCOCO and ROCOCO3D at a resolution of 20 sampling points per σ. The RMS length of the bunch is $\sigma = 2.5$ cm and the material interface is discretized with the SC scheme.

roughness, the resonators are different in ROCOCO and ROCOCO3D: The discretization error introduced in 2D of the material interface is cylindrically symmetric with regard to the beam axis. In 3D, the whole surface is discretized and therefore the discretization error of the boundary is not symmetric.

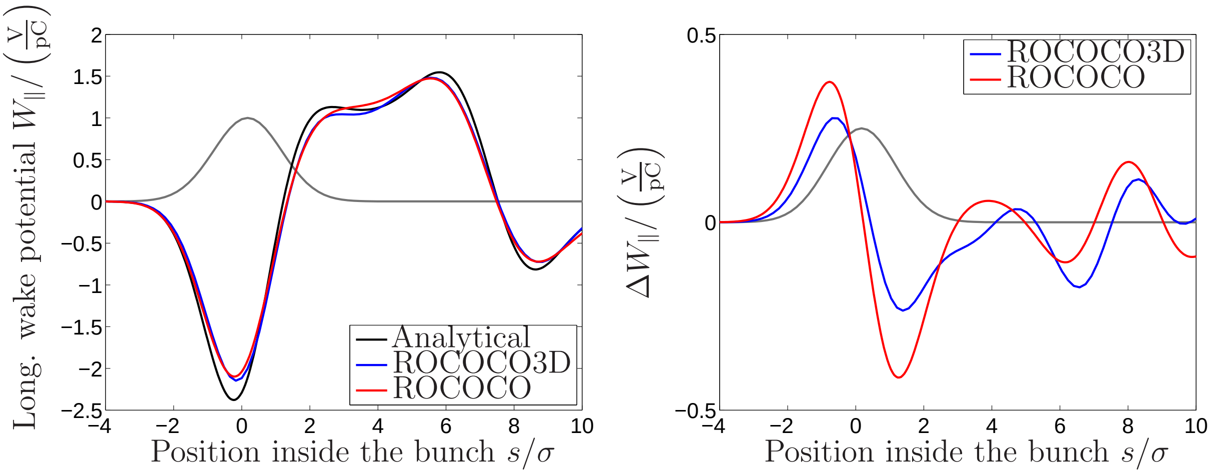

(a) The two wake potentials obtained by using ROCOCO and ROCOCO3D and the analytical reference wake potential.

(b) The difference of the two wake potentials to the analytical reference wake potential.

Figure 6.11: Comparison of the spherical resonator wake potentials computed using the two different simulation tools ROCOCO and ROCOCO3D at a resolution of 20 sampling points per σ. The RMS length of the bunch is $\sigma = 1.0$ cm and the material interface is discretized by the USC scheme.

The same comparison is conducted for the spherical resonator (Fig. 6.11(a)). In both simulations, the USC boundary approximation method was applied.

The resulting wake potentials are almost identical. The differences to the analytical reference in the near range wake potential are due to the same effects as explained above for the pillbox resonator.

6.5 Rotated Cubic Resonator

In order to verify the 3D algorithm for an arbitrary resonator, i.e. without a cylindrical symmetry, a *rotated cubic resonator* is employed. A cube with an edge length of $a = 0.1$ m is rotated by the same angles as the grid (Fig. 4.4). This leads to a resonator with analytically known eigenmodes. The material interface of the rotated cube is perfectly aligned to the faces of the rotated grid cells. Therefore, the discretization of the rotated cubic resonator fits perfectly and the material interface is smooth. Furthermore, an analytical expression for the wake potential of a charged bunch traveling along the diagonal of this cube can be derived (see appendix C).

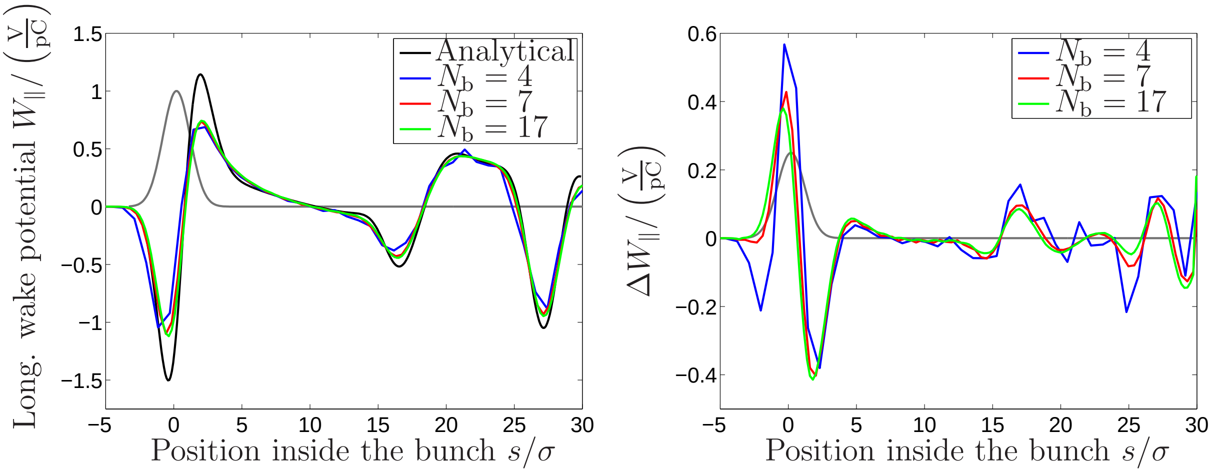

(a) The three wake potentials and the analytical reference wake potential.

(b) The difference of the three wake potentials to the analytical reference wake potential.

Figure 6.12: The wake potential of a rotated cubic resonator for three different resolutions computed with ROCOCO3D. The three resolutions are 4, 7 and 17 sampling points per $\sigma = 1.0$ cm. The boundary approximation method is the SC method.

A particle bunch of an RMS length $\sigma = 1$ cm travels through the rotated cubic resonator. The coarsest resolution is 4 sampling points per σ. This sampling rate of the bunch is already sufficient to resemble the analytical solution of the wake potential. Two more resolutions with 7 and 17 sampling points per σ are applied to resolve the bunch more accurately (Fig. 6.12(a)).

The results for the higher resolutions are very accurate in the long range wake potential. The deviations in the near range wake potential occur due to two effects. On the one hand, the simulated resonator is different from the resonator used in the analytical calculation due to the tubes (sec. 6.2). On the other hand, due to the rotated grid, these tubes cannot be discretized correctly even with a conformal boundary approximation scheme (sec. 4.5). Numerical surface roughness wake fields are generated inside the tubes.

The two conformal schemes applied for the simulations depicted in Fig. 6.13(a) do not show any significant differences. Due to the material interface of the resonator itself, which is aligned with the rotated mesh cells, these already smooth resonator walls are indifferent to the application of the SC or USC scheme. In contrast to that, the near range wake potential is spoiled due to the tubes, which are not described accurately by the boundary approximation schemes.

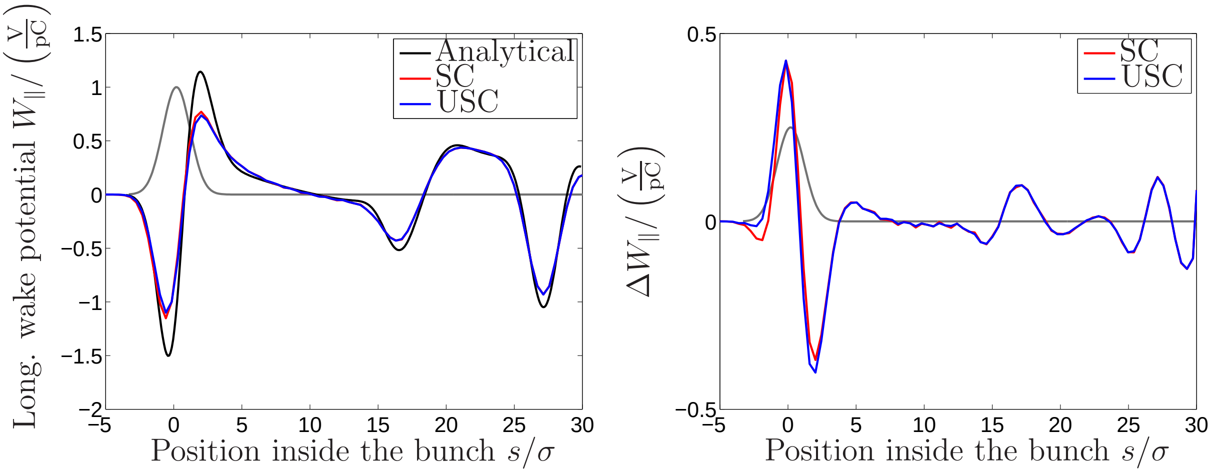

(a) The two wake potentials for two different boundary approximation methods.

(b) The difference of the two wake potentials to the analytical reference wake potential.

Figure 6.13: Comparison of the SC and USC boundary approximation methods at a resolution of 7 sampling points per $\sigma = 1.0$ cm.

Finally, the wake potential for the rotated cubic resonator is compared to the results of two other simulation tools. These two programs are the CST Particle Studio and the directionally dispersion-free PBCI. The resolution is 7 sampling points per σ.

Both directionally dispersion-free codes, i.e. ROCOCO3D and PBCI, show a very good agreement compared to each other (Fig. 6.14(a)). The CST Particle Studio result agrees with the two other results. Due to the relatively large RMS bunch length low numerical dispersion errors occur and the wake potential is calculated accurately. The comparison of the PBCI and ROCOCO3D results to the analytical reference wake potential exhibits the same deviations in the near range wake potential as in the preceding Fig. 6.12(a) and Fig. 6.13(a). This is an indication that the discrepancy to the analytical reference wake potential seen here and before is primarily due to the tubes which are not part of the analytical solution.

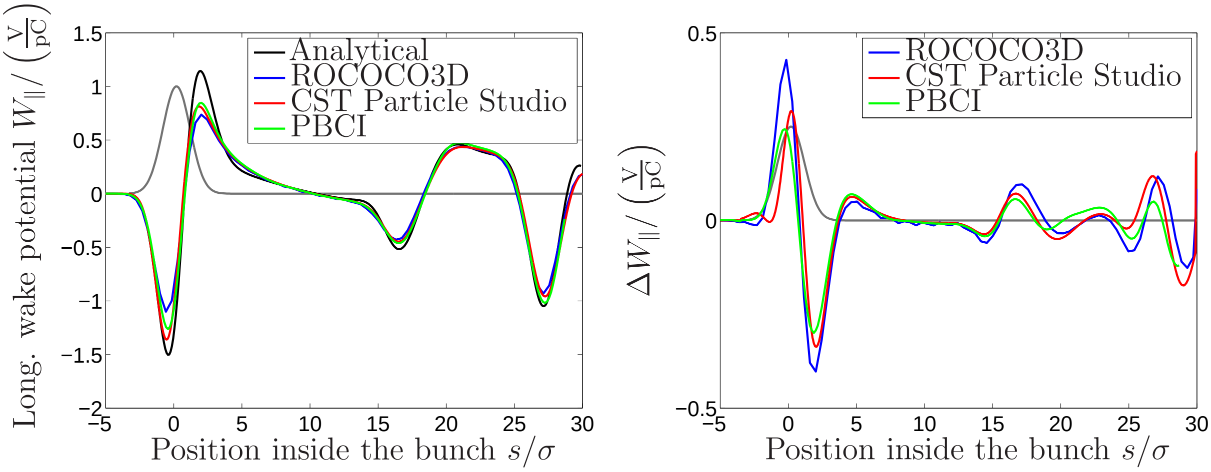

(a) The three wake potentials obtained by using PBCI, ROCOCO3D, and CST Particle Studio and the analytical reference wake potential.

(b) The difference of the three wake potentials to the analytical reference wake potential.

Figure 6.14: Comparison of the wake potentials of the rotated cubic resonator computed using the three different simulation tools PBCI, ROCOCO3D, and CST Particle Studio at a resolution of 7 sampling points per σ and an RMS length of the bunch of $\sigma = 1.0$ cm.

Chapter 7

Applications

In this chapter, two components deployed in particle accelerators are investigated. Collimators are incorporated in the beamline of particle accelerators shortly before the interaction point where experiments are conducted. They are introduced in order to cut off the outer parts of the particle bunch. Thus, a bunch with almost parallel particle trajectories is obtained which decreases noise in the measurements.

As a second example, a long accelerator structure, a TESLA nine-cell cavity, is considered. The term "long structure" refers to a resonator with a length which is very large in comparison to the bunch length σ. Their simulation requires a large number of time steps. Thus, substantial numerical dispersion errors may be accumulated. In this example, the ratio of the structure's dimensions and the RMS bunch length is larger than 1100. This results in a very demanding 3D simulation in terms of both, memory size and computational time.

7.1 Collimator

Cutting off the outer parts of a particle bunch is intended, however, collimators may also have an additional negative effect on the beam. They may induce short range wake fields and therefore degrade the quality of the beam.

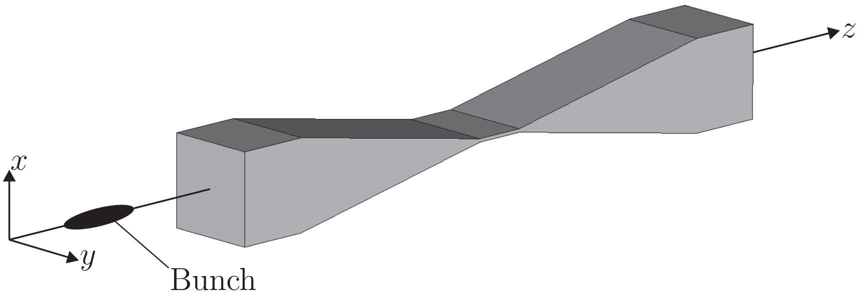

Figure 7.1: The CAD model of the collimator of the International Linear Collider (ILC) [1] collimator test program. Its length is roughly 0.211 m. The electron bunch travels along the z-axis at the speed of light.

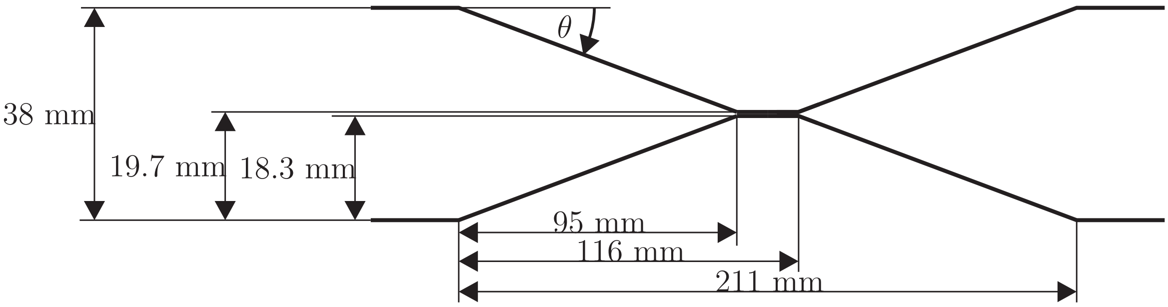

Figure 7.2: Sectional view along the x/z-plane of the collimator shown in Fig. 7.1. The horizontal gap has a height of 1.4 mm. The length of each chamfered section is 95 mm. The length of the gap is 21 mm. This results in an angle of about 10.9° measured relatively to the beam axis. The square cross section has an edge length of 38 mm.

In this section, a collimator (Fig. 7.1) of the ILC collimator test program described in [43], is considered in order to compare the results of two numerical simulation tools. A bunch with an RMS length of $\sigma = 5$ mm travels along the structure axis, passes the gap and excites wake fields.

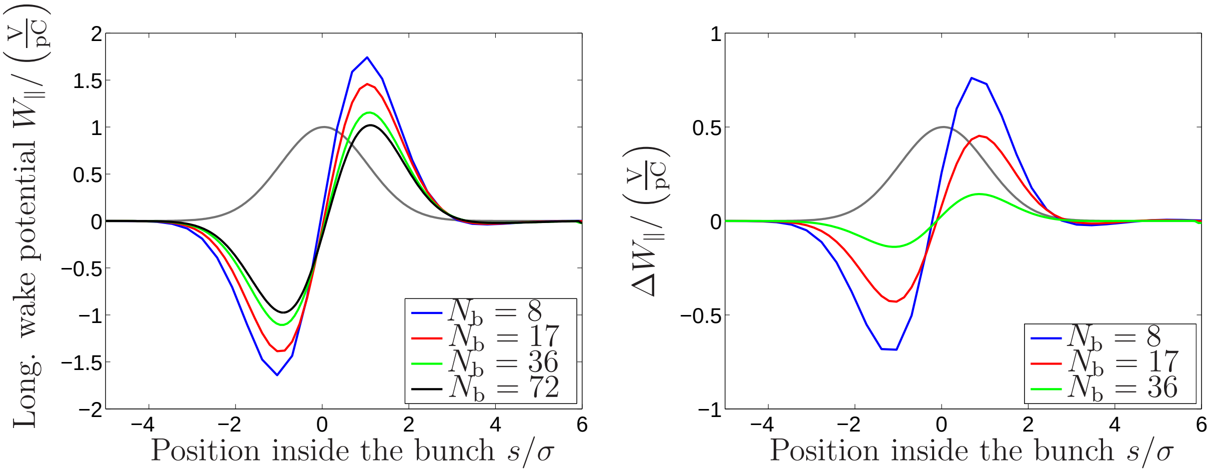

(a) The longitudinal wake potential at four different resolutions.

(b) The difference of the wake potentials to the one at 72 sampling points per σ.

Figure 7.3: The longitudinal wake potential of the collimator (Fig. 7.1) for a bunch with an RMS length $\sigma = 5$ mm. The four resolutions are 8, 17, 36, and 72 sampling points per σ. The results were obtained by ROCOCO3D with the SC boundary approximation method.

In Fig. 7.3(a), four wake potentials are depicted. They are obtained by ROCOCO3D with the SC boundary approximation method. The RMS length of the bunch is resolved by 8, 17, 36, and 72 sampling points per σ. The near range wake potential improves with increasing resolution. The difference of the wake potentials in comparison to the result at the highest resolution diminishes.

Due to the lack of an analytical solution, a number of reference simulations are conducted using the PBCI code.

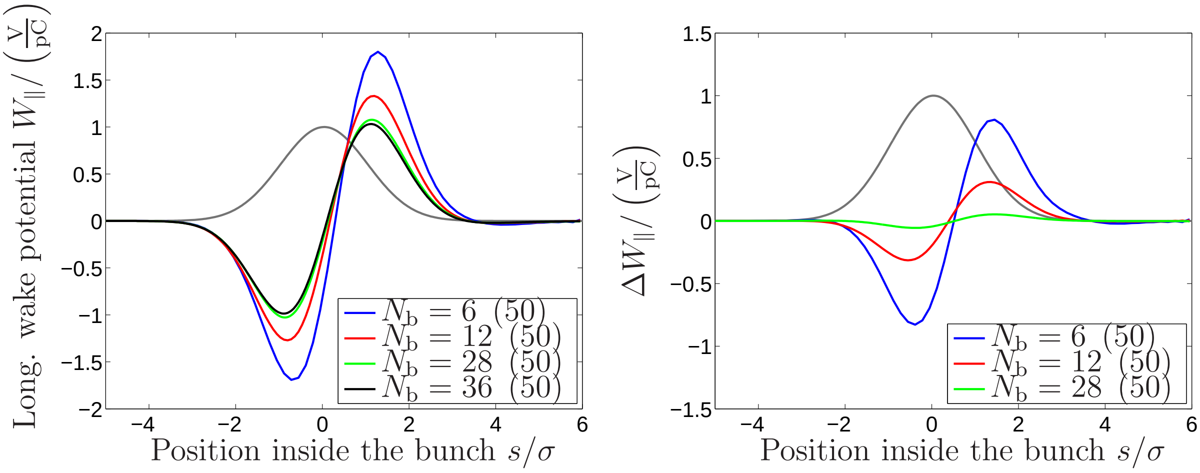

(a) The longitudinal wake potential at four different resolutions.

(b) The difference of the wake potentials to the one at 36 sampling points per σ.

Figure 7.4: The longitudinal wake potential of the collimator (Fig. 7.1) for a bunch with an RMS length $\sigma = 5$ mm. The four resolutions are 6, 12, 28, and 36 sampling points per σ. Additionally, the calculations were done using 50 modes for the mode expansion. The results were obtained by PBCI.

In Fig. 7.4(a) four wake potentials for different grid resolutions in PBCI are shown. The sampling rates used are 6, 12, 28, and 36 sampling points per σ, respectively.

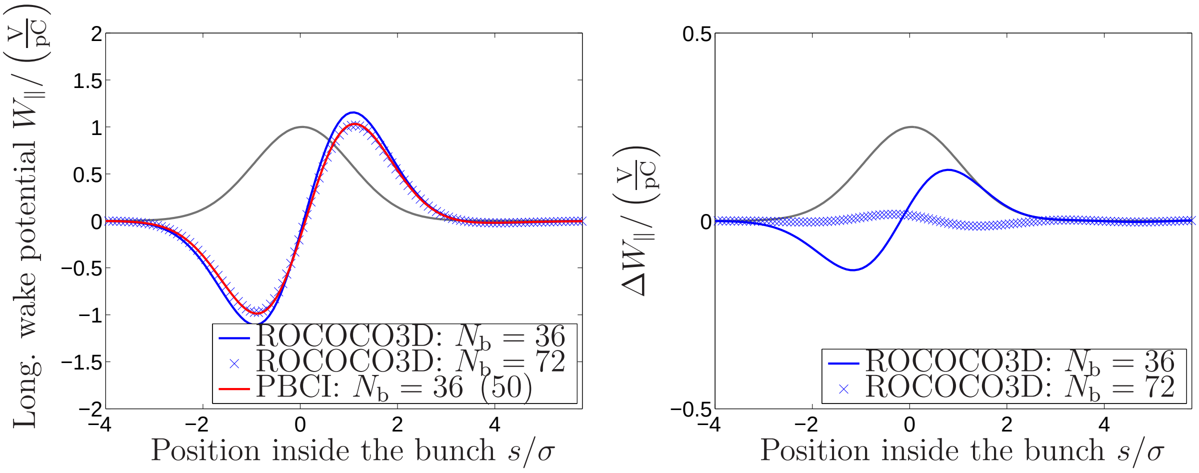

(a) The three wake potentials calculated with PBCI, ROCOCO, and ROCOCO3D.

(b) The difference of the wake potentials obtained by using ROCOCO and ROCOCO3D to the one obtained by PBCI.

Figure 7.5: Comparison of two longitudinal wake potentials for a bunch with an RMS length $\sigma = 5$ mm. The resolution for the results obtained by ROCOCO3D and PBCI is 36 sampling points per σ. For the mode expansion in PBCI 50 modes were used. Additionally, the wake potential obtained by ROCOCO3D using an resolution of 72 sampling points per σ is shown.

The number of modes for the mode expansion in the indirect integration [23] in PBCI is determined by simulations in which the spatial resolution is kept constant and the number of modes is varied. The number of modes which is found to be sufficient for the given problem is indicated in brackets. Here it is 50 modes.

The wake potentials depicted approach the result obtained at the highest resolution of 36 sampling points per σ. This is illustrated in the difference plot (Fig. 7.4(b)).

However, the simulation accuracy is dominated by the collimator's geometry and not by the bunch length. The RMS bunch length of 5 mm is large compared to the 1.4 mm gap of the collimator. A large number of sampling points is required to resolve the gap. Therefore, the bunch length is in all cases resolved very accurately.

In Fig. 7.5(a) the results of both codes, ROCOCO3D and PBCI, are now compared to each other at a resolution of 36 sampling points per σ. There are deviations in the near range wake potential. This is explained with the resolution problems of the gap mentioned above. Additionally, due to the rotated grid, the gap is resolved inaccurately at 36 sampling points per σ in ROCOCO3D. In contrast to that, in PBCI a Cartesian grid is employed and the gap is discretized more accurately. The wake potentials for the highest resolution given in Fig. 7.3(a) and Fig. 7.4(a) exhibit a good agreement. For comparison, this result at 72 sampling points per σ is also depicted in Fig. 7.5(a).

In the following, the parameter

$$\alpha = \frac{\theta \cdot b}{\sigma}, \tag{7.1}$$

will be used to compare the electron bunch length to the dimensions of the collimator [44]. The angle θ is the tapering of the collimator and b denotes half the gap width. The parameter α allows for a classification of the geometry in relation to the bunch and, therefore, applicable solutions for the specific scenario. Approximate, analytical solutions exist if

$$\alpha \ll 1 \tag{7.2}$$

holds true. This regime is called the *inductive* regime. On the other hand, if

$$\alpha \gg 1 \tag{7.3}$$

holds true, an approximate analytical solution exists as well. This case is referred to as the *diffractive regime*.

If α is of the order of one,

$$\alpha \sim 1, \tag{7.4}$$

approximate analytical solutions do no longer exist. In this case, only numerical simulations can be applied to determine the wake potential.

Following this classification, the RMS bunch length of $\sigma = 5$ mm in the first example is reduced by a factor of 20 to $\sigma = 250\ \mu$m. Thus, α increases from approximately 0.027 to approximately 0.533.

The wake potentials are calculated with the two directionally dispersion-free programs PBCI and ROCOCO3D.

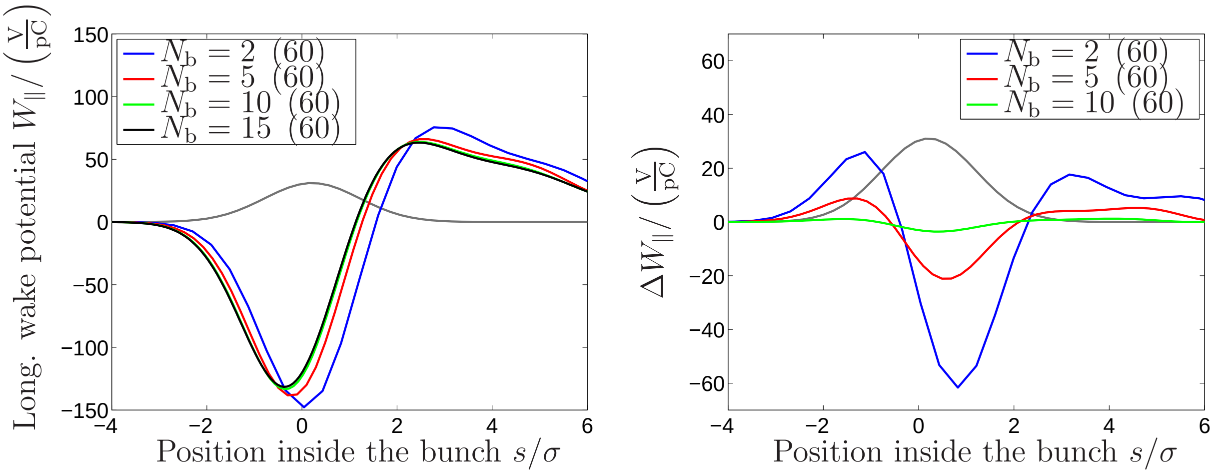

(a) The wake potential at four different resolutions.

(b) The difference of the wake potentials to the one at 15 sampling points per σ.

Figure 7.6: Comparison of four longitudinal wake potentials for a bunch with an RMS length of $\sigma = 250$ μm. The resolutions for the results calculated by PBCI are 2, 5, 10 and 15 sampling points per σ. There are 60 modes considered for the mode expansion for the indirect integration.

In Fig. 7.6(a), four wake potentials computed by PBCI are shown. The coarsest resolution is 2 sampling points per σ. Increasing the number of sampling points shows an improvement of the results towards the wake potential obtained at the highest resolution of 15 sampling points per σ.

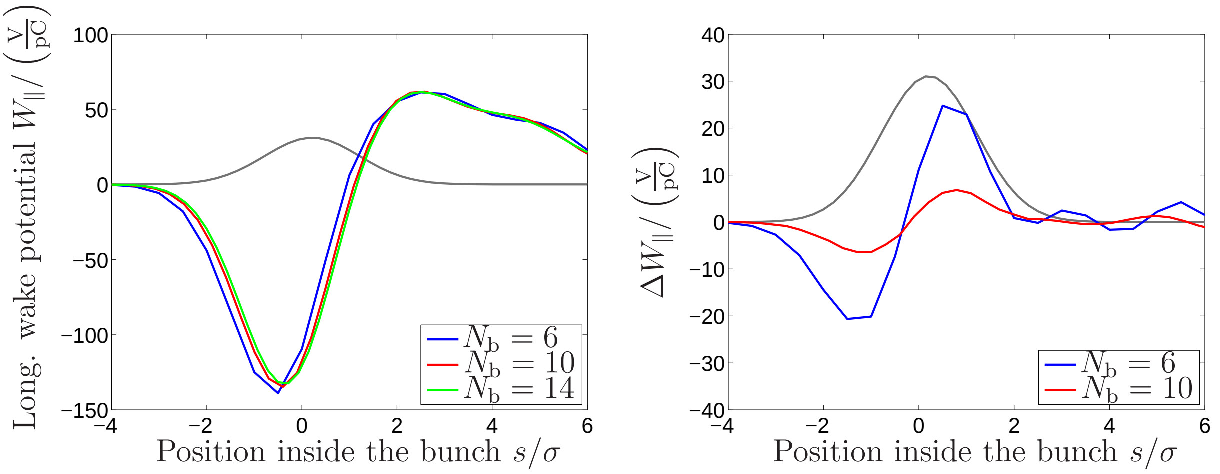

(a) The wake potential at three different resolutions.

(b) The difference of the wake potentials to the one at 14 sampling points per σ.

Figure 7.7: Comparison of three longitudinal wake potentials for a bunch with an RMS length of $\sigma = 250$ μm. The three resolutions are 6, 10 and 14 sampling points per σ. The results were obtained by ROCOCO3D using the SC boundary approximation method.

The difference between the green and the black colored wake potential curves is only marginal. This wake potential obtained at the highest resolution will be used as reference solution for the ROCOCO3D simulations below. The number of modes for the mode decomposition is 60 for all resolutions.

Analogously, the wake potential was computed using ROCOCO3D at three different resolutions (Fig. 7.7(a)). The coarsest resolution is 6 sampling points per σ, the highest is 14 sampling points per σ. The SC scheme was deployed for the approximation of the boundary. Again, the two higher resolutions show only small deviations. The result obtained at the highest resolution can be compared to the one computed with PBCI.

In Fig. 7.8(a) the results at a resolution of 14 (ROCOCO3D) and 15 (PBCI) sampling points per σ are compared to each other. The near range wake potentials of both results match extremely well. Only towards the long range wake potential small deviations occur. Thus, ROCOCO3D, compared to PBCI, exhibits a good result for the analytically inaccessible region of $\alpha \sim 1$.

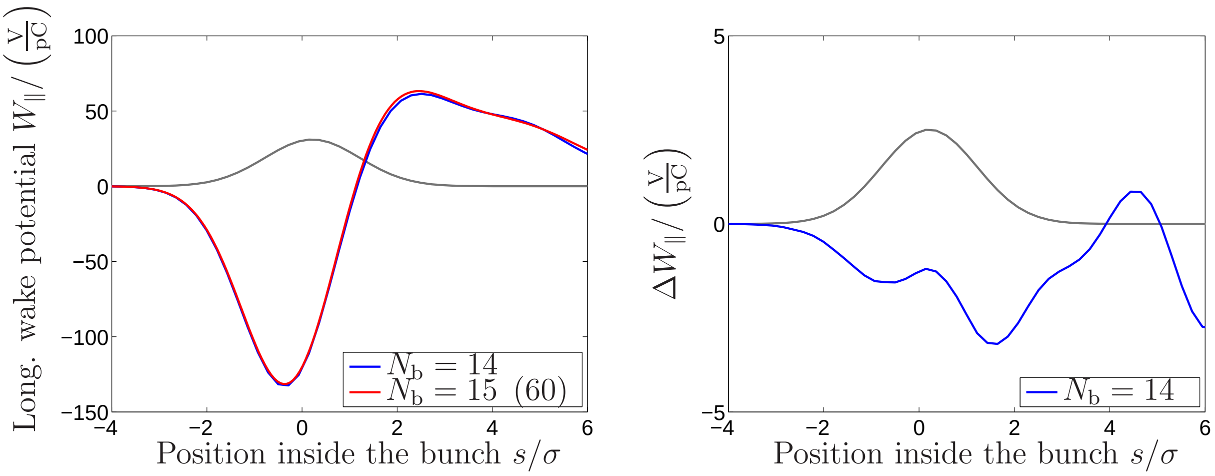

(a) The two wake potentials obtained by applying PBCI ($N_\mathrm{b} = 15$ (60)) and ROCOCO3D ($N_\mathrm{b} = 14$).

(b) The difference of the wake potential obtained by ROCOCO3D to the one obtained by PBCI.

Figure 7.8: Comparison of two longitudinal wake potentials obtained by applying two different dispersion-free numerical simulation tools at a comparable spatial resolution. The result computed using PBCI has 15 sampling points per σ (Fig. 7.6(a)). The result computed using ROCOCO3D has 14 sampling points per σ (Fig. 7.7(a)).

Finally, the numbers of degrees of freedom for these simulations presented in Fig. 7.8(a) are given. In PBCI the number of mesh cells is about 1.25 billion. The number of mesh cells in ROCOCO3D is 234 million. The ratio of these two numbers is approximately 5.3. This ratio was already derived in section 4.1.1.

7.2 TESLA Module

The TESLA nine-cell cavity is deployed in the beamline of an accelerator, e.g. in the X-FEL, in order to increase the energy of the bunch traveling through it. It is operated at a frequency of 1.3 GHz, and it is superconducting to minimize losses. Therefore, the PEC assumption for the metallic material holds true. The following simulations are performed with a TESLA nine-cell cavity without RF input coupler and without HOM couplers (Fig. 7.9) in order to obtain a cylindrically symmetric structure.

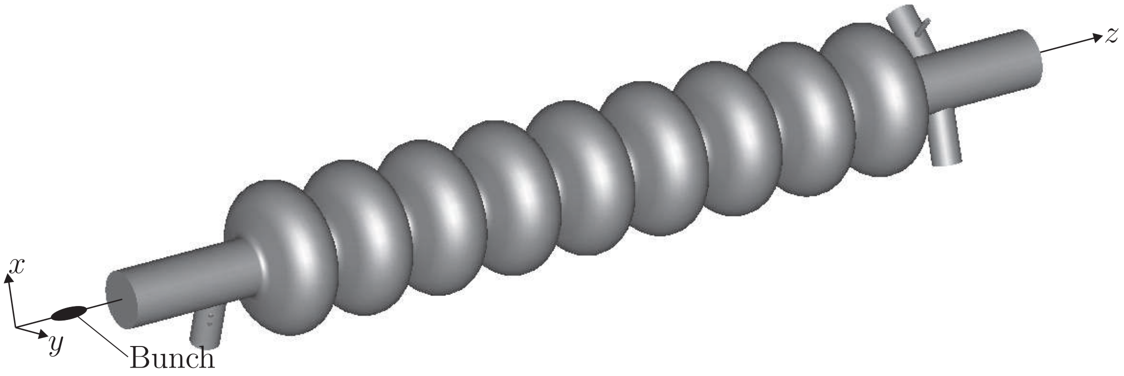

Figure 7.9: The CAD model of the TESLA nine-cell cavity. Its length is 1.1 m. The electron bunch travels along the z-axis at the speed of light.

In Fig. 7.10(a), the wake potential for a Gaussian shaped bunch with an RMS length of $\sigma = 1$ mm is depicted. Since the cavity is a cylindrically symmetric structure, ECHO was applied at two different resolutions. At 5 and 10 sampling points per σ, the difference of the wake potentials to each other is marginal. This result is therefore taken as a reference.

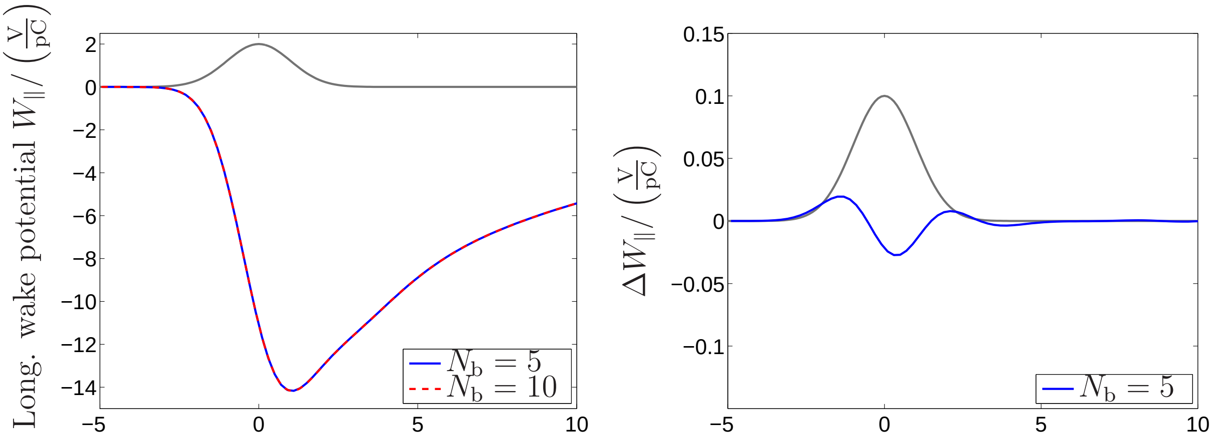

(a) The longitudinal wake potential at two different resolutions.

(b) The difference of the wake potential at 5 sampling points per σ and the one at 10 sampling points per σ.

Figure 7.10: The longitudinal wake potential of a TESLA nine-cell cavity for a bunch with RMS length $\sigma = 1$ mm. The two resolutions are 5 and 10 grid lines per sigma. The results were obtained using ECHO.

The same structure is then simulated using ROCOCO. All parameters are the same. Here, the simulations at two different resolutions exhibit a difference especially in the near range wake potential (Fig. 7.11(a)). The boundary approximation method is the USC scheme. The tubes attached to the cavity and the irises separating each of the nine single cells from each other are not perfectly smooth. An increasing resolution minimizes this effect. Additionally, the wake fields excited at the boundary parts at large radii do not contribute to the integration for the wake potential because they do not catch-up with the bunch.

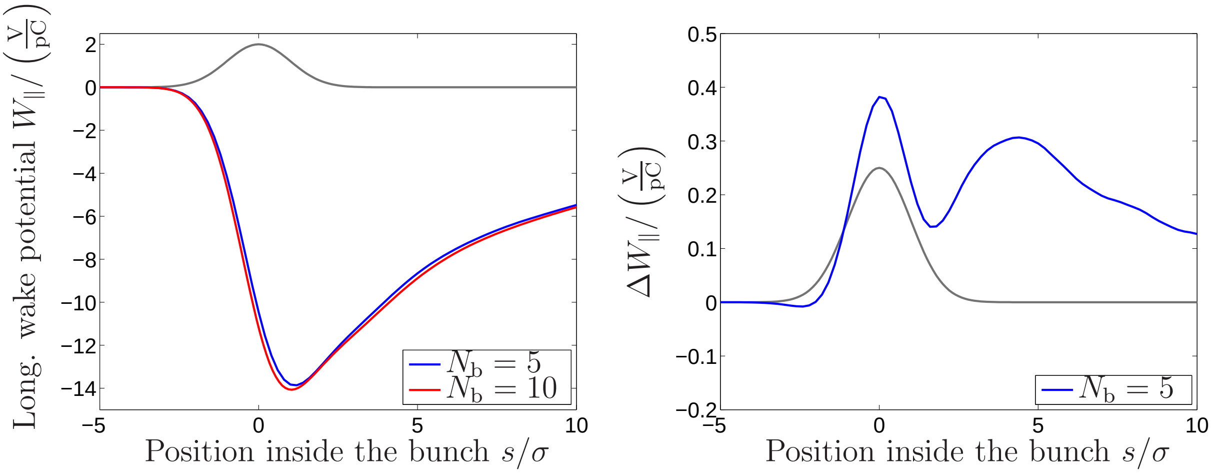

(a) The longitudinal wake potential at two different resolutions.

(b) The difference of the wake potential at 5 sampling points per σ and the one at 10 sampling points per σ.

Figure 7.11: The longitudinal wake potential of a TESLA nine-cell cavity for a bunch with an RMS length $\sigma = 1$ mm. The two resolutions used are 5 and 10 grid lines per sigma. The results were obtained using ROCOCO.

Finally, the wake potentials for the TESLA nine-cell cavity calculated using different computer codes are compared. In Fig. 7.12(a), three wake potentials are shown. The data obtained by ROCOCO and ECHO are compared at a resolution of 10 grid lines per σ. The third wake potential is obtained by ROCOCO3D. Since the cavity is a cylindrically symmetric structure, a full 3D simulation of the electromagnetic fields is not necessary. Nevertheless, it was performed to compare the 3D algorithm implemented in ROCOCO3D to a reference result obtained by two different 2D computer codes.

Due to limited memory resources, the RMS length of 1 mm was only resolved by 7 grid lines. The structure was discretized by the SC scheme.

The wake potential computed with ROCOCO3D matches the two 2D reference wake potentials very accurately. This confirms the accuracy of the rotated grid algorithm even for a comparatively low resolution of only 6 sampling points per σ.

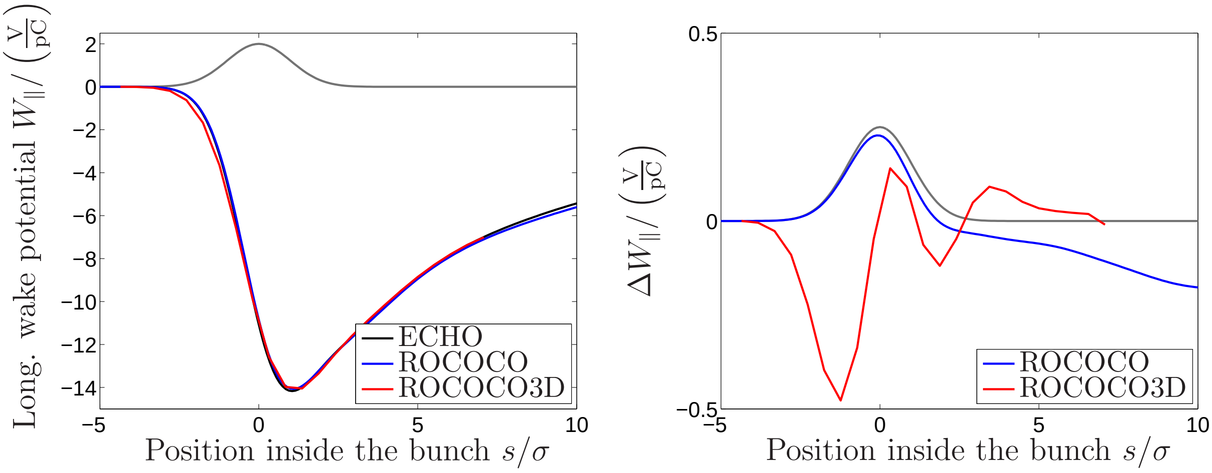

(a) The longitudinal wake potential obtained by ECHO, ROCOCO, and ROCOCO3D.

(b) The differences of the wake potentials obtained by applying ROCOCO and ROCOCO3D to the one obtained by ECHO.

Figure 7.12: Three longitudinal wake potentials for a TESLA nine-cell cavity and a bunch with an RMS length $\sigma = 1$ mm are compared. The resolution is 10 grid lines per sigma for ECHO and ROCOCO. The result obtained using ROCOCO3D has a resolution of 6 grid lines per sigma.

Chapter 8

Summary and Outlook

In this thesis an algorithm for the accurate calculation of wake potentials was developed. This was achieved by aligning inherently dispersion-free directions of the discrete space with the direction of bunch motion. In the following, the important aspects of this approach are recapitulated and the fundamental results of the numerical algorithm in the 2D and the 3D case are summarized.

First, the theory of electromagnetism was introduced in short. Thereafter, wake fields and wake potentials were presented. In order to compute wake potentials of arbitrary structures a numerical simulation technique is required. Maxwell's equations were cast into a semi-discrete form via the FIT.

Discretizing the time axis in the Maxwell-Grid-Equationsof FIT leads to fully discrete equations which are integrated in time using the leapfrog scheme allowing for the simulation of transient electromagnetic fields. In this work, the dispersion properties of the fully discretized equations were investigated. It was found that in the direction of each of the three base vectors of a Cartesian grid, the numerical dispersion errors show a maximum. In contrast to that, the dispersion errors are zero along the diagonals of a basic grid cell.

These dispersion-free directions were aligned with the preferred orientation in an accelerating structure – the direction of bunch motion. This alignment results in a rotation of the Cartesian grid. Maxwell's equations hold true in rotated coordinate systems.

Additionally, the non-conformal and conformal boundary approximation methods, the excitation of the electromagnetic fields and the calculation of the exciting field of the particle bunch on a rotated grid were described. The combination of these allows for the implementation of a directionally dispersion-free code yielding very accurate wake potential solutions.

Results

After the algorithm was described, numerical simulations were conducted to test its properties. At the beginning of the chapters which present the results of the 2D and 3D simulations, the expected dispersion properties of ROCOCO and ROCOCO3D were verified. A dispersion-free propagation along the direction of bunch motion was readily confirmed for the 3D implementation, ROCOCO3D. It was also confirmed for the 2D code, ROCOCO. However, a modification in the calculation of the material matrices in the 2D case was necessary. This modification introduces new material matrices which allow for the dispersion-free transport of a TEM wave.

Next, the programs were applied to calculate wake potentials of three resonators for which an analytical solution exists. The verification using a pillbox resonator, a spherical resonator, and a rotated cubic resonator succeeded. Nevertheless, a systematic problem of the rotated grid approach, named numerical surface roughness wake fields, was revealed. This effect was decreased by the application of conformal boundary approximation methods.

Finally, the wake potentials for two components of particle accelerators were computed, a collimator of the ILC collimator test program and a TESLA nine-cell cavity. The wake potential for the collimator for two bunches of different lengths was calculated. The result for a long bunch exciting wake fields in the inductive regime, as well as the result for a short bunch exciting wake fields in the intermediate regime showed a good agreement compared to results obtained by other well-established simulation tools. The main challenge for the TESLA nine-cell cavity is its length compared to the short length of the bunch. Therefore, it is of major importance to apply a dispersion-free algorithm in combination with the resource-friendly moving window technique. The results of the 2D code and the 3D code coincided and showed a good agreement to the result obtained with ECHO.

In conclusion, the employment of a rotated grid with the FIT leads to a algorithm well-suited for the calculation of accurate wake potentials. The main benefit of the new algorithm is its saving of computational time in comparison to other existing computer codes, e.g. PBCI and ECHO. Both programs, ROCOCO and ROCOCO3D, are accurate and reliable tools supporting the design of accelerator structures.

Outlook

The results presented in this thesis prove the applicability of the algorithm. Short bunches require a high spatial resolution leading to higher memory demands and increased computational time, especially in the 3D case. This can be remedied by a parallelization of the code.

In order to reduce the numerical surface roughness wake fields, a closer look at the boundary approximation is necessary. The USC scheme is computationally expensive and due to its non-local character it would deteriorate the parallel performance. From this point of view, the SC scheme is more advantageous, but it has a lower order of convergence.

A parallelized code in conjunction with a second order convergent and computationally cheap conformal boundary approximation method would be desirable.

Appendix A

Calculation of the Initial Fields for the Leapfrog Scheme

The leapfrog scheme, being a recursive time update scheme, requires a set of initial fields. The initial electric scattered field can be computed by equation (4.30) from the exciting electric field. The sum of the exciting and the scattered field fulfill the boundary conditions on the boundary of the computational domain.

The initial magnetic scattered field, however, has still to be determined. For the case of a charge distribution traveling at the speed of light in an infinite tube, the initial magnetic scattered field can be computed directly from the initial electric scattered field.

Six electric edge voltages connected to a primary grid node (Fig. A.1) are interpolated component-wise in order to obtain a vector of the electric voltage at the position of the node,

$$\begin{pmatrix} \overset{\frown}{e}{}^0_x \\ \overset{\frown}{e}{}^0_y \\ \overset{\frown}{e}{}^0_z \end{pmatrix} = \frac{1}{2} \cdot \begin{pmatrix} \overset{\frown}{e}{}^0_{x,+} + \overset{\frown}{e}{}^0_{x,-} \\ \overset{\frown}{e}{}^0_{y,+} + \overset{\frown}{e}{}^0_{y,-} \\ \overset{\frown}{e}{}^0_{z,+} + \overset{\frown}{e}{}^0_{z,-} \end{pmatrix} . \tag{A.1}$$

The subscripts + and − denote the edges pointing towards the node P and away from it, respectively.

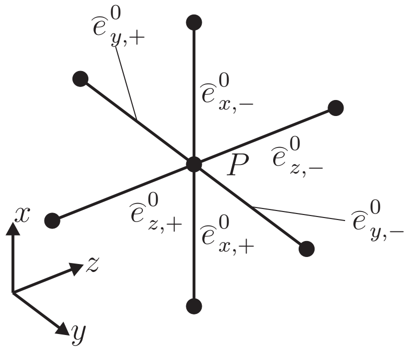

Figure A.1: Interpolation scheme of the six edge voltages of the exciting electric field attached to the primary grid node.

The resulting vector of electric voltages is transformed applying a rotary matrix $\mathbf{R}_z\left(\frac{\pi}{2}\right)$ which transforms the radial base vector into the azimuthal base vector

$$\mathbf{R}_z \cdot \vec{e}_r = \vec{e}_\phi. \tag{A.2}$$

Afterwards, the transformed vector is scaled with the vacuum impedance Z_0 and the magnetic voltage vector located at the primary grid node P is obtained by

$$\begin{pmatrix} \widehat{h}_x^0 \\ \widehat{h}_y^0 \\ \widehat{h}_z^0 \end{pmatrix} = \frac{1}{Z_0}\mathbf{R}_z \cdot \begin{pmatrix} \widehat{e}_x^0 \\ \widehat{e}_y^0 \\ \widehat{e}_z^0 \end{pmatrix}. \tag{A.3}$$

The magnetic voltages are allocated on the dual grid edges and are obtained by a second interpolation. Four magnetic field vectors allocated at the primary grid nodes forming the face which is stabbed by the dual edge, contribute to the magnetic edge voltage (Fig. A.2).

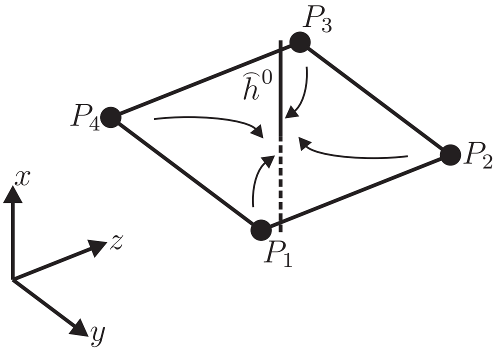

Figure A.2: The magnetic voltages are calculated at the primary grid nodes following the procedure described above. In a second step, they are brought to the position of the dual edge in order to obtain the required dual edge voltages.

The initial magnetic scattered field is now calculated correctly in terms of its spatial position. However, a shift in time of $\frac{\Delta t}{2}$ relative to the initial electric scattered field has to be additionally applied, which is an essential property of the leapfrog scheme.

The time-dependency corresponding to the time t of the electric field is given by the right hand side of equation (A.4). In order to shift the initial magnetic scattered field by half a time step, the right hand side of equation (A.4) has to be multiplied by a shift factor ξ

$$\xi \cdot \exp\left(-\frac{\left(z - c_0 t\right)^2}{2\sigma^2}\right) = \exp\left(-\frac{\left(z - c_0 t - \frac{1}{2}c_0\Delta t\right)^2}{2\sigma^2}\right), \tag{A.4}$$

yielding

$$\xi = \exp\left(c_0\Delta t \cdot \frac{z - c_0 t - \frac{1}{4}c_0\Delta t}{2\sigma^2}\right). \tag{A.5}$$

The initial magnetic and electric voltages corresponding to the staggered time update scheme (Fig. 3.10) are established consistently.

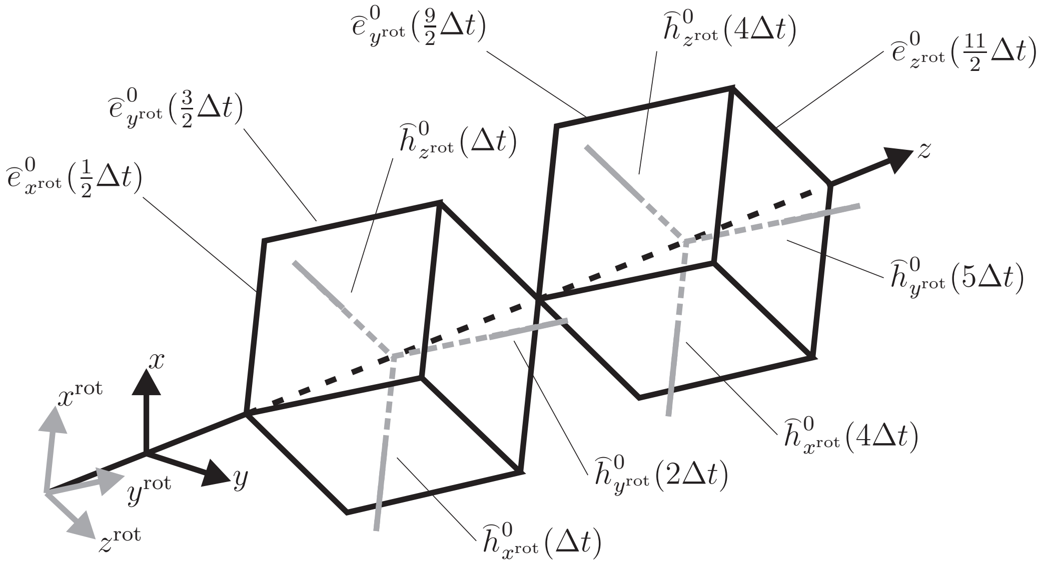

Figure A.3: Two rotated primary mesh cells are stabbed on their faces by dual grid edges (gray). The six magnetic grid voltages are shown along with their allocation in time. As an example, a few electric grid voltages are shown in order to indicate the staggered grid of the time update scheme.

All calculations concerning $\widehat{\mathbf{h}}^{0}$ and $\widehat{\mathbf{h}}^{\mathrm{s}}$ are done in the vacuum. Analogously to equation (4.30), the initial scattered magnetic grid voltages are adjusted to the vacuum part. For the PEC part or the partially filled cells (PFC) of the computational domain Ω it follows,

$$\widehat{\mathbf{h}}^{\mathrm{s}}_{m+1} = \begin{cases} -\widehat{\mathbf{h}}^{0}_{m+1} & \text{f. PEC} \\ -\bar{f}_{\widetilde{\mathrm{L}}} \cdot \widehat{\mathbf{h}}^{0}_{m+1} & \text{f. PFC} \\ 0 & \text{f. VAC} \end{cases} , \tag{A.6}$$

where $\bar{f}_{\widetilde{\mathrm{L}}}$ is the scaled part of the dual grid edge which is located in the PEC medium.

Appendix B

Modification of the Permeability Matrix in the 2D Case

The dispersion properties of a plane wave in the discretized space are investigated by means of a von Neumann dispersion analysis. In section 3.3, the dispersion relation for a Cartesian grid is obtained (eqn. (3.38)). In the following, the same analysis is carried out for a cylindrically symmetric grid with a rotated r/z-plane.

Therefore, the diagonal material matrices of the FIT defined for a Cartesian coordinate system require a modification. The proper radius-dependent values for the entries of the material matrices are obtained by dividing $\widehat{\widehat{b}}(n)$ by $\widehat{h}(n)$ and $\widehat{\widehat{d}}(n)$ by $\widehat{e}(n)$. This would lead to correct matrices $\mathbf{M}_{\mu^{-1}}$ and $\mathbf{M}_{\epsilon^{-1}}$. However, the fields $\vec{E}$, $\vec{D}$ and $\vec{H}$, $\vec{B}$ are unknown. For this reason, a different way of adapting the material matrix entries is demanded. In order to reflect the rotational symmetry in the material matrices, equations (3.16a-3.16b) are evaluated according to the rotated grid in ROCOCO (Fig. B.1).

The length of the dual grid edge along an azimuthal path is

$$\Delta\widetilde{\phi}^{\mathrm{rot}}(n) = 2\pi\, r(n), \tag{B.1}$$

and the area of the lateral surface of the conical frustum (Fig. B.1) is given by

$$\widetilde{A}^{\mathrm{rot}}(n) = 2\pi r(n)\sqrt{2}\Delta z^{\mathrm{rot}}(n). \tag{B.2}$$

This introduces an approximation into the entries of the material matrices. The adapted matrix entries in free space for the rotated grid now read for $\mathbf{M}_{\mu^{-1}}$ as

$$\left(\mathbf{M}^{\mathrm{approx}}_{\mu^{-1}}\right)(n) = \frac{2\pi\, r(n)}{\mu_0\, A^{\mathrm{rot}}(n)}, \tag{B.3}$$

and for $\mathbf{M}_{\epsilon^{-1}}$ as

$$(\mathbf{M}^{\mathrm{approx}}_{\epsilon^{-1}})\,(n) = \frac{\Delta z^{\mathrm{rot}}(n)}{\epsilon_0\, 2\pi\, r(n)\sqrt{2}\,\Delta z^{\mathrm{rot}}(n)}. \tag{B.4}$$

The equations (B.3 and B.4) for the approximated values for the entries of $\mathbf{M}_{\mu^{-1}}$ and $\mathbf{M}_{\epsilon^{-1}}$ lead just as in the Cartesian case to purely diagonal material matrices.

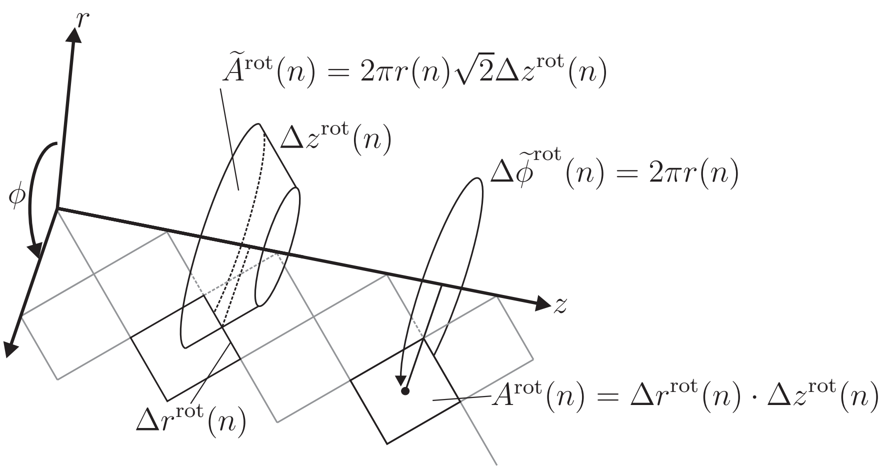

Figure B.1: Geometrical entities needed for the calculation of rotationally symmetric material matrices. The lateral surface of the conical frustum (gray) defines the dual area needed in $\mathbf{M}_{\epsilon^{-1}}$ and the circumference of the circle (black) results in the length of the dual edge.

The inverse of the entries of $\mathbf{M}^{\text{approx}}_{\mu_0^{-1}}$ (eqn. (B.3)) are shown in Fig. B.2. In comparison to these, for a TEM wave traveling in a coaxial cable, the accurate entries for $\mathbf{M}_{\mu_0}$ are shown. The ratio $-\widehat{\widehat{b}}(n)/\widehat{h}(n)$ is calculated in two different ways: On the one hand using sampled field values, on the other hand using integrated state values. Thus leading to matrices called $\mathbf{M}^{\text{sample}}_{\mu_0^{-1}}$ and $\mathbf{M}^{\text{state}}_{\mu_0^{-1}}$.

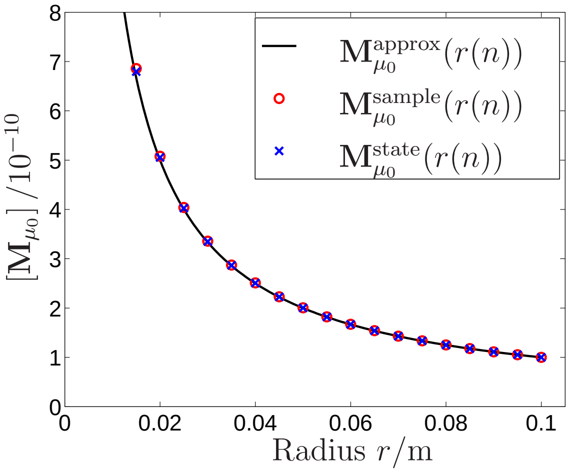

Figure B.2: The matrix entries for $\mathbf{M}^{\text{approx}}_{\mu_0}$ compared to the entries of $\mathbf{M}^{\text{sample}}_{\mu_0}$ and $\mathbf{M}^{\text{state}}_{\mu_0}$. Their differences are shown in Fig. B.3 versus the radius r.

The differences of $\mathbf{M}^{\text{sample}}_{\mu_0^{-1}}$ and $\mathbf{M}^{\text{state}}_{\mu_0^{-1}}$ to $\mathbf{M}^{\text{approx}}_{\mu_0^{-1}}$ are shown in (Fig. B.3).

However, running a test for the dispersion properties of a TEM wave propagating in a coaxial cable does not produce the expected result (sec. 5.1). Due to the approximation introduced, the TEM wave cannot propagate without generating numerical dispersion

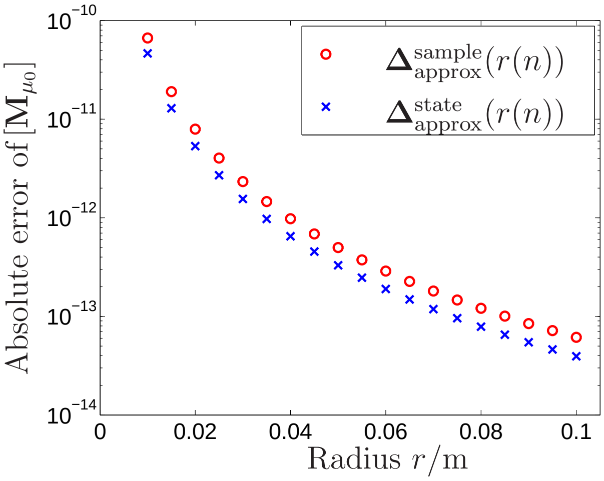

Figure B.3: Logarithmic plot of the absolute differences of $\boldsymbol{\Delta}^{\mathrm{sample}}_{\mathrm{approx}} = \mathbf{M}^{\mathrm{approx}}_{\mu 0} - \mathbf{M}^{\mathrm{sample}}_{\mu 0}$ and $\boldsymbol{\Delta}^{\mathrm{state}}_{\mathrm{approx}} = \mathbf{M}^{\mathrm{approx}}_{\mu 0} - \mathbf{M}^{\mathrm{state}}_{\mu 0}$ versus the radius r.

errors (Fig. 5.3).

A remedy for this inaccuracy is an element-wise correction of the equations (B.3 and B.4) by a factor f_{corr}, reproducing the correct entries of $\mathbf{M}_{\mu_0^{-1}}$ and $\mathbf{M}_{\epsilon_0^{-1}}$

$$\mathbf{M}^{j}_{\epsilon^{-1}} = f^{\epsilon,j}_{\mathrm{corr}} \cdot \mathbf{M}^{\mathrm{approx}}_{\epsilon^{-1}}, \qquad (B.5\mathrm{a})$$

$$\mathbf{M}^{j}_{\mu^{-1}} = f^{\mu,j}_{\mathrm{corr}} \cdot \mathbf{M}^{\mathrm{approx}}_{\mu^{-1}} \qquad j \in \{\mathrm{sample}, \mathrm{state}\}. \qquad (B.5\mathrm{b})$$

The correction factors $f^{\epsilon,j}_{\mathrm{corr}}$ and $f^{\mu,j}_{\mathrm{corr}}$ are calculated by the comparison of the approximative material matrices and the accurate material matrices. Thus, the radius-dependent correction factors only depend on the spatial spacing of the grid (Fig. B.4).

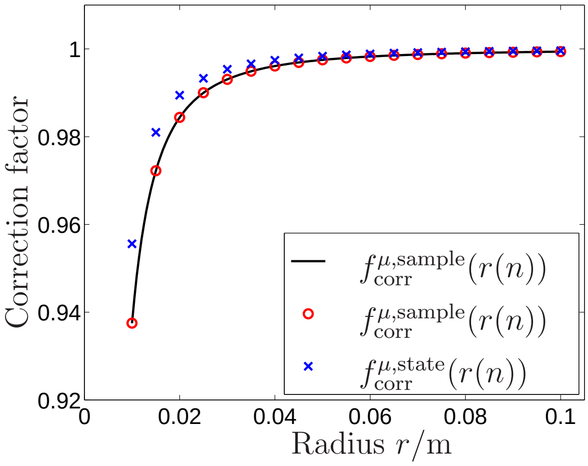

Figure B.4: The correction factors f^{μ}_{corr} for sampled field values and for integrated state values are compared to the correction factor given in equation (B.6b) versus the radius r.

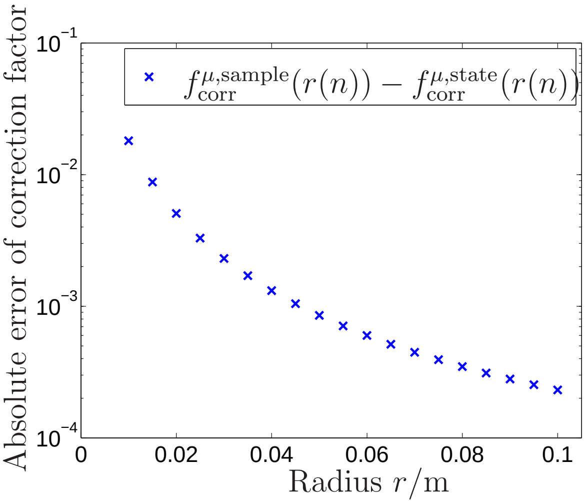

Figure B.5: Logarithmic plot of the absolute difference of the correction factor for integrated state values and sampled field values from Fig. B.4. The latter one matches the analytically closed form given in equation (B.6b).

For the special case of a TEM wave and sampled field values, an analytical expression of the correction factor (Fig. B.4) is possible and reads as follows

$$f^{\epsilon,\mathrm{sample}}_{\mathrm{corr}} = 1 \tag{B.6a}$$

$$f^{\mu,\mathrm{sample}}_{\mathrm{corr}} = 1 - \left(\frac{\Delta r}{2\,r}\right)^2 . \tag{B.6b}$$

The property of $f^{\mu,\mathrm{sample}}_{\mathrm{corr}}$ at large radii

$$\lim_{r\to\infty} f^{\mu,\mathrm{sample}}_{\mathrm{corr}} = 1, \tag{B.7}$$

shows that the approximated material matrices are consistent with the accurate matrices. In contrast to that, in the vicinity of the axis the correction factor is not negligible. Fig. 5.4 illustrates this behavior in section 5.1.

The impact of the correction factor is exemplified by a TEM wave propagating through a rotated and a non-rotated grid cell using sampled field values. In Fig. B.6, the electric grid voltages $\widehat{e}_z\left(r_{\mathrm{u}}\right)$ and $\widehat{e}_z\left(r_{\mathrm{d}}\right)$ are zero for a TEM wave. The remaining two electric grid voltages are allocated at the radius r_{m}. The magnetic grid voltage $\widehat{h}_\phi\left(r_{\mathrm{m}}\right)$ is allocated at r_m. Calculating the curl of the electric grid voltages reproduces the magnetic grid voltage:

$$\begin{aligned}
-2\pi r_{\mathrm{m}} \frac{H^{\mathrm{TEM}}_\phi\left(r_{\mathrm{m}}, t+\frac{\Delta t}{2}\right) - H^{\mathrm{TEM}}_\phi\left(r_{\mathrm{m}}, t-\frac{\Delta t}{2}\right)}{\Delta t} &= \\
\frac{2\pi r_{\mathrm{m}}}{\mu_0 \Delta r \Delta z}\Big(-\Delta r E^{\mathrm{TEM}}_r\left(r_{\mathrm{m}}, t\right) + \Delta r E^{\mathrm{TEM}}_r\left(r_{\mathrm{m}}, t\right)\exp\left(-ik_z\Delta z\right)\Big)&.
\end{aligned} \tag{B.8}$$

The corresponding equation for a rotated grid cell (Fig. B.7) does not hold true. The electric grid voltages are allocated at the radii r_{d} and r_{u}, whereas the magnetic grid

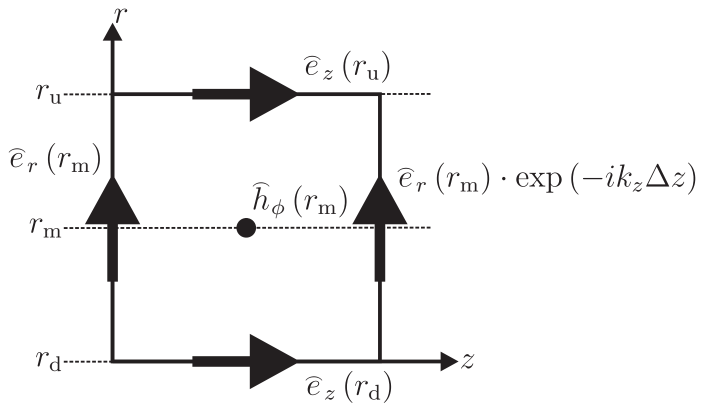

Figure B.6: A TEM wave traveling through a non-rotated grid cell. The electric grid voltage $\widehat{e}_r$ is transported along the z-axis.

voltage is still allocated at r_{m}. If $\mathbf{M}_{\mu_0}^{\mathrm{approx}}$ is applied, the curl of the electric grid voltages does not reproduce the magnetic grid voltage

$$-2\pi r_{\mathrm{m}}\frac{H_\phi^{\mathrm{TEM}}\left(r_{\mathrm{m}},t+\frac{\Delta t}{2}\right)-H_\phi^{\mathrm{TEM}}\left(r_{\mathrm{m}},t-\frac{\Delta t}{2}\right)}{\Delta t}\neq\frac{2\pi r_{\mathrm{m}}}{\mu_0\Delta r^{\mathrm{rot}}\Delta z^{\mathrm{rot}}}\Big(-\Delta r^{\mathrm{rot}}E_{r^{\mathrm{rot}}}^{\mathrm{TEM}}\left(r_{\mathrm{u}},t\right)+ \Delta z^{\mathrm{rot}}E_{z^{\mathrm{rot}}}^{\mathrm{TEM}}\left(r_{\mathrm{d}},t\right)+\Delta r^{\mathrm{rot}}E_{r^{\mathrm{rot}}}^{\mathrm{TEM}}\left(r_{\mathrm{d}},t\right)\exp\left(-ik_z\Delta z\right)-\Delta z^{\mathrm{rot}}E_{z^{\mathrm{rot}}}^{\mathrm{TEM}}\left(r_{\mathrm{u}},t\right)\exp\left(-ik_z\Delta z\right)\Big)\,. \tag{B.9}$$

Applying the correction factor, an effective permeability μ_{eff} is introduced for the grid cell

$$\mu_{\mathrm{eff}}=\frac{2\pi r_{\mathrm{m}}}{\mu_0\Delta r^{\mathrm{rot}}\Delta z^{\mathrm{rot}}}f_{\mathrm{corr}}^{\mu,\mathrm{sample}}, \tag{B.10}$$

and equation (B.9) holds true.

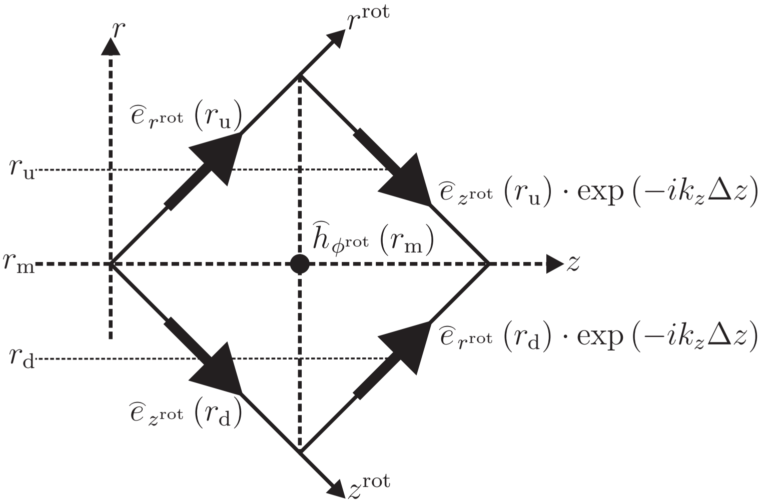

Figure B.7: A TEM wave traveling through a rotated grid cell. The electric grid voltages $\widehat{e}_{r^{\mathrm{rot}}}$ and $\widehat{e}_{z^{\mathrm{rot}}}$ are transported along the z-axis.

Appendix C

The Wake Potential of a Rotated Cubic Resonator

The analytical calculation of wake potentials is possible only in very rare cases. Two of these solutions are used for comparison in chapters 5 and 6. One for a relativistic bunch propagating through a cylindrical resonator [41] and the other for a spherical resonator [42]. Applying the modal approach used in the aforementioned papers, the calculation of the wake potential in a rotated cubic resonator succeeds.

The longitudinal wake potential of a point-like charge propagating through a resonator is given by [45, 46]

$$W_{\parallel}^{p}\left(s\right) = -2Q\sum_{\xi} k_{\xi}\cos\left(\omega_{\xi}\frac{s}{c_0}\right). \tag{C.1}$$

For the computation of the loss factor each resonant mode ξ has to be known, as well as the corresponding angular frequency ω_{ξ}.

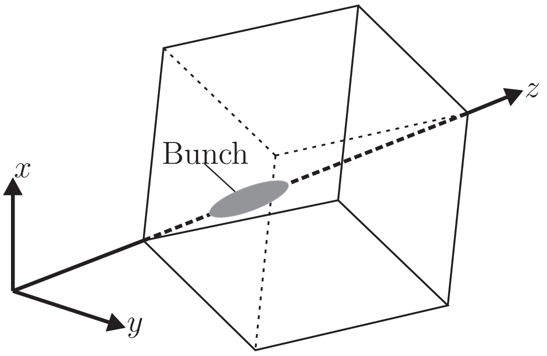

Figure C.1: A cube of edge length a rotated by the angles given in chapter 4, namely −45° about $\vec{e}_z$ and −54.7° about $\vec{e}_y$. The resonator resembles a structure which can be perfectly filled with rotated mesh cells. Therefore, the bunch crosses the resonator on a path along the cube diagonal.

In Fig. C.1, the rotated cubic resonator is shown. The cavity itself is a rectangular box resonator with equally long sides. The electron bunch or a point-like particle travels along the cube's diagonal. In the following calculation the electron bunch is represented by a line charge distribution.

The resonant modes of a rectangular box resonator are obtained from a textbook [47]. For the computation of the loss factor

$$k_\xi = \frac{V_\xi V_\xi^*}{4U_\xi}, \tag{C.2}$$

only an appropriate parameterization of the volume of the resonator is needed. Then, the integrals determining V_ξ, the voltage induced by a point-like charge, and U_ξ, the energy stored in the mode ξ, are calculated.

The result is the longitudinal wake potential of a point-like charge which corresponds to the wake function (eqn. (2.16)). In order to obtain the longitudinal wake potential $W_\parallel^G$ for a Gaussian line charge distribution λ_G with an RMS length σ of the bunch, the convolution

$$W_\parallel^G(s) = \int_0^\infty W_\parallel^p(\tau)\, \lambda_G(\tau - s)\, \mathrm{d}\tau \tag{C.3}$$

has to be calculated. The longitudinal wake potential $W_\parallel^G$ then reads as follows

$$\begin{aligned} W_\parallel^G(s) = -\frac{3\,\exp\left(\frac{s^2}{2}\right)}{4\,a\,\epsilon_0} \Bigg(& \sum_{\substack{m,n,p\\ p\neq 0}} f^{\mathrm{TE}}_{m,n,p}\, \Re\left\{ w\left(\frac{\omega_{m,n,p}\,\sigma}{c_0\sqrt{2}} - \frac{\mathrm{i}\,s}{\sqrt{2}} \right)\right\} + \\ & \sum_{\substack{m,n,p\\ m\neq 0\,\wedge\, n\neq 0}} f^{\mathrm{TM}}_{m,n,p}\, \Re\left\{ w\left(\frac{\omega_{m,n,p}\,\sigma}{c_0\sqrt{2}} - \frac{\mathrm{i}\,s}{\sqrt{2}} \right)\right\} \Bigg) \end{aligned} \tag{C.4}$$

with $w(x)$ being the complex error function [48] and:

$$\omega_{m,n,p} = \frac{c_0\,\pi}{a}\sqrt{m^2+n^2+p^2},$$

$$\Omega_{m,n,p} = \pi\sqrt{3}\sqrt{m^2+n^2+p^2},$$

$$\begin{aligned} f^{\mathrm{TE}}_{m,n,p} = \frac{\Omega^2_{m,n,p}\left(1-(-1)^{m+n+p}\cos\left(\Omega_{m,n,p}\right)\right)}{m^2+n^2} \Bigg(& \frac{m-n}{(p-m-n)^2\,\pi^2-\Omega^2_{m,n,p}} + \\ & \frac{m+n}{(p-m+n)^2\,\pi^2-\Omega^2_{m,n,p}} + \frac{-m-n}{(p+m-n)^2\,\pi^2-\Omega^2_{m,n,p}} + \frac{-m+n}{(p+m+n)^2\,\pi^2-\Omega^2_{m,n,p}} \Bigg) \end{aligned}$$

$$\begin{aligned} f^{\mathrm{TM}}_{m,n,p} = \frac{\Omega^2_{m,n,p}\left(1-(-1)^{m+n+p}\cos\left(\Omega_{m,n,p}\right)\right)}{\left(m^2+n^2\right)\left(m^2+n^2+p^2\right)} \Bigg(& \frac{m^2+n^2+p(m+n)}{(p-m-n)^2\,\pi^2-\Omega^2_{m,n,p}} + \\ & \frac{-m^2-n^2+p(-m+n)}{(p-m+n)^2\,\pi^2-\Omega^2_{m,n,p}} + \frac{-m^2-n^2+p(m-n)}{(p+m-n)^2\,\pi^2-\Omega^2_{m,n,p}} + \frac{m^2+n^2+p(-m-n)}{(p+m+n)^2\,\pi^2-\Omega^2_{m,n,p}} \Bigg) \end{aligned}$$

Appendix D

The Transformation of Relativistic Fields

In this appendix, the transformation of the electromagnetic fields of a particle with charge q in a frame K' to a second frame K is calculated. The velocity of q with respect to the frame K is $v\,\vec{e}_z$, thus $\vec{\beta} = \frac{v}{c_0}\,\vec{e}_z$. The particle q is at rest in the frame K', carrying the spherically symmetric electric field of a point-like charge; the magnetic field is zero

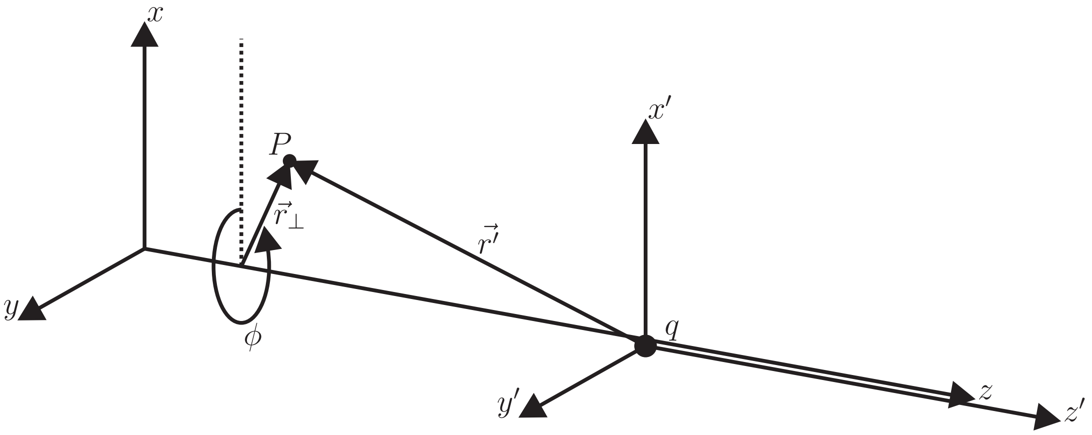

Figure D.1: The point-like charge q in the frame K' travels along the z-axis of the frame K. The relative velocity of K' with respect to K is v.

$$\vec{E'} = \frac{Q}{4\pi\epsilon_0}\frac{\vec{r'}}{r'^3}, \qquad \vec{B'} = 0. \tag{D.1}$$

The fields of the frame K' are transformed to the frame K by the following transformation formulae [28]:

$$\vec{E} = \gamma\vec{E'} - \frac{\gamma^2}{\gamma+1}\vec{\beta}\left(\vec{\beta}\cdot\vec{E'}\right) \tag{D.2a}$$

$$\vec{B} = \frac{1}{c_0}\vec{\beta}\times\vec{E}. \tag{D.2b}$$

However, the spatial and temporal coordinates have to be transformed as well:

$$x' = x, \qquad y' = y, \qquad z' = \gamma\,(z - vt)\,. \tag{D.3}$$

An arbitrary point P in K with coordinates $(r_\perp, \phi, z)^T$ is located with respect to the frame K' at

$$\vec{r'} = \vec{r}_\perp + \gamma\,(z - vt)\,\vec{e}_z. \tag{D.4}$$

Thus, the electric field of the point-like charge is expressed in the frame K' with coordinates of K as

$$\vec{E'} = \frac{Q}{4\pi\epsilon_0}\,\frac{\vec{r}_\perp + \gamma\,(z - vt)\,\vec{e}_z}{\left(r_\perp^2 + \gamma^2\,(z - vt)^2\right)^{\frac{3}{2}}}. \tag{D.5}$$

Finally, the fields are transformed by equation (*D*.2a)

$$\vec{E} = \gamma\frac{Q}{4\pi\epsilon_0}\,\frac{\vec{r}_\perp + \gamma\,(z - vt)\,\vec{e}_z}{\left(r_\perp^2 + \gamma^2\,(z - vt)^2\right)^{\frac{3}{2}}}, \tag{D.6}$$

resulting in an electric field in K.

Equation (D.6) gives an expression for the electric field at any point P in K for a point-like electric charge passing an observer at this point P at a speed

$$0 \leq v < c_0. \tag{D.7}$$

Increasing the speed of the particle, the electric as well as the magnetic field contracts longitudinally. The spherical symmetry is broken and the field distribution becomes ellipsoid-like. In the limit of $\gamma \to \infty$, the electric field $\vec{E}$ can be written as a delta function

$$\lim_{\gamma\to\infty}\frac{\gamma}{(C_1^2 + C_2^2\gamma^2)^{\frac{3}{2}}} = \frac{2}{C_1^2}\delta\,(C_2)\,. \tag{D.8}$$

Thus, the electric field is contracted into a plane perpendicular to $\vec{e}_z$ at $z - vt$ for ultra-relativistic velocities

$$\vec{E} = \frac{Q}{2\pi\epsilon_0}\,\frac{\vec{r}_\perp + \gamma\,(z - vt)\,\vec{e}_z}{r_\perp^2}\delta\,(z - vt) = \frac{Q}{2\pi\epsilon_0}\,\frac{\vec{r}_\perp}{r_\perp^2}\delta\,(z - vt)\,. \tag{D.9}$$

Since

$$\vec{B} = \frac{1}{c_0}\vec{\beta}\times\vec{E} \tag{D.10}$$

still holds, both the electric and magnetic field for a particle at the speed of light are:

$$\vec{E} = \frac{Q}{2\pi\epsilon_0}\,\frac{\vec{r}_\perp}{r_\perp^2}\delta\,(z - c_0 t)\,, \qquad \vec{B} = \frac{Q\mu_0 c_0}{2\pi}\,\frac{\vec{e}_z\times\vec{r}_\perp}{r_\perp^2}\delta\,(z - c_0 t) \tag{D.11}$$

Appendix E

Rotational Invariance

Maxwell's equations are rotationally invariant. In this chapter, this invariance is proven mathematically. The quantities in the set of equations (eqns. (2.5a)-(2.5d)) are vectors and scalars. The relevant operations are the dot product and the cross product.

A scalar is invariant under a rotation $\mathbf{R}$. Thus, the invariance of the dot product and the cross product has to be derived. Starting from two rotated vectors $\vec{a}^{\,\mathrm{rot}}$ and $\vec{b}^{\,\mathrm{rot}}$ connected via the dot product, the orthogonal transformation of these vectors can be written using Einstein's summation convention

$$\begin{aligned}
\vec{a}^{\,\mathrm{rot}} \cdot \vec{b}^{\,\mathrm{rot}} &= a'_i \, b'_i \\
&= r_{i,k} \, a_k \, r_{i,j} \, b_j \\
&= r_{i,k} \, r_{i,j} \, a_k \, b_j \\
&= r^T_{k,i} \, r_{i,j} \, a_k \, b_j \\
&= \delta_{k,j} \, a_k \, b_j \\
&= \vec{a} \cdot \vec{b}.
\end{aligned} \tag{E.1}$$

The left hand side $\vec{a}^{\,\mathrm{rot}} \cdot \vec{b}^{\,\mathrm{rot}}$ equals the dot product of the non-rotated vectors $\vec{a} \cdot \vec{b}$, proving the invariance stated above.

Equation (E.1) can be applied to equation (2.5c) and equation (2.5d) - Gauss' law and Gauss' law for magnetism. For the remaining two equations containing cross products, Faraday's law is taken exemplarily

$$\begin{aligned}
\nabla \times \vec{E} &= -\frac{\partial}{\partial t} \vec{B} \qquad |\mathbf{R} \cdot \\
\mathbf{R} \cdot \left(\nabla \times \vec{E} \right) &= -\mathbf{R} \cdot \frac{\partial}{\partial t} \vec{B} \\
(\mathbf{R} \cdot \nabla) \times \left(\mathbf{R} \cdot \vec{E} \right) &= -\frac{\partial}{\partial t} \left(\mathbf{R} \cdot \vec{B} \right) \\
\nabla^{\mathrm{rot}} \times \vec{E}^{\,\mathrm{rot}} &= -\frac{\partial}{\partial t} \vec{B}^{\,\mathrm{rot}}.
\end{aligned} \tag{E.2}$$

Rotating the system by the orthogonal transformation $\mathbf{R}$ leads to the same physical law in a rotated frame. The structure of Faraday's law does not change. Crucial to this proof is the equality of

$$\mathbf{R} \cdot \left(\nabla \times \vec{E}\right) \stackrel{?}{=} (\mathbf{R} \cdot \nabla) \times \left(\mathbf{R} \cdot \vec{E}\right) . \tag{E.3}$$

In order to prove equation (E.3) one assumption has to be made. The cross product itself is calculated analogously in the rotated frame as well as in the non-rotated frame. Thus, $\vec{e}_x^{\,\mathrm{rot}}$, $\vec{e}_y^{\,\mathrm{rot}}$, and $\vec{e}_z^{\,\mathrm{rot}}$ also form an orthonormal system of vectors. This can be proven applying equation (E.1):

$$\vec{e}_i^{\,\mathrm{rot}} \cdot \vec{e}_j^{\,\mathrm{rot}} = \vec{e}_i \cdot \vec{e}_j = \delta_{i,j} \qquad\qquad i, j \in \{x, y, z\} . \tag{E.4}$$

Now, the left hand side as well as the right hand side of equation (E.3) can be computed separately:

$$\begin{aligned}
\mathbf{R} \cdot \left(\nabla \times \vec{E}\right) &= \mathbf{R} \cdot \begin{vmatrix} \vec{e}_x & \vec{e}_y & \vec{e}_z \\ \partial_x & \partial_y & \partial_z \\ E_x & E_y & E_z \end{vmatrix} \\
&= \mathbf{R} \cdot \left[\vec{e}_x \cdot \begin{vmatrix} \partial_y & \partial_z \\ E_y & E_z \end{vmatrix} - \vec{e}_y \cdot \begin{vmatrix} \partial_x & \partial_z \\ E_x & E_z \end{vmatrix} \vec{e}_z \cdot \begin{vmatrix} \partial_x & \partial_y \\ E_x & E_y \end{vmatrix} \right] \\
&= \vec{e}_x^{\,\mathrm{rot}} \cdot \begin{vmatrix} \partial_y & \partial_z \\ E_y & E_z \end{vmatrix} - \vec{e}_y^{\,\mathrm{rot}} \cdot \begin{vmatrix} \partial_x & \partial_z \\ E_x & E_z \end{vmatrix} + \vec{e}_z^{\,\mathrm{rot}} \cdot \begin{vmatrix} \partial_x & \partial_y \\ E_x & E_y \end{vmatrix} ,
\end{aligned} \tag{E.5}$$

$$\begin{aligned}
& (\mathbf{R} \cdot \nabla) \times \left(\mathbf{R} \cdot \vec{E}\right) \\
= \; & (\mathbf{R} \cdot [\vec{e}_x \partial_x + \vec{e}_y \partial_y + \vec{e}_z \partial_z]) \times (\mathbf{R} \cdot [\vec{e}_x E_x + \vec{e}_y E_y + \vec{e}_z E_z]) \\
= \; & \left(\vec{e}_x^{\,\mathrm{rot}} \partial_x + \vec{e}_y^{\,\mathrm{rot}} \partial_y + \vec{e}_z^{\,\mathrm{rot}} \partial_z\right) \times \left(\vec{e}_x^{\,\mathrm{rot}} E_x + \vec{e}_y^{\,\mathrm{rot}} E_y + \vec{e}_z^{\,\mathrm{rot}} E_z\right) \\
= \; & \partial_x E_y \vec{e}_z^{\,\mathrm{rot}} - a_x E_z \vec{e}_y^{\,\mathrm{rot}} - \partial_y E_x \vec{e}_z^{\,\mathrm{rot}} + \partial_y E_z \vec{e}_x^{\,\mathrm{rot}} + \partial_z E_x \vec{e}_y^{\,\mathrm{rot}} - \partial_z E_y \vec{e}_x^{\,\mathrm{rot}} \\
= \; & \vec{e}_x^{\,\mathrm{rot}} \cdot \begin{vmatrix} \partial_y & \partial_z \\ E_y & E_z \end{vmatrix} - \vec{e}_y^{\,\mathrm{rot}} \cdot \begin{vmatrix} \partial_x & \partial_z \\ E_x & E_z \end{vmatrix} + \vec{e}_z^{\,\mathrm{rot}} \cdot \begin{vmatrix} \partial_x & \partial_y \\ E_x & E_y \end{vmatrix} .
\end{aligned} \tag{E.6}$$

Finally, comparing the results of equation (E.5) and equation (E.6) confirms the equality sign in equation (E.3).

Thus, scalars, vectors, and the vector operations, namely the dot product and the cross product, are invariant under rotations. Concluding, Maxwell's equations can be applied in a non-rotated frame or rotated frame, respectively.

Nomenclature

Classic Electromagnetics

ϵ	Permittivity
ϵ_0	Electric permittivity of vacuum
ϵ_r	Relative electric permittivity
λ_G	Charge distribution of a Gaussian shaped bunch
μ_0	Magnetic permeability of vacuum
μ_r	Relative magnetic permeability
ω	Angular frequency
ω_ξ	Angular frequency for the resonant mode ξ
ρ	Electric charge density
$\underline{\Psi}_x, \underline{\Psi}_y, \underline{\Psi}_z$	Spatial phase factors for the three spatial directions
$\underline{\vec{E}}$	Electric field
$\vec{B}'$	Magnetic induction in the moving inertial system
$\vec{B}$	Magnetic induction
$\vec{B}^{\,\mathrm{rot}}$	Magnetic induction in the rotated frame
$\vec{B}_0$	Exciting magnetic field
$\vec{B}_\mathrm{s}$	Scattered magnetic field
$\vec{D}$	Electric displacement
$\vec{E}'$	Electric field in the moving inertial system
$\vec{E}$	Electric field
$\vec{E}^{\,\mathrm{rot}}$	Electric field in the rotated frame
$\vec{E}_{0,\mathrm{tan}}$	Tangential component of the exciting electric field
$\vec{E}_0$	Exciting electric field
$\vec{E}_{\mathrm{s,tan}}$	Tangential component of the scattered electric field
$\vec{E}_\mathrm{s}$	Scattered electric field
$\vec{E}_{\mathrm{t,tan}}$	Tangential component of the total electric field
$\vec{F}_\mathrm{Lorentz}$	Lorentz-force
$\vec{H}$	Magnetic field

$\vec{J}$	Total electric current
$\vec{J}_C(\vec{r}, t)$	Impressed current
$\vec{J}_I(\vec{r}, t)$	Convective current
$\vec{J}_L(\vec{r}, t)$	Line current
$\vec{k}$	Wave vector
$\vec{M}$	Magnetization
$\vec{n}$	Direction of propagation of the wave
$\vec{P}$	Electric polarization
$\vec{W}$	Vector of wake potentials
$\vec{w}$	Wake function
$\vec{W}_\perp$	Vector of transversal wake potentials
E_r, E_z	Electric field components in the non-rotated r/z-plane
E_x, E_y, E_z	x-, y-, and z-component of the electric field
$E_{r^\mathrm{rot}}, E_{z^\mathrm{rot}}$	Electric field components in the rotated r/z-plane
H_ϕ	Azimuthal component of the magnetic field
k_ξ	Loss factor for the resonant mode ξ
k_x, k_y, k_z	Components of the wave vector
k_loss	Total loss factor
Q_1	Charge of the bunch
Q_2	Charge of the witness particle
s	Position inside the bunch
U_ξ	Energy stored in the resonant mode ξ
V_ξ	Voltage induced by a point-like charge for the resonant mode ξ
$W_\parallel^G$	Longitudinal wake potential for a Gaussian shaped bunch
$W_\parallel^p$	Longitudinal wake potential for a point-like charge
$W_\parallel$	Longitudinal wake potential
Z_0	Vacuum impedance

Finite Integration Technique

$\bar{f}_\mathrm{L}$	Scaled part of a primary grid edge in PEC
$\bar{f}_{\tilde{\mathrm{L}}}$	Scaled part of a dual grid edge in PEC
$\Delta r^\mathrm{rot}, \Delta z^\mathrm{rot}$	Spatial spacings in the rotated r/z-plane
$\Delta r, \Delta z$	Spatial spacings in the non-rotated r/z-plane
Δt	Time step
Δt_max	Maximum stable time step
$\Delta x, \Delta y, \Delta z$	Spatial spacings in the x-, y-, and z-direction

$\widetilde{G}$	Dual grid
$\widetilde{\mathbf{C}}$	Curl matrix on the dual grid
$\mathbf{M}_{\epsilon^{-1}}$	Inverse permittivity matrix
$\mathbf{M}_{\epsilon^{-1}}^{\text{approx}}$	Approximated permittivity material matrix
$\mathbf{M}_{\epsilon^{-1}}^{\text{sample}}$	Permittivity material matrix for sampled values
$\mathbf{M}_{\epsilon^{-1}}^{\text{SC}}$	Inverse permittivity material matrix with the SC scheme
$\mathbf{M}_{\epsilon^{-1}}^{\text{staircase}}$	Inverse permittivity material matrix with staircased interfaces
$\mathbf{M}_{\epsilon^{-1}}^{\text{state}}$	Permittivity material matrix for state values
$\mathbf{M}_{\epsilon^{-1}}^{\text{USC}}$	Inverse permittivity material matrix with the USC scheme
$\widehat{\widehat{\mathbf{j}}}$	Vector of grid currents
$\widehat{\widehat{j}}$	Grid current vector
$\widehat{\widehat{\mathbf{b}}}$	Vector of magnetic grid fluxes
$\widehat{\widehat{\mathbf{d}}}$	Vector of electric grid flux
$\widehat{\widehat{b}}(n)$	n-th entry in the vector of magnetic grid fluxes $\widehat{\widehat{\mathbf{b}}}$
$\widehat{\widehat{d}}(n)$	n-th entry in the vector of electric grid flux $\widehat{\widehat{\mathbf{d}}}$
$\mathbf{M}_{\epsilon}^{\text{PFC}}$	Permittivity material matrix for PFC cells
$\mathbf{M}_{\mu}^{\text{PFC}}$	Permeability material matrix for PFC cells
$\mathbf{M}_{\mu^{-1}}$	Inverse of the permeability material matrix
$\mathbf{M}_{\mu^{-1}}^{\text{approx}}$	Approximated permeability material matrix
$\mathbf{M}_{\mu^{-1}}^{\text{sample}}$	Permeability material matrix for sampled values
$\mathbf{M}_{\mu^{-1}}^{\text{SC}}$	Inverse permeability material matrix with the SC scheme
$\mathbf{M}_{\mu^{-1}}^{\text{staircase}}$	Inverse permeability material matrix with staircased interfaces
$\mathbf{M}_{\mu^{-1}}^{\text{state}}$	Permeability material matrix for state values
$\mathbf{M}_{\mu^{-1}}^{\text{USC}}$	Inverse permeability material matrix with the USC scheme
ν_c	Courant number
Ω	Computational domain
Ω_{PEC}	PEC part of Ω
Ω_{Vacuum}	Vacuum part of Ω
$\overline{\epsilon}(n)$	Averaged permittivity
$\overline{\mu^{-1}}(n)$	Averaged inverse permeability
$\partial\Omega_s$	Boundary of Ω_s
$\mathbf{C}$	Curl matrix on the primary grid
$\mathbf{C}_{\text{local}}$	Local curl matrix on the primary grid
$\widehat{\mathbf{e}}^{\text{s}}$	Scattered electric grid voltage
$\widehat{\mathbf{h}}^{\text{s}}$	Vector of scattered magnetic grid voltages
$\widehat{\mathbf{e}}^{0}$	Exciting electric grid voltage

$\widehat{\mathbf{h}}^{0}$	Vector of exciting magnetic grid voltages
σ	RMS length of the Gaussian shaped bunch
$\widehat{\mathbf{e}}^{\mathrm{t}}$	Total electric grid voltage
$\widehat{\mathbf{h}}^{\mathrm{t}}$	Vector of total magnetic grid voltages
$\underline{\Psi}_t$	Phase factor
$\widehat{\mathbf{e}}$	Vector of the electric grid voltages
$\widehat{\mathbf{h}}$	Vector of magnetic grid voltages
$\widehat{e}(n)$	n-th entry in the vector of electric grid voltages $\widehat{\mathbf{e}}$
$\widehat{h}(n)$	n-th entry in the vector of magnetic grid voltages $\widehat{\mathbf{h}}$
$\widetilde{\mathbf{C}}_{\mathrm{local}}$	Local curl matrix on the dual grid
$\widetilde{\mathbf{S}}$	Source matrix on the dual grid
A	Cell face of the grid G
f_{A}	Scaled part of the cell area in vacuum
$f_{\mathrm{corr}}^{\epsilon,\mathrm{sample}}$	Correction factor for the permittivity material matrix for sampled values
$f_{\mathrm{corr}}^{\epsilon,\mathrm{state}}$	Correction factor for the permittivity material matrix for state values
$f_{\mathrm{corr}}^{\mu,\mathrm{sample}}$	Correction factor for the permeability material matrix for sampled values
$f_{\mathrm{corr}}^{\mu,\mathrm{state}}$	Correction factor for the permeability material matrix for state values
f_{corr}^{μ}	Correction factor for the permeability
f_{L}	Scaled part of the edge length in vacuum
G	Primary grid
k, l, m	Indices corresponding to x, y and z
L	Cell edge of the grid G
$M_{\epsilon}(n)$	n-th entry in the permittivity material matrix
$M_{\mu}(n)$	n-th entry in the permeability material matrix
n	Canonic index of cell
$N_{\mathrm{b}}^{\mathrm{2D,rot}}$	Number of sampling points in the rotated 2D grid
$N_{\mathrm{b}}^{\mathrm{2D}}$	Number of sampling points in the non-rotated 2D grid
$N_{\mathrm{b}}^{\mathrm{3D,rot}}$	Number of sampling points in the rotated 3D grid
$N_{\mathrm{b}}^{\mathrm{3D}}$	Number of sampling points in the non-rotated 3D grid
$N_{\mathrm{DoF}}^{\mathrm{2D,rot}}$	Number of degrees of freedom in the rotated 2D grid
$N_{\mathrm{DoF}}^{\mathrm{2D}}$	Number of degrees of freedom in the non-rotated 2D grid
$N_{\mathrm{DoF}}^{\mathrm{3D,rot}}$	Number of degrees of freedom in the rotated 3D grid
$N_{\mathrm{DoF}}^{\mathrm{3D}}$	Number of degrees of freedom in the non-rotated 3D grid
N_p	Number of grid points

N_x, N_y, N_z	Number of grid lines in x, y and z direction
P	Node of the grid G
$P_1 \dots P_8$	Nodes on the primary grid
$q(n)$	n-th entry in the cell charge vector $\mathbf{q}$
Q_{cell}	Electric charge in a primary volume V
V	Cell volume of the grid G
$\widetilde{\mathbf{S}}$	Source matrix on the dual grid
$\mathbf{A}^{\mathrm{SC}}$	System matrix with the SC scheme
$\mathbf{A}^{\mathrm{staircase}}$	System matrix with staircased interfaces
$\mathbf{A}^{\mathrm{USC}}$	System matrix with the USC scheme
$\mathbf{M}^{-1}_{\epsilon,\mathrm{local}}$	Inverse local permittivity material matrix
$\mathbf{M}_{\epsilon_0}$	Vacuum permittivity matrix
$\mathbf{M}^{\mathrm{PFC}}_{\epsilon_0}$	Vacuum permittivity material matrix for PFC cells
$\mathbf{M}_{\epsilon^{-1}_{\mathrm{PEC}}}$	Inverse of the permittivity material matrix in the PEC part of Ω
$\mathbf{M}_{\epsilon}$	Permittivity material matrix
$\mathbf{M}^{-1}_{\epsilon}$	Inverse of the permittivity material matrix
$\mathbf{M}^{-1}_{\mu,\mathrm{local}}$	Inverse local permeability material matrix
$\mathbf{M}_{\mu^{-1}}$	Inverse permeability material matrix
$\mathbf{M}_{\mu_0^{-1}}$	Inverse of the vacuum permeability material matrix
$\mathbf{M}_{\mu_0}$	Vacuum permeability material matrix
$\mathbf{M}^{\mathrm{PFC}}_{\mu_0}$	Vacuum permeability material matrix for PFC cells
$\mathbf{M}_{\mu^{-1}_{\mathrm{PEC}}}$	Inverse of the permeability material matrix in the PEC part of Ω
$\mathbf{q}$	Vector of cell charges
$\mathbf{S}$	Source matrix on the primary grid

Mathematics

$\delta(x)$	Delta function
$\delta_{i,j}$	Kronecker Delta
$\frac{\partial}{\partial t}$	Partial derivative with respect to time t
$\frac{\partial^2}{\partial t^2}$	Second partial derivative with respect to time t
i	Imaginary unit
λ	Eigenvalues
∇	Nabla operator
∇^2	Laplace operator
∇^{rot}	Nabla operator in the rotated frame
∂_t	Derivative with respect to time

$\partial_x, \partial_y, \partial_z$	Derivatives with respect to the spatial directions
ϕ	Angle
π	Pi
ψ	Auxiliary scalar field
$\rho\left(\mathbf{A}\right)$	Spectral radius of the matrix $\mathbf{A}$
$\mathbf{R}_{\mathrm{3D}}$	3×3 rotation matrix
$\mathbf{R}_{\mathrm{2D}}$	2×2 rotation matrix
$\vec{d}^{\mathrm{rot}}$	Diagonal of the rotated grid cell
$\vec{e}_r, \vec{e}_\phi, \vec{e}_z$	Base vectors of a cylindrical coordinate system
$\vec{e}_x^{\mathrm{rot}}, \vec{e}_y^{\mathrm{rot}}, \vec{e}_z^{\mathrm{rot}}$	Base vectors in the rotated Cartesian coordinate system
$\vec{r}$	Position vector
$\vec{r}_\perp$	Radius perpendicular to a certain direction
$\vec{v}$	Auxiliary vector field
r_{m}	Radius at the center of a grid cell
$w(z)$	Complex error function of the complex argument z
$\mathbf{R}$	Rotational matrix

Physics

β	Absolute value of the speed relative to the velocity of light $\vec{\beta}$
ΔE_{Q_2}	Energy gain of the witness particle
γ	Lorentz factor
$\lambda\left(r, \phi, z, t\right)$	Line charge distribution
θ	Angle of the collimator tapering
$\vec{\beta}$	Speed relative to the velocity of light
$\vec{E}^{\mathrm{TEM}}$	Electric field of a TEM wave
$\vec{E}_{\mathrm{t}}$	Total electric field
$\vec{e}_x, \vec{e}_y, \vec{e}_z$	Base vectors of a Cartesian coordinate system
$\vec{H}^{\mathrm{TEM}}$	Magnetic field of a TEM wave
$\vec{H}_0$	Exciting magnetic field
$\vec{H}_{\mathrm{s}}$	Scattered magnetic field
$\vec{H}_{\mathrm{t}}$	Total magnetic field
ξ	Phase factor
a	Edge length of the rotated cubic resonator
b	Half of the gap width of a collimator
c_0	Vacuum velocity of light
k_z	Longitudinal component of the wave vector

$m(v)$	Relativistic mass
m_0	Mass at rest
Q	Electric charge
v	Velocity

Bibliography

[1] N. Phinney. ILC Reference Design Report: Accelerator Executive Summary. *ICFA Beam Dynamics Newsletter*, 42:7–29, 2007. 1, 75

[2] T. Weiland. BCI - A Computer Program for Transient Electromagnetic Fields of Bunched Beams in Accelerators. *CERN Report (CERN-ISR)*, CERN-ISR-TH/80-45:1–2, 1980. 3

[3] T. Weiland, R. Wanzenberg. Wakefields and Impedances. pages 140–180,, 1983. 3

[4] Y. H. Chin. User's Guide for ABCI. Version 8.7. *Technical Report*, LBL–35258(CBP Note-069):CERN SL/94–02 (AP), 1994. 3

[5] *CST Particle Studio Users Guide*, CST GmbH, Darmstadt. 3

[6] I. Zagorodnov, T.Weiland. A Conformal Scheme for Wake Field Calculations. In *Proceedings of EPAC 2002, Paris, France*, pages 1682–1684, 2002. 3, 60

[7] E. Gjonaj, X. Dong, R. Hampel, M. Kärkkäinen, T. Lau, W.F.O. Müller, T. Weiland. Large Scale Parallel Wake Field Computations with PBCI. In *Proceedings of the 9th International Computational Accelerator Physics Conference (ICAP 2006), Chamonix, France*, pages 29–34, 2006. 3

[8] E. Gjonaj, T. Lau, S. Schnepp, F. Wolfheimer, T. Weiland. Accurate Modelling of Charged Particle Beams in Linear Accelerators. *New Journal of Physics*, 8:1–21, 2006. 3

[9] T. Weiland. A Discretization Method for the Solution of Maxwell's Equations for Six-Component Fields. *Electronics and Communications (AEÜ)*, 31(3):116–120, 1977. 3

[10] T. Weiland. On the Numerical Solution of Maxwell's Equations and Applications in Accelerator Physics. *Particle Accelerators*, 15:245–292, 1984. 3

[11] M. Faraday. *Experimental Researches in Electricity.* Bernard Quaritch, 15 Piccadilly, London, 1855. 5

[12] A. M. Ampère. *Théorie Mathématique des Phénomènes Électro-Dynamiques.* Libraire Scientifique Albert Blanchard, 1827. 5

[13] J.C. Maxwell. On physical lines of force. *Philosophical Magazine and Journal of Science*, 1861. 5

[14] J.C. Maxwell. *A Treatise on Electricity and Magnetism.* Oxford University Press, 1873. 5

[15] K. Wille. *Physik der Teilchenbeschleuniger und Synchrotronstrahlungsquellen.* Teubner Studienbücher, 1996. 9

[16] J. Rossbach, H. Schmüser. Basic course on accelerator optics. In *Proceedings of CAS 1992, Jyväskylä, Finland*, pages 17–88, 1994. 9

[17] W. K. H. Panofsky, W. A. Wenzel. Some Considerations Concerning the Transverse Deflection of Charged Particles in Radio-Frequency Fields. *Review of Scientific Instruments*, 27:967, 1956. 12

[18] A. W. Chao, M. Tigner. *Handbook of Accelerator Physics and Engineering.* World Scientific, Singapore, 1998. 12

[19] T. Weiland. Comment on Wake Field Calculations in Time-Domain. *Nuclear Instruments and Methods*, 216:255–265, 1983. 13

[20] O. Napoly, Y.H. Chin, B. Zotter. A Generalized Method for Calculating Wake Potentials. *Nuclear Instruments and Methods in Physics Research, Vol A*, 334:31–34, 1993. 13

[21] H. Henke, W. Bruns. Calculation of Wake Potentials in General 3D Structures. In *Proceedings of EPAC 2006, Edinburgh, Scotland*, pages 2170–2172, 2006. 13

[22] I. Zagorodnov. Indirect methods for wake potential integration. *Physical Review Special Topics - Accelerators and Beams*, 9:102002–1 – 102002 – 10, 2006. 13

[23] X. Dong, E. Gjonaj, W.F.O. Müller, T. Weiland. Eigenmode Expansion Method in the Indirect Calculation of Wake Potential in 3D Structures. In *Proceedings of the 9th International Computational Accelerator Physics Conference (ICAP 2006), Chamonix, France*, pages 148–151, 2006. 13, 78

[24] K. S. Yee. Numerical Solution of Initial Boundary Value Problems Involving Maxwell's Equations in Isotropic Media. *IEEE Transactions on Antennas and Propagation*, AP-14:302–307, 1966. 15

[25] F. Edelvik. A General Stability Analysis of FIT/FDTD Applied to Lossy Dielectrics and Lumped Elements. *International Journal of Numerical Modelling*, 17:407–419, 2004. 20

[26] D. Donnelly, E. Rogers. Symplectic integrators: An introduction. *American Journal of Physics*, 73:938–945, 2005. 23

[27] P. Colella, E. G. Puckett. *Modern Numerical Methods for Fluid Flow.* UC Berkley and UC Davis, 1998. 24

[28] J. D. Jackson. *Classical Electrodynamics*. John Wiley & Sons Inc., New Jersey, 1999. 25, 99

[29] K. Bane, T. Weiland. Wake Force Computation in the Time Domain for Long Structures. *Proceedings of the 12th International Conference on High Energy Accelerators, Chicago*, pages 314–316, 1983. 31

[30] R. Hampel, I. Zagorodnov, T. Weiland. New Discretization Scheme for Wake Field Computation in Cylindrically Symmetric Structures. In *Proceedings of EPAC 2004, Luzerne, Switzerland*, pages 2559–2561, 2004. 32

[31] R. Hampel, W.F.O. Müller, T. Weiland. ROCOCO - A Zero Dispersion Algorithm for Calculating Wake Potentials. In *Proceedings of the 9th International Computational Accelerator Physics Conference (ICAP 2006), Chamonix, France*, pages 144–146, 2006. 32

[32] R. Hampel, W.F.O. Müller, T. Weiland. A Dispersionless Algorithm for Calculating Wake Potentials in 3D. In *Proceedings of PAC 2007, Albuquerque, New Mexico, USA*, pages 3268–3270, 2007. 32

[33] M. Dehler. Numerical Wake Calculations using an Equivalence Principle. *Proceedings of the Particle Accelerators Conference*, 49:105–116, 1995. 37

[34] A. Taflove, S. C. Hagness. *Computational Electrodynamics: the finite-difference time-domain method*. Artech House, Boston [u.a.], 2000. 43

[35] S. Dey, R. Mittra. A modified locally-conformal finite-difference time-domain algorithm for modeling three-dimensional perfectly conducting objects. *Microwave and Optical Technology Letters*, 17:349–352, 1998. 43

[36] B. Krietenstein, R. Schuhmann, P. Thoma, T. Weiland. The Perfect Boundary Approximation Technique Facing the Big Challenge of High Precision Field Computation. *Proceedings of the XIX International Linear Accelerator Conference (LINAC 98), Chicago, USA*, pages 860–862, 1998. 43

[37] P. Thoma. *Zur numerischen Lösung der Maxwellschen Gleichungen im Zeitbereich*. PhD thesis, Dissertation D17, Technische Hochschule Darmstadt, Dissertation D17, Technische Hochschule Darmstadt, 1997. 44

[38] S. Dey, R. Mittra. A locally conformal finite-difference time-domain (FDTD) algorithm for modeling three-dimensional perfectly conducting objects. *IEEE Microwave and Guided Wave Letters*, 7(9):273–275, 1997. 44

[39] C. J. Railton, J. B. Schneider. An Analytical and Numerical Analysis of Several Locally-Conformal FDTD Schemes. *IEEE Trans. Microwave Theorz and Techniques*, 47:56–66, 1999. 44

[40] M. B. Timm. *Wake Fields of Short Ultra-Relativistic Electron Bunches*. PhD thesis, Dissertation D17, Technische Hochschule Darmstadt, Dissertation D17, Technische Hochschule Darmstadt, 2000. 48

[41] T. Weiland, B. Zotter. Wake Potentials of a relativistic Current in a Cavity. *Particle Accelerators*, 11:143–151, 1981. 55, 97

[42] S. Ratschow, T. Weiland. Analytical Calculation of the Wake Potential of a Spherical Resonator. *Physical Review Special Topics – Accelerators and Beams*, 5, 2002. 55, 97

[43] S. Molloy, S. Seletskiy, M. Woods, J. D. A. Smith, C. D. Beard, J. L. Fernandez-Hernando, N. Watson, A. Bungau, A. Sopczak. Measurements of the Transverse Wakefields Due to Varying Collimator Characteristics. In *Proceedings of PAC 2007, Albuquerque, New Mexico, USA*, pages 4207–4209, 2007. 76

[44] P. Tenenbaum, K. Bane, L. Eriksson, R.K. Jobe, D. McCormick, C.K. Ng, T.O. Raubenheimer, M.C. Ross, G. Stupakov, D. Walz, D. Onoprienko. Transverse Wakefields from Tapered Collimators: Measurements and Analysis. In *Proceedings of the PAC 2001, Chicago, Illinois, USA*, pages 418–420, 2001. 78

[45] K. L. F. Bane, P. B. Wilson. Bunch Lengthening Due to Potential Well Distortions from Cylindrical Cavities with Beam Ports. *IEEE Transactions on Nuclear Science*, NS-24(3):1485–1486, 1977. 97

[46] P. B. Wilson, K. L. F. Bane. Comparison of Measured and Computed Loss to Parasitic Modes in Cylndrical Cavities with Beam Ports. In *Proceedings of the PAC 1977, Chicago, Illinois, USA*, pages 1496–1498, 1977. 97

[47] N. Marcuvitz. *Waveguide Handbook*. Dover Publications, New York, 1965. 98

[48] M. Abramowitz and I. Stegun. *Handbook of Mathematical Functions*. Dover Publications, New York, 1965. 98

Acknowledgments

Thus ends ...

... this thesis and I want to express my gratitude to the people, who directly or indirectly contributed to its completion.

A great thanks goes to Prof. Dr.-Ing. Thomas Weiland for giving me the opportunity to work in his group, for the fruitful discussions and advice concerning scientific problems.

I thank Prof. Dr.-Ing. Ludger Klinkenbusch for kindly accepting to be my co-referee.

Dr. rer. nat. Erion Gjonaj, Dr.-Ing. Wolfgang Ackermann, and Dr. phil. nat. Wolfgang F. O. Müller deserve my gratitude for their advice on the script for this thesis.

I want to thank Mrs. Dagmar Stenger, Ms. Hava Selmanaj, and Ms. Heike Seiler for their relentless support in all matters of administration and bureaucracy.

Robert Oestreich, Chakrapani Bommaraju, and Stephan Koch discussed various scientific problems with me, for which I am very grateful. Moreover, I want to thank the other colleagues at TEMF.

Very special thanks to Sascha Schnepp for the many fruitful scientific discussions and becoming a good friend of mine.

I thank Holger Fröhlich for his support and the relaxed evenings eating enormously large "Schnitzel".

Thanks to my parents, Helmut and Claudia, and my brother Volker for their support during my scientific career.

And last but not least, I want to thank Mareike Müller for her support and helping me to maintain my balance: Thank you!

Curriculum Vitae

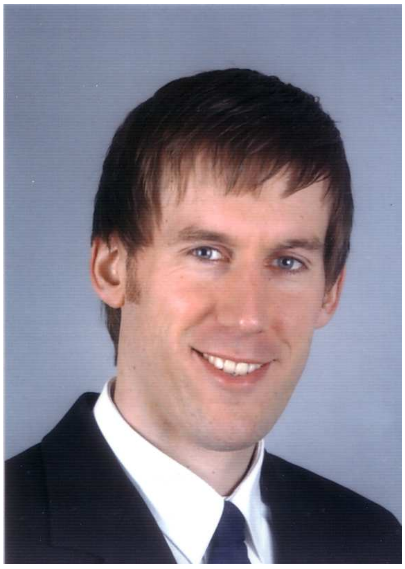

29. Juni 1977	geboren in Frankfurt am Main
1983-1987	Grundschule in Hanau Großauheim
1987-1989	Förderstufe an der Lindenauschule in Hanau Großauheim
1989-1996	Mittel- und Oberstufe an der Hohen Landesschule in Hanau
1996-1997	Grundwehrdienst
1997-2003	Studium der Physik (Diplom) an der Technischen Universität Darmstadt
2002-2003	Diplomarbeit "Mehrkomponentige Vektorsolitonen in photorefraktiven Medien"
seit März 2003	Wissenschaftlicher Mitarbeiter am Institut Theorie Elektromagnetischer Felder des Fachbereichs für Elektrotechnik und Informationstechnik der Technischen Universität Darmstadt